

# Nonlinear Nanoelectromechanical Systems

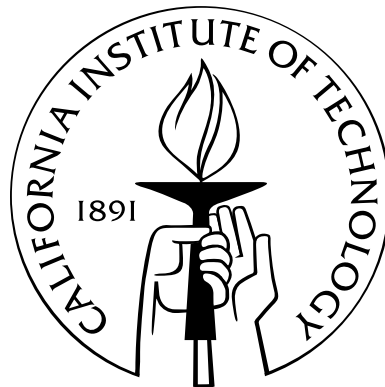
Thesis by

Inna Kozinsky

In Partial Fulfillment of the Requirements

for the Degree of

Doctor of Philosophy



California Institute of Technology

Pasadena, California

2007

(Defended February 8, 2007)

© 2007

Inna Kozinsky

All Rights Reserved

To my parents, Lev and Marina

# Acknowledgements

I would like to thank all the people who have guided and supported me throughout my thesis research. First of all, my advisor Prof. Michael Roukes, for letting me pursue my interest in nonlinear nature of NEMS and for believing in me all these years. I am grateful to my committee members who have made interesting and useful suggestions throughout my graduate life: Prof. Mike Cross, Prof. Ron Lifshitz, Prof. Ali Hajimiri, and Prof. Hideo Mabuchi. I am most thankful to everyone that I had the pleasure of working with closely and learning from, especially Eyal Buks, Henk Postma, Ali Husain, and Oleg Kogan. Without help from and discussions with other Roukes group members, my work would not have followed the same direction and for that I am especially grateful to Philip Feng, Ed Myers, Rassul Karabalin, Sotiris Masmanidis, Sequoyah Aldridge, Matt LaHaye, Ben Gudlewski, Mo Li, Blake Axelrod, Jessica Arlett, James Maloney, Henry Huang, Hong Tang, and Steve Stryker. I had a privilege of interacting and learning from others outside of our group, particularly Prof. Keith Schwab, Prof. Phil Wigen, Prof. Jim Hone, Prof. Kamil Ekinci, Prof. Mark Dykman, Ronen Almog, Nick Melosh, and Florin Grstein. I appreciate that Exie-Marie Leagons and Loly Ekmekjian made everything run smoothly and were always there for us.

Many, many thanks go to my family for their constant love and support. And to my Caltech and Harvard friends for the warmth of their friendship and many scientific and philosophical discussions. And above all to Igor Bargatin, my wonderful partner in crime at home and in the lab, for his love and encouragement and for all the shared adventures.

# Abstract

Nano-electro-mechanical systems (NEMS), used as sensors for small masses and forces, have traditionally been operated in the linear regime. While convenient for engineering applications, the linear regime is getting harder to maintain as the devices grow smaller. The first part of this thesis develops a theoretical framework for analysis of nonlinear nanomechanical devices and establishes that nonlinear effects become more significant in smaller resonators. As a result, nonlinear nanomechanical resonators offer a convenient playground for studies of nonlinear dynamics as well as open up new possibilities for enhancing performance of NEMS devices. To illustrate both of these trends, the thesis presents experimental investigations of nonlinear dynamics using nanoresonators and demonstrates several effects in nonlinear NEMS in an effort to build the foundation necessary for engineering highly sensitive, versatile, and controllable NEMS devices.

As an example of exploring nonlinear dynamics with NEMS, we present the experimental mapping of basins of attraction of a nonlinear platinum nanowire resonator. We also measure the rate of the observed noise-induced transitions between two stable states in the nonlinear regime as the artificial noise is added to the system. An additional set of experiments demonstrates increased versatility of NEMS devices made possible by their intrinsic nonlinearity. Devices with tunable frequency, nonlinearity, and dynamic range are explored experimentally and theoretically. We show how to induce the coupling of orthogonal modes in nanomechanical resonators. We also detect multiple higher-order modes in doubly-clamped beams and observe increased dynamic range of operation in these modes. Several ideas for further experiments with nonlinear nanomechanical resonators are proposed.

# Contents

<b>Acknowledgements</b>	<b>iv</b>
<b>Abstract</b>	<b>v</b>
<b>1 Introduction</b>	<b>1</b>
1.1 Motivation . . . . .	1
1.2 Overview . . . . .	2
<b>2 Theoretical Foundation</b>	<b>4</b>
2.1 Elastic beam theory . . . . .	4
2.2 Nonlinear dynamics . . . . .	8
2.2.1 Method of multiple scales . . . . .	8
2.2.2 Duffing equation analysis using the method of multiple scales . . . . .	10
2.2.2.1 Amplitude analysis . . . . .	14
2.2.2.2 Phase analysis . . . . .	17
2.2.2.3 Stability of steady-state motion . . . . .	20
2.3 Nonlinear NEMS . . . . .	22
2.3.1 Sources of nonlinearity . . . . .	22
2.3.2 Dynamic range of beams . . . . .	24
<b>3 Experimental Techniques</b>	<b>32</b>
3.1 Devices . . . . .	32
3.1.1 Gold beams on silicon nitride membranes . . . . .	32

3.1.2	Silicon carbide beams and cantilevers	34
3.1.3	Metal nanowires	35
3.2	Transduction schemes	37
3.2.1	Electron beam detection	37
3.2.1.1	SEM Detector system	38
3.2.1.2	Experimental setup	39
3.2.1.3	Nonlinearity of the detector response	41
3.2.1.4	Detector bandwidth	44
3.2.2	Magnetomotive drive and detection	45
3.2.3	Magnetomotive drive and piezoresistive detection	47
3.2.4	Thermoelastic drive and piezoresistive detection	48
3.3	Resonant response analysis	50
<b>4</b>	<b>Exploring Nonlinear Dynamics with NEMS</b>	<b>55</b>
4.1	Basins of attraction	55
4.1.1	Theoretical analysis	59
4.1.2	Experimental technique and results	60
4.2	Noise-induced transitions	63
4.2.1	Theoretical results	64
4.2.2	Waiting time measurements	64
4.2.3	Sweep measurements	69
4.2.4	Noise analysis	72
4.3	Ideas for future experiments	74
4.3.1	Bifurcation amplifier	74
4.3.2	Basins of attraction of coupled resonators	75
4.3.3	Noise-induced transitions in a quantum nonlinear resonator	76

<b>5 Making Versatile Devices using Nonlinear NEMS</b>	<b>77</b>
5.1 Tuning frequency, nonlinearity, and dynamic range . . . . .	78
5.2 Interaction of orthogonal modes . . . . .	85
5.3 Higher flexural modes of beams . . . . .	90
5.4 Ideas for future experiments . . . . .	95
5.4.1 Self-tuning resonators . . . . .	95
5.4.2 Cooling of a resonator mode by interaction with another mode . . . . .	96
5.4.3 Synchronization of coupled oscillators . . . . .	97
<b>6 Concluding Remarks</b>	<b>98</b>
<b>Bibliography</b>	<b>100</b>
<b>A Duffing equation analysis using Landau and Lifshitz method</b>	<b>113</b>
<b>B Mathematica script for solving the nonlinear equation with electrostatics</b>	<b>118</b>
<b>C Matlab routine for fitting resonance with a background</b>	<b>129</b>

# List of Figures

2.1	Theoretical amplitude of the response of a Duffing resonator as a function of swept driving frequency (a) and swept driving amplitude (b) . . . . .	15
2.2	Theoretical phase of the response of a Duffing resonator as a function of swept driving frequency (a) and swept driving amplitude (b) . . . . .	18
2.3	Schematic representation of a doubly-clamped nanomechanical resonator of length $L$ and diameter $d$ . . . . .	25
2.4	Schematic representation of dynamic range as a distance between the noise floor and the onset of nonlinearity . . . . .	28
2.5	Calculated dynamic ranges of several doubly-clamped nanomechanical resonators as a function of their length . . . . .	30
3.1	Fabrication process for gold beams on top of a silicon nitride membrane . . . . .	33
3.2	Examples of gold NEMS devices fabricated on silicon nitride membranes . . . . .	34
3.3	Examples of silicon carbide NEMS devices . . . . .	35
3.4	Electron beam detection setup . . . . .	38
3.5	Signal measured using electron beam detection technique . . . . .	40
3.6	Estimation of nonlinearity in detector response in the scanning electron microscope measurement scheme . . . . .	42
3.7	Schematic of magnetomotive drive and detection technique . . . . .	46
3.8	Room-temperature magnetomotive excitation setup photograph and measured response	47
3.9	Thermoelastic drive and piezoresistive detection setup . . . . .	49

3.10	Steps in the procedure for fitting experimental resonance data to a Lorentzian with a background . . . . .	52
3.11	Example of the fits obtained with the Lorentzian fitting procedure . . . . .	54
4.1	Setup of the experiment to map out the basins of attraction in the nanowire resonator	57
4.2	Experimentally measured basins of attraction . . . . .	61
4.3	Noise-induced transition waiting time histogram with no added noise . . . . .	65
4.4	Experimental setup to measure the effect of added noise on the transition rate between two stable states of the nanowire resonator . . . . .	66
4.5	Analysis of noise-induced transition data and extraction of the critical exponent . . . .	67
4.6	Experimental setup to collect the statistics of noise-induced transitions by using amplitude-modulated signal to sweep through both bifurcation points and detecting the response with an oscilloscope . . . . .	69
4.7	Experimental setup to collect the statistics of noise-induced transitions by using amplitude-modulated signal to sweep through both bifurcation points and detecting the response with a data acquisition system . . . . .	71
5.1	Resonant response of the suspended SiC doubly-clamped beam to a progressively increased drive . . . . .	78
5.2	Tuning of dynamic range, critical amplitude, and effective nonlinearity with the gate voltage . . . . .	79
5.3	Tuning of resonant frequency with the gate voltage . . . . .	81
5.4	Interaction of orthogonal modes in silicon carbide beams observed magnetotomively . .	85
5.5	Interaction of orthogonal modes in gold beams observed with the SEM . . . . .	86
5.6	An example frequency-response curve of a two-degree-of-freedom Duffing system with internal resonance . . . . .	87
5.7	Simulated coupled orthogonal mode shapes . . . . .	88

5.8	Raw signal from a thermoelastically actuated and piezoresistively detected $16\mu\text{m}$ -long beam, showing the first eight modes . . . . .	91
5.9	Critical strain dependence on mode number . . . . .	93
A.1	Theoretical amplitude of the response of a Duffing resonator as a function of swept driving frequency for increasing drive amplitude calculated using the Landau and Lifshitz method . . . . .	117

# List of Tables

2.1	Properties of a silicon carbide resonator, platinum nanowire, multi- and single-walled nanotube used as input parameters for calculation of dynamic range in Figure 2.5 . . .	29
5.1	Predicted and experimental frequencies and quality factors for the lowest 17 flexural modes of SiC beams . . . . .	92

# Chapter 1

## Introduction

If you hit a tuning fork twice as hard it will ring twice as loud but still at the same frequency. That's a linear response. If you hit a person twice as hard they're unlikely just to shout twice as loud. That property lets you learn more about the person than the tuning fork.

---

*When Things Start to Think*  
NEIL GERSHENFELD

### 1.1 Motivation

Why do we care about shrinking down resonating mechanical systems so that they reach nanoscale dimensions and have to be fabricated painstakingly in a cleanroom over weeks or perhaps months? One reason is the ability to detect very small physical quantities. A recent breakthrough in mass sensing is a device with a mass resolution of 7 zeptograms ( $7 \times 10^{-21}$ ), equivalent to  $\sim 30$  xenon atoms [116]. Unprecedented force sensitivity was demonstrated by single electron spin detection [95]. In the past few years, even more sensing, imaging, and processing applications emerged, including magnetic resonance force microscopy [103] and improvements in RF communications [88]. Another reason is an irresistible temptation to see quantum mechanics of mechanical devices. By decreasing the size of mechanical devices, increasing their resonant frequency, and cooling them down to mK temperatures, we expect the mechanical motion of nanoscale resonators to approach the quantum regime [4, 63, 72, 23]. All of these applications require both high responsivity and ultra-high-frequency operation [55]. Engineering considerations also call for a large dynamic range, over

which the device responds linearly to the stimulus, as well as operation at desired and, preferably, adjustable frequencies.

Unfortunately, the real world with its inconvenient nonlinearities does not cooperate very well with our designs. It turns out that the onset of nonlinear regime for operation of nanomechanical resonators decreases with decreasing diameter, so that the useful linear dynamic range of the smallest NEMS devices is severely limited. In fact, many applications we are hoping for in the near future will involve operation in the nonlinear regime, where the response to the stimulus is suppressed and frequency is pulled away from the original resonant frequency. This thesis is about embracing this idiosyncrasy of nature and exploring ways in which intrinsic nonlinearity in NEMS devices can be made to work for us to improve our devices and to further our knowledge of physics.

The easily reachable nonlinear regime in nanomechanical resonators is a great tool for fundamental studies of nonlinear dynamics. Nonlinear systems usually require thousands of cycles to study. A lot of experiments aimed at exploring nonlinear dynamics in low-frequency macroscopic systems turn out to be prohibitively long. However, in high-frequency nanoscale resonators, the steady state is achieved in a fraction of a second and we are able to perform multiple measurements of the system in a relatively short time and before the experimental parameters start to drift. Besides, the state of art in nanofabrication allows us to design devices required for such studies in a relatively short period of time compared with building of nonlinear macroscopic systems.

Nonlinearity introduces a number of new effects in NEMS devices. Ability to control them at will is as important for applications as finding ways to use them to enhance the performance of nanomechanical devices for precision measurement applications. I will present the studies of several effects in nonlinear NEMS, but these are just the first steps in building the foundation necessary for engineering highly sensitive, versatile, and controllable NEMS devices.

## 1.2 Overview

Chapter 2 presents the theoretical foundation for the analysis of nonlinear NEMS devices. It summarizes the elastic beam theory and nonlinear dynamics theory necessary for the analysis of NEMS

beams and cantilevers. We use the Galerkin discretization procedure to obtain simple analytical expressions for frequency and nonlinear coefficients. Finally, the elastic beam and nonlinear dynamics formalisms are applied to the analysis of NEMS beams. Sources of nonlinearity in beams and cantilevers as well as dynamic range of NEMS beams are discussed.

Chapter 3 describes fabrication and characteristics of various devices that I have used in nonlinear NEMS experiments and includes gold beams fabricated on silicon nitride, silicon carbide beams, and metal nanowires. This chapter also outlines the transduction schemes that have been used with these devices. These include electron beam detection inside the SEM, magnetomotive transduction, and magnetomotive drive and thermoelastic drive coupled with piezoresistive detection. At the end I discuss a fitting procedure for resonance signals on top of a background that allows us to extract accurate resonant frequency and quality factor.

Chapter 4 describes the experimental studies of nonlinear dynamics performed with nonlinear NEMS resonators. It presents the mapping of the basins of attraction of a nonlinear platinum nanowire resonator in its bistable state. I also discuss our studies of the observed transitions between the two stable states of the resonator induced by the environmental and artificially added noise. Since nonlinear regime is readily accessible in nanoscale devices, the details of their dynamical behavior are not only easy and exciting to study, but their understanding is important for proper engineering and analysis of nanoscale systems. Ideas for potential applications of resonators operating in nonlinear regime for enhancing the sensitivity of experimental measurements are presented at the end of the chapter.

The understanding of dynamics of NEMS resonators opens up possibilities for better devices for sensor applications. Chapter 5 describes various effects in NEMS that promise to enhance versatility, performance, and sensitivity of NEMS sensors. They include resonant frequency tuning, dynamic range enhancement, orthogonal mode coupling, and operation of NEMS in higher vibrational modes. I present both experimental and theoretical investigations of these effects. Ideas for future experiments based on the completed work conclude the chapter.

## Chapter 2

# Theoretical Foundation

... theories don't prove nothing, they only give you a place to rest on, a spell, when you are tuckered out butting around and around and trying to find out something there ain't no way to find out... There's another trouble about theories: there's always a hole in them somewheres, sure, if you look close enough.

---

*Tom Sawyer Abroad*  
MARK TWAIN

This chapter presents the theoretical foundation for the analysis of nonlinear NEMS devices. It summarizes the elastic beam theory and nonlinear dynamics theory necessary for the analysis of NEMS beams and cantilevers. An original contribution in this chapter is the use of the Galerkin discretization procedure to obtain simple analytical expressions for frequency and nonlinear coefficients. Finally, the elastic beam and nonlinear dynamics formalisms are applied to the analysis of NEMS beams. The dynamic range of NEMS beams and cantilevers is discussed.

### 2.1 Elastic beam theory

This section develops the elastic beam theory using the Galerkin discretization procedure. Analytical formulas for resonant frequencies of beams under both stress and tension and a profile of an electrostatically-driven beam are derived. The dynamics of an elastic beam driven by some force per unit length  $f(x, t)$ , where  $x$  is along the axis of the beam and  $z$  is the direction of its displacement,

is described by the equation of motion,

$$EIz_{xxxx} - Tz_{xx} + \rho S z_{tt} - f(x, t) = 0. \quad (2.1.1)$$

Here,  $E$  is the Young's modulus,  $I$  is the moment of inertia,  $S$  is the beam's cross-sectional area, and  $T$  is the total tension present in the beam. The two clamped ends impose the boundary conditions,  $z(0, t) = z(L, t) = z_x(0, t) = z_x(L, t) = 0$ .

The steady-state solution to this equation, when  $z_t = 0$ , gives a static displacement profile of a doubly-clamped beam deflected by a displacement-independent force per unit length,  $f$ :

$$z(x) = \frac{f}{2T} \left[ (L-x)x + L\sqrt{EI/T} \left( -\coth\left(\frac{L}{2\sqrt{EI/T}}\right) + \cosh\left(\frac{L-2x}{2\sqrt{EI/T}}\right) \operatorname{csch}\left(\frac{L}{2\sqrt{EI/T}}\right) \right) \right] \quad (2.1.2)$$

The exact analytical solutions of the full equation (2.1.1) exist and are well-known for two limiting cases: beams under negligible tension and dominated by stress, or bending rigidity; and beams dominated by tension, sometimes referred to as strings.

In the string limit, when tension dominates over stress,  $EI/T \ll 1$  and no drive is applied to the system, the displacement profile is simply

$$z(x) = A \sin\left(\sqrt{\frac{\rho S}{T}} \omega_n x\right), \quad \text{with } \omega_n = \frac{n\pi}{L} \sqrt{\frac{T}{\rho S}}. \quad (2.1.3)$$

In the stress limit, where tension is negligible compared to bending rigidity,  $T/EI \ll 1$  and no drive is applied to the system, a general doubly-clamped beam profile is

$$z(x) = A \left[ \cos(\kappa x) - \cosh(\kappa x) - \frac{\cos(\kappa L) - \cosh(\kappa L)}{\sin(\kappa L) - \sinh(\kappa L)} (\sin(\kappa x) - \sinh(\kappa x)) \right], \quad (2.1.4)$$

where  $\kappa^2 = \sqrt{\frac{\rho S}{EI}} \omega$ . The boundary conditions for a doubly-clamped beam impose the condition on  $\kappa$ ,  $\cos(\kappa L) \cosh \kappa L = 1$ . The roots of this equation, which can be found numerically or graphically,

allow us to express  $\omega_n$  in terms of  $\kappa_n$ :

$$\omega_n = \kappa_n^2 \sqrt{\frac{EI}{\rho S}}, \quad \text{where } \kappa_n L = 4.73, 7.8532, 10.9956, \dots \quad (2.1.5)$$

and  $\kappa_n L$  tends to  $(n + 1/2)\pi$  for large  $n$  [81].

When both bending rigidity and tension in the beam have comparable effects on its dynamics, the equation of motion (2.1.1) cannot be solved analytically because  $\kappa L$  becomes dependent on tension. Using separation of variables,  $z(x, t) = X(x)\Theta(t)$ , and letting  $\Theta(t) = e^{i\omega t}$  and  $X(x) = e^{\kappa x}$ , we can express  $\kappa$  in terms of frequency,  $\omega$  for the unforced case:

$$EI\kappa^4 - T\kappa^2 - \omega^2\rho S = 0 \quad \implies \kappa_{1,2}^2 = \frac{T \pm \sqrt{T^2 + 4EI\rho S\omega^2}}{2EI}. \quad (2.1.6)$$

There are two real and two imaginary roots  $\kappa$ . Therefore, the beam profile has the shape

$$X(x) = A \cos(\kappa_2 x) + B \sin(\kappa_2 x) + C \cosh(\kappa_1 x) + D \sinh(\kappa_1 x). \quad (2.1.7)$$

The boundary conditions for a doubly-clamped beam result in the following characteristic equation:

$$2 - 2 \cos(\kappa_2 L) \cosh(\kappa_1 L) + \left( \frac{\kappa_1}{\kappa_2} - \frac{\kappa_2}{\kappa_1} \right) \sin(\kappa_2 L) \sinh(\kappa_1 L) = 0. \quad (2.1.8)$$

Here,  $\kappa_1$  and  $\kappa_2$  are different and tension-dependent. In the case of  $T = 0$ ,  $\kappa_1 = \kappa_2$  (see equation (2.1.6)) and the characteristic equation (2.1.8) reduces to  $\cos(\kappa L) \cosh \kappa L = 1$ , which is the previously-discussed characteristic equation for the beam with no tension, whose roots  $\kappa L$  are numbers. However, when  $\kappa_1$  and  $\kappa_2$  are not the same, the roots of the equation (2.1.8) are tension-dependent and can only be found analytically for a given tension. Since we are interested in mode shapes and frequencies as a function of tension,  $T$ , this approach is inconvenient. Instead, I will show next how we can find an approximate solution to the equation of motion (2.1.1), which allows us to capture analytical dependencies on all of the device parameters.

We will write down the full equation of motion for the system,

$$\mathcal{L}[z(x, t)] = EI z_{xxxx} - T z_{xx} + \rho S z_{tt} - f(x, t) = 0, \quad (2.1.9)$$

and assume that the full solution can be expressed in terms of a linearly independent set of basis functions  $\phi_k(x)$ ,

$$z(x, t) = \sum_{k=1}^N z_k(t) \phi_k(x), \quad (2.1.10)$$

where  $z_k(t)$  is the time-dependent part of the response. This is known as the Galerkin discretization procedure [85]. Each basis function is chosen so that it satisfies the boundary conditions, so that exact mode shapes could be one such basis. The error associated with this approximation technique is

$$e(x, t) = \mathcal{L} \left[ \sum_{k=1}^N z_k(t) \phi_k(x) \right] - \mathcal{L}[z(x, t)] \quad . \quad (2.1.11)$$

The Galerkin procedure requires this error to be orthogonal to each basis function, or in other words, the error is a residual that cannot be expressed in terms of the given finite set of basis functions:

$$\int_0^L e(x, t) \phi_n(x) dx = 0 \quad (2.1.12)$$

Multiplying the expanded error equation (2.1.11) by a mode  $\phi_n(x)$  and integrating from 0 to  $L$  leaves only the  $z_n$  and  $\phi_n$  terms because  $\int_0^L \phi_k(x) \phi_n(x) dx = 0$  if  $k \neq n$ . Also using the fact that  $\mathcal{L}[z(x, t)] = 0$  as given in the equation (2.1.9), we get

$$\begin{aligned} \left( \int_0^L \phi_n^2(x) dx \right) \ddot{z}_n(t) + \left( \frac{EI}{\rho S} \int_0^L \phi_n''''(x) \phi_n(x) dx - \frac{T}{\rho S} \int_0^L \phi_n''(x) \phi_n(x) dx \right) z_n(t) = \\ = \frac{1}{\rho S} \int_0^L f(x, t) \phi_n(x) dx. \end{aligned} \quad (2.1.13)$$

From here, we can write down an analytical formula for the mode frequencies,

$$\omega_n^2 = \frac{\frac{EI}{\rho S} \int_0^L \phi_n''''(x) \phi_n(x) dx - \frac{T}{\rho S} \int_0^L \phi_n''(x) \phi_n(x) dx}{\int_0^L \phi_n(x)^2 dx}. \quad (2.1.14)$$

Integrating by parts and using the boundary conditions, the expression for mode frequencies simplifies to

$$\omega_n^2 = \frac{\frac{EI}{\rho S} \int_0^L \phi_n''(x)^2 dx + \frac{T}{\rho S} \int_0^L \phi_n'(x)^2 dx}{\int_0^L \phi_n(x)^2 dx}. \quad (2.1.15)$$

From this expression, we can clearly see that the presence of any tension,  $T$ , in the beam increases the resonant frequency.

The question of calculating the frequency of a desired mode now boils down to picking the appropriate basis to use in this equation.

## 2.2 Nonlinear dynamics

This section presents a theoretical framework for the analysis of nonlinear behavior. For simplicity, this section will address directly driven systems and include only cubic nonlinearity in the equation of motion. This is done under the assumption that the nonlinearity is small so that the higher order nonlinearities in displacement (fifth, seventh order, and so on) are not significant, and that the system is more or less symmetric.<sup>1</sup> The framework and methods presented in this section are general and can be applied to systems with higher order nonlinear terms and other driving types [85, 80].

### 2.2.1 Method of multiple scales

A general way to approach the analysis of a dynamical system is to look for a time-dependent function (a solution of a differential equation of motion) that describes the response of the system to an initial disturbance. One obtains the response of a nonlinear system by perturbing the response of

---

<sup>1</sup>The deviations from symmetry will be reflected in the appearance of quadratic and other even-power terms. Nonlinearities can also modify the damping forces in the system (i.e. velocity rather than displacement). For the following calculations, we ignore these nonlinearities altogether, but they can be present in the system independently and have to be included in the full calculation if they are on the order of displacement nonlinearities.

the corresponding linear system (which is obtained by simply deleting all the nonlinear terms from the equation). There are many ways that this perturbation can be modeled and calculated [85].

A naive approach is a straightforward expansion. We introduce a small, dimensionless parameter,  $\varepsilon$ , which is the order of the amplitude of the motion and expand the solution as

$$u(t; \varepsilon) = \varepsilon x_1(t) + \varepsilon^2 x_2(t) + \varepsilon^3 x_3(t) + \dots \quad (2.2.1)$$

This form of the solution can be substituted into the nonlinear equation and, after a lot of algebra which will be omitted here, one will find that  $x_1(t)$  is periodic. However, starting with  $x_3(t)$ , the corrections to the linear behavior will contain factors  $t^m \cos(\omega_0 t + \beta)$  and  $t^m \sin(\omega_0 t + \beta)$ . Such terms are called "secular terms".<sup>2</sup>

Because of secular terms, the entire expansion (2.2.1) is not periodic and, moreover,  $x_3/x_1$ ,  $x_3/x_2$ , and so on grow without bound as  $t$  increases. The underlying reason for such a nonsensical solution is that one of the differences between a linear and a nonlinear system is the interconnection between frequency and amplitude of the system, and there was no provision for this interaction in the straightforward expansion (2.2.1).

The method of multiple scales offers an alternative way of applying a nonlinear perturbation that takes the possible interaction between terms into account. The idea is to consider the expansion that represents the response as a function of multiple independent variables, or scales, instead of a single variable. The multiple time scales are defined as

$$T_n = \varepsilon^n t \text{ for } n = 0, 1, 2, \dots \quad (2.2.2)$$

The time scale  $T_1$  is slower than  $T_0$ ;  $T_2$  is slower than  $T_1$ . In general,  $T_n$  is slower than  $T_{n-1}$ . "Slow" means over a time scale much longer than the natural period of the system. The time scale are assumed to be disparate enough so that the time scales,  $T_i$ , are treated as independent variables.

---

<sup>2</sup>The term *secular* is derived from the Latin *saeculum*, meaning *century*, and was first used in astronomical applications, where  $\varepsilon$  is quite small and  $\varepsilon t$  becomes significant only if  $t$  is on order of a century.

The derivatives with respect to  $t$  can be expressed in terms of partial derivatives with respect to  $T_n$ :

$$\frac{d}{dt} = \frac{dT_0}{dt} \frac{\partial}{\partial T_0} + \frac{dT_1}{dt} \frac{\partial}{\partial T_1} + \dots = D_0 + \varepsilon D_1 + \dots \quad (2.2.3)$$

$$\frac{d^2}{dt^2} = D_0^2 + 2\varepsilon D_0 D_1 + \varepsilon^2 (D_1^2 + 2D_0 D_2) + \dots \quad (2.2.4)$$

We can then express the solution in terms of different time scales:

$$u(t; \varepsilon) = u_0(T_0, T_1, T_2, \dots) + \varepsilon u_1(T_0, T_1, T_2, \dots) + \varepsilon^2 u_2(T_0, T_1, T_2, \dots) + \dots \quad (2.2.5)$$

### 2.2.2 Duffing equation analysis using the method of multiple scales

A directly driven system with a cubic nonlinearity is described by a Duffing equation:

$$\ddot{u} + \omega_0^2 u + 2\varepsilon \mu \dot{u} + \varepsilon \alpha u^3 = E(t), \quad (2.2.6)$$

where the damping coefficient  $\mu > 0$  and nonlinear coefficient is either  $\alpha > 0$  (hard spring) or  $\alpha < 0$  (soft spring). We will consider an ideal source that is not affected by the excited system:  $E(t) = K \cos \Omega t$ . For driving forces that are not too strong, we will take  $K = \varepsilon k$ . The most important response is at the primary resonance of the system,  $\Omega \approx \omega_0$ . Let

$$\Omega = \omega_0 + \varepsilon \sigma, \quad (2.2.7)$$

where  $\sigma$  is a frequency detuning parameter.

Using the method of multiple scales, we expand the solution in terms of two different time scales  $T_0$  and  $T_1$ :

$$u(t; \varepsilon) = u_0(T_0, T_1) + \varepsilon u_1(T_0, T_1) + \dots, \quad (2.2.8)$$

where the multiple time scales are defined as  $T_n = \varepsilon^n t$ . Here,  $T_0 = t$  gives the natural period of oscillations of the undamped harmonic version of the system.  $T_1 = \varepsilon t$  is a slower time scale on which

damping and nonlinearity affect the system. The excitation can be similarly re-written as

$$E(t) = \varepsilon k \cos(\omega_0 T_0 + \sigma T_1). \quad (2.2.9)$$

The derivatives of  $u(t; \varepsilon)$  are

$$\begin{aligned} \dot{u} &= D_0 u_0 + \varepsilon D_1 u_0 + \varepsilon D_0 u_1 + \mathcal{O}(\varepsilon^2) \\ \ddot{u} &= D_0^2 u_0 + 2\varepsilon D_1 D_0 u_0 + \varepsilon D_0^2 u_1 + \mathcal{O}(\varepsilon^2), \end{aligned}$$

where  $D_0 = \partial/\partial T_0$  and  $D_1 = \partial/\partial T_1$ . When we substitute those into the equation of motion, we get

$$D_0^2 u_0 + 2\varepsilon D_1 D_0 u_0 + \varepsilon D_0^2 u_1 + \omega_0^2 u_0 + \varepsilon \omega_0^2 u_1 + 2\varepsilon \mu D_0 u_0 + \varepsilon \alpha (u_0^3 + 3\varepsilon u_0 u_1 + \mathcal{O}(\varepsilon^2)) = \varepsilon k \cos(\omega_0 T_0 + \sigma T_1). \quad (2.2.10)$$

Collecting powers of  $\varepsilon$ , we get partial differential equations:

$$D_0^2 u_0 + \omega_0^2 u_0 = 0 \text{ for } \varepsilon^0 \quad (2.2.11)$$

$$D_0^2 u_1 + \omega_0^2 u_1 = -2D_0 D_1 u_0 - 2\mu D_0 u_0 - \alpha u_0^3 + k \cos(\omega_0 T_0 + \sigma T_1) \text{ for } \varepsilon^1. \quad (2.2.12)$$

The solution to the  $\varepsilon^0$  equation has the form

$$u_0 = A(T_1) e^{i\omega_0 T_0} + \bar{A}(T_1) e^{-i\omega_0 T_0}. \quad (2.2.13)$$

Let's substitute this expression for  $u_0$  into the  $\varepsilon^1$  equation. We will need

$$\begin{aligned} D_0 u_0 &= i\omega_0 A(T_1) e^{i\omega_0 T_0} - i\omega_0 \bar{A}(T_1) e^{-i\omega_0 T_0} \\ D_1 D_0 u_0 &= i\omega_0 D_1 A(T_1) e^{i\omega_0 T_0} - i\omega_0 D_1 \bar{A}(T_1) e^{-i\omega_0 T_0} \\ u_0^3 &= A(T_1)^3 e^{3i\omega_0 T_0} + \bar{A}(T_1)^3 e^{-3i\omega_0 T_0} + 3\bar{A}(T_1) A(T_1)^2 e^{i\omega_0 T_0} + \\ &+ 3\bar{A}(T_1)^2 A(T_1) e^{-i\omega_0 T_0} \end{aligned}$$

$$\text{Note also: } \cos(x) = \frac{1}{2}(e^{ix} + e^{-ix}).$$

The actual substitution gives

$$\begin{aligned} D_0^2 u_1 + \omega_0^2 u_1 &= -[2i\omega_0(D_1 A(T_1) + \mu A(T_1)) + 3\alpha A(T_1)^2 \bar{A}(T_1)] e^{i\omega_0 T_0} + \\ &+ [2i\omega_0(D_1 \bar{A}(T_1) + \mu \bar{A}(T_1)) - 3\alpha \bar{A}(T_1)^2 A(T_1)] e^{-i\omega_0 T_0} - \\ &- \alpha A(T_1)^3 e^{3i\omega_0 T_0} - \alpha \bar{A}(T_1)^3 e^{-3i\omega_0 T_0} + \frac{1}{2} k [e^{i(\omega_0 T_0 + \sigma T_1)} + e^{-i(\omega_0 T_0 + \sigma T_1)}]. \end{aligned} \quad (2.2.14)$$

The terms proportional to  $e^{\pm i\omega_0 T_0}$  on the right side of the above equation for  $u_1$  (called "secular" terms) behave like a force that drives a harmonic oscillator characterized by left side of the equation on resonance. But we would like  $u_0$  to include all the resonance terms, so that the other contributions to the resonance in the full solution  $u$  are small. This means that in equations for  $u_1, u_2, \dots$  we want to eliminate all secular terms. They are eliminated if we choose  $A(T_1)$  to be a solution of

$$2i\omega_0(D_1 A(T_1) + \mu A(T_1)) + 3\alpha A(T_1)^2 \bar{A}(T_1) - \frac{1}{2} k e^{i\sigma T_1} = 0. \quad (2.2.15)$$

To solve this equation, let's express the solution in the form  $A(T_1) = \frac{1}{2} a(T_1) e^{i\beta(T_1)}$ , where  $a(T_1)$  and  $\beta(T_1)$  are real (and, therefore,  $D_1 A(T_1) = \frac{1}{2} D_1 a(T_1) e^{i\beta(T_1)} + \frac{i}{2} a(T_1) D_1 \beta(T_1) e^{i\beta(T_1)}$ ). For convenience, we make the dependence of  $a$  and  $\beta$  on  $T_1$  implicit in all further calculations. Substituting

this into the above equation gives

$$\begin{aligned}
2i\omega_0 \left[ \frac{1}{2}(D_1 a(T_1) + ia(T_1)D_1 \beta(T_1))e^{i\beta} + \frac{1}{2}\mu a e^{i\beta} \right] + 3\alpha \frac{1}{4} a^2 e^{2i\beta} \frac{1}{2} a' e^{-i\beta} - \frac{1}{2} k e^{i\sigma T_1} = 0 &\implies \\
e^{i\beta} \left( iD_1 a \omega_0 - aD_1 \beta \omega_0 + i\omega_0 \mu a + \frac{3}{8} \alpha a^3 \right) = \frac{1}{2} k e^{i\sigma T_1} &\implies \\
\left( \frac{3}{8} \alpha a^3 - aD_1 \beta \omega_0 \right) + i(\omega_0 \mu a + D_1 a \omega_0) = \frac{k}{2} (\cos(\sigma T_1 - \beta) + i \sin(\sigma T_1 - \beta)). &
\end{aligned} \tag{2.2.16}$$

Collecting the real and imaginary parts separately, we can get two equations:

$$\text{Real: } aD_1 \beta = \frac{3\alpha}{8\omega_0} a^3 - \frac{k}{2\omega_0} \cos(\sigma T_1 - \beta) \tag{2.2.17}$$

$$\text{Imag: } D_1 a = -\mu a + \frac{k}{2\omega_0} \sin(\sigma T_1 - \beta). \tag{2.2.18}$$

Re-writing our solution for  $u_0$ ,

$$u_0 = A(T_1)e^{i\omega_0 T_0} + \bar{A}(T_1)e^{-i\omega_0 T_0} = \frac{1}{2} a e^{i(\beta + \omega_0 T_0)} + \frac{1}{2} a e^{-i(\beta + \omega_0 T_0)} = a \cos(\omega_0 T_0 + \beta) = a \cos(\omega_0 t + \beta). \tag{2.2.19}$$

For convenience, let  $\gamma = \sigma T_1 - \beta$ . Then the first-order response can be re-written as

$$u_0 = a \cos(\omega_0 t + \beta) = a \cos(\omega_0 t + \varepsilon \sigma t - \gamma) = a \cos(\Omega t - \gamma), \tag{2.2.20}$$

where  $\Omega$  is the frequency of the drive and, in the beginning of the principal resonance discussion, we have taken  $\Omega = \omega_0 + \varepsilon \sigma$ . It means that, in general, the phase of the response is shifted from that of the excitation by  $-\gamma$ .

The equations for variation in phase and amplitude of the response are

$$D_1 a = -\mu a + \frac{k}{2\omega_0} \sin \gamma \tag{2.2.21}$$

$$aD_1 \gamma = a\sigma - \frac{3\alpha}{8\omega_0} a^3 + \frac{k}{2\omega_0} \cos \gamma \tag{2.2.22}$$

For steady state motion, there is no change in amplitude, phase or frequency,  $D_1 a = D_1 \gamma = 0$ , which means that the equations above reduce to

$$\mu a = \frac{k}{2\omega_0} \sin \gamma \quad (2.2.23)$$

$$a\sigma - \frac{3\alpha}{8\omega_0} a^3 = -\frac{k}{2\omega_0} \cos \gamma \quad (2.2.24)$$

### 2.2.2.1 Amplitude analysis

Squaring and adding these equations gives us the frequency-response equation:

$$\boxed{\left[ \mu^2 + \left( \sigma - \frac{3\alpha}{8\omega_0} a^2 \right)^2 \right] a^2 = \frac{k^2}{4\omega_0^2}} \quad (2.2.25)$$

**Variation of  $a$  with  $\sigma$ .** To draw the curve illustrating the frequency response of the system, it's easier to solve the above equation for  $\sigma(a)$ :

$$\sigma(a) = \frac{3\alpha}{8\omega_0} a^2 \pm \sqrt{\frac{k^2}{4\omega_0^2 a^2} - \mu^2}. \quad (2.2.26)$$

Example curves of the response amplitude,  $a$ , versus the frequency detuning from resonance,  $\sigma$ , for varying drive levels are shown in Figure 2.1(a). In an experiment with fixed drive amplitude,  $k$ , as the drive frequency,  $\Omega$ , (or effectively the detuning parameter,  $\sigma$ , since  $\omega_0$  is constant for a given system) is swept up and down, the response amplitude exhibits hysteresis because the middle branch is unstable and, therefore, not observed experimentally.

**Peak.** At the peak,

$$\frac{d\sigma}{da} = \frac{3\alpha}{4\omega_0} a \pm \frac{1}{2} \frac{-\frac{k^2}{2\omega_0^2 a^3}}{\sqrt{\frac{k^2}{4\omega_0^2 a^2} - \mu^2}} \rightarrow \infty. \quad (2.2.27)$$

This means that

$$\frac{k^2}{4\omega_0^2 a^2} - \mu^2 \rightarrow 0 \implies a^2 = \frac{k^2}{4\omega_0^2 \mu^2}. \quad (2.2.28)$$

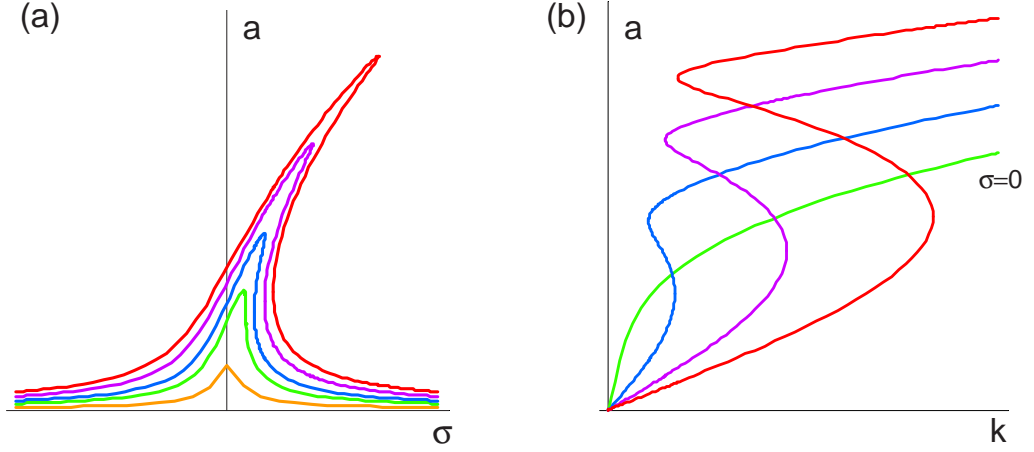


Figure 2.1: (a) Example resonance curves for the fixed  $\alpha$  and increasing driving force illustrating the gradual change in shape. (b) Effect of the drive magnitude,  $k$ , on the response amplitude,  $a$ , for the fixed nonlinear coefficient,  $\alpha$ , and different frequency detuning parameters,  $\sigma$ .

So for the peak, we have

$$a_{peak} = \frac{k}{2\omega_0\mu} \quad (2.2.29)$$

$$\sigma_{peak} = \frac{3\alpha}{8\omega_0} a_{peak}^2 = \frac{3\alpha k^2}{32\omega_0^3\mu^2}. \quad (2.2.30)$$

The dependence of  $\sigma_{peak}$  on  $a_{peak}$  is often called a "backbone curve".

**Variation of  $a$  with  $k$ .** For a fixed frequency detuning,  $\sigma$ , we are also interested in variation of response amplitude,  $a$ , with the magnitude of the drive,  $k$ . The response of the system,  $a$ , to the drive,  $k$ , for different frequency detuning,  $\sigma$ , from the resonance is shown in Figure 2.1(b). In an experiment with fixed drive frequency,  $\Omega$ , as the drive amplitude is swept up and down, the response amplitude exhibits hysteresis.

**Inflection point.** The point of inflection on the curve in Figure 2.1(a) is where the nonlinear curve just starts to lean over. The derivative of amplitude with respect to frequency goes to infinity at that point:

$$\frac{d\sigma}{da} = 2a \frac{d\sigma}{da^2} = 0 \implies \frac{d\sigma}{da^2} = 0. \quad (2.2.31)$$

From equation (2.2.25) we can write down the implicit differentiation:

$$\frac{d}{da^2} \left( \left[ \mu^2 + \left( \sigma - \frac{3\alpha}{8\omega_0} a^2 \right)^2 \right] a^2 = \frac{k^2}{4\omega_0^2} \right) \implies \quad (2.2.32)$$

$$\mu^2 + \left( \sigma - \frac{3\alpha}{8\omega_0} a^2 \right)^2 + a^2 \left[ 2 \left( \sigma - \frac{3\alpha}{8\omega_0} a^2 \right) \left( \frac{d\sigma}{da^2} - \frac{3\alpha}{8\omega_0} \right) \right] = 0. \quad (2.2.33)$$

For the inflection point,  $\frac{d\sigma}{da^2} = 0$ , so equation (2.2.33) becomes an equation for the inflection point amplitude  $a_i$  and frequency  $\sigma_i$ :

$$\mu^2 + \sigma_i^2 - \frac{3\alpha a_i^2}{4\omega_0} \sigma_i + \frac{9\alpha^2 a_i^4}{64\omega_0^2} - \frac{3\alpha a_i^2}{4\omega_0} \sigma_i + \frac{2 \cdot 9\alpha^2 a_i^4}{64\omega_0^2} = 0 \implies \quad (2.2.34)$$

$$\mu^2 + \sigma_i^2 - \frac{3\alpha a_i^2}{2\omega_0} \sigma_i + \frac{27\alpha^2 a_i^4}{64\omega_0^2} = 0 \implies \quad (2.2.35)$$

$$\left( \sigma_i - \frac{9\alpha a_i^2}{8\omega_0} \right) \left( \sigma_i - \frac{3\alpha a_i^2}{8\omega_0} \right) + \mu^2 = 0. \quad (2.2.36)$$

The two points  $(\sigma_i, a_i)$  given by this equation are the two inflection points on the nonlinear curve that are the endpoints of the middle unstable branch. We will show in the next section that this branch is in fact unstable.

When the quadratic equation (2.2.36) above has only one solution for  $a_i(\sigma_i)$ , the two inflection points coincide and correspond to the critical condition for the onset of nonlinearity. This happens when

$$\mathcal{D} = \frac{9\alpha^2 \sigma_c^2}{4\omega_0^2} - 4(\sigma_c^2 + \mu^2) \frac{27\alpha^2}{64\omega_0^2} = 0. \quad (2.2.37)$$

The critical frequency  $\sigma_c$  for the onset of nonlinearity is then given by

$$\sigma_c^2 = \frac{27\mu^2 \alpha^2}{16\omega_0^2} / \left( \frac{9\alpha^2}{4\omega_0^2} - \frac{27\alpha^2}{16\omega_0^2} \right) = 3\mu^2 \implies \sigma_c = \sqrt{3}\mu. \quad (2.2.38)$$

We will call the amplitude of inflection point at the critical drive, critical amplitude  $a_c$ . It can be calculated by solving the quadratic equation (2.2.35) with  $\mathcal{D} = 0$ :

$$a_c^2 = \frac{\frac{3\alpha \sigma_c}{2\omega_0}}{\frac{27\alpha^2}{64\omega_0^2}} = \frac{16\sqrt{3}\omega_0 \mu}{9\alpha}. \quad (2.2.39)$$

We can rewrite the equation (2.2.26) for  $\sigma(a)$  that describes the steady-state resonance curve in terms of  $a_{peak}$  (using equation (2.2.29)) and  $a_c$  (using equation (2.2.39)):

$$\sigma(a) = \frac{3\alpha}{8\omega_0} a^2 \pm \sqrt{\frac{k^2}{4\omega_0^2 a^2} - \mu^2} = \mu \left( \frac{2}{\sqrt{3}} \frac{a^2}{a_c^2} \pm \sqrt{\frac{a_{peak}^2}{a^2} - 1} \right). \quad (2.2.40)$$

**Ratio of  $a_{peak}$  and  $a_c$  at the critical point.** Now, we are interested in the critical magnitude of the drive,  $k_c$ , that drives the system to this critical point. By substituting the expressions for  $a_c$  and  $\sigma_c$  from equations (2.2.39) and (2.2.38) into the frequency response equation (2.2.25), we get

$$k_c^2 = 4\omega_0^2 \left[ \mu^2 + \left( \sigma_c - \frac{3\alpha}{8\omega_0} a_c^2 \right)^2 \right] a_c^2 = \frac{256\mu^3\omega_0^3}{9\sqrt{3}\alpha} \quad (2.2.41)$$

$$\implies k_c = \frac{16\mu\omega_0}{3} \sqrt{\frac{\mu\omega_0}{\sqrt{3}\alpha}}. \quad (2.2.42)$$

Let's evaluate  $a_{peak}$ , given by equation (2.2.29), at the critical point:

$$a_{peak} = \frac{k_c}{2\omega_0\mu} = \frac{8}{3} \sqrt{\frac{\mu\omega_0}{\sqrt{3}\alpha}}. \quad (2.2.43)$$

The ratio of  $a_{peak}$  to  $a_c$  at the critical point is

$$\frac{a_{peak}}{a_c} = \left( \frac{8}{3} \sqrt{\frac{\mu\omega_0}{\sqrt{3}\alpha}} \right) \left( \frac{3}{4} \sqrt{\frac{\alpha}{\sqrt{3}\mu\omega_0}} \right) = \frac{2}{\sqrt{3}}. \quad (2.2.44)$$

### 2.2.2.2 Phase analysis

The steady state equations (2.2.23) and (2.2.24) can be re-written to get a relation between drive-response phase difference,  $\gamma$ , and frequency detuning,  $\sigma$ . From equation (2.2.23), we get

$$a = \frac{k}{2\mu\omega_0} \sin \gamma. \quad (2.2.45)$$

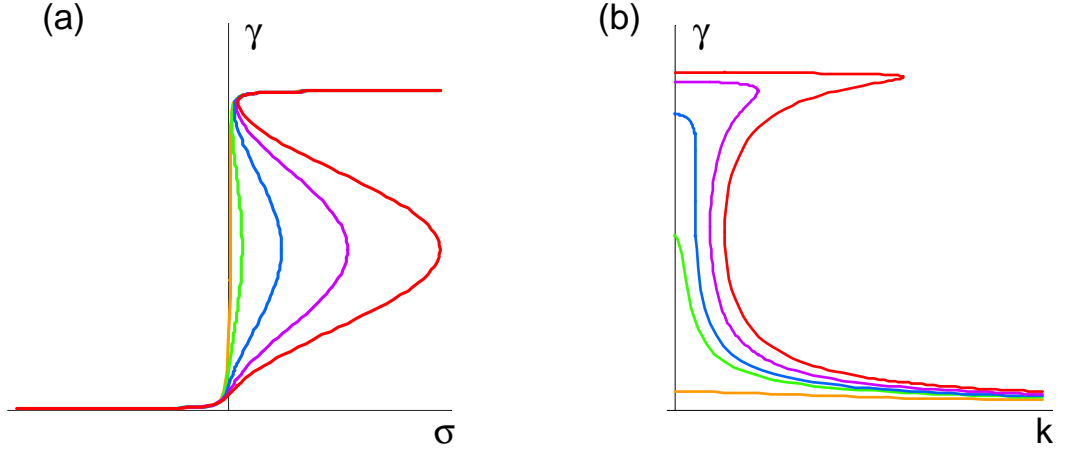


Figure 2.2: (a) Example resonance phase curves for the fixed  $\alpha$  and increasing driving force illustrating the gradual change in shape. (b) Effect of magnitude of the drive,  $k$ , on the response phase,  $\gamma$ , for the fixed nonlinear coefficient,  $\alpha$ , and different frequency detuning parameters,  $\sigma$ .

Substituting this into equation (2.2.24), get

$$\sigma \frac{k}{2\mu\omega_0} \sin \gamma - \frac{3\alpha k^3}{64\mu^3\omega_0^4} \sin^3 \gamma = -\frac{k}{2\omega_0} \cos \gamma. \quad (2.2.46)$$

This equation can be easily solved for  $\sigma$  in terms of  $\gamma$ :

$$\sigma = \frac{3\alpha k^2}{32\mu^2\omega_0^3} \sin^2 \gamma - \mu \cot \gamma. \quad (2.2.47)$$

This relation is illustrated in Figure 2.2(a). In an experiment with fixed drive amplitude,  $k$ , as the drive frequency,  $\Omega$ , (or effectively the detuning parameter,  $\sigma$ , since  $\omega_0$  is constant for a given system) is swept up and down, the relative phase between the drive and the response exhibits hysteresis.

**Inflection points.** The inflection points on the curve shown in Figure 2.2(a) are the jump points in the hysteresis loop during frequency sweeps. It is easy to see from the graph that these points are given by

$$\frac{d\sigma}{d\gamma} = -\frac{3\alpha k^2}{16\mu^2\omega_0^3} \sin \gamma \cos \gamma + \mu \csc^2 \gamma = 0. \quad (2.2.48)$$

Re-writing this equation, we get the condition on the inflection points:

$$\sin^3 \gamma \cos \gamma = \frac{16\mu^3\omega_0^3}{3\alpha k^2}. \quad (2.2.49)$$

**Variation of  $\gamma$  with  $k$ .** For a fixed frequency detuning,  $\sigma$ , we are also interested in variation of response phase,  $\gamma$ , with the magnitude of the drive,  $k$ . It is easiest to write down the expression for  $k^2$  vs.  $\gamma$  from equation (2.2.46):

$$\sigma \sin \gamma - \frac{3\alpha k^2}{32\mu^2\omega_0^3} \sin^3 \gamma + \mu \cos \gamma = 0 \implies \quad (2.2.50)$$

$$k^2 = \frac{32\mu^2\omega_0^3}{3\alpha} (\sigma \sin \gamma + \mu \cos \gamma). \quad (2.2.51)$$

This relation for different values of  $\sigma$  is shown in Figure 2.2(b). In an experiment with fixed drive frequency,  $\Omega$ , as the drive amplitude is swept up and down, the response phase exhibits hysteresis in the same way as the response amplitude does.

**Effect of damping.** When no damping is present, i.e.  $\mu = 0$ , the peak amplitude is infinite. In addition, in the absence of damping, the phase difference between the drive and the response  $\gamma$  follows the relation

$$\mu a = 0 = \frac{k}{2\omega_0} \sin \gamma \implies \gamma = n\pi, \text{ where } n \text{ is an integer.} \quad (2.2.52)$$

From equation (2.2.20), we can see that the response is either in phase or out of phase with the drive because the phase transition at resonance is perfectly sharp.

When damping is present,  $\mu \neq 0$ ,

$$\sin \gamma = \frac{2\mu a \omega_0}{k} \implies \gamma = \sin^{-1} \frac{2\mu a \omega_0}{k}. \quad (2.2.53)$$

Damping changes the phase shift of the response with respect to the drive. In addition, as usual, damping limits the amplitude of response.

### 2.2.2.3 Stability of steady-state motion

The stability of steady-state motion can be explored by determining the nature of the singular points of the time-varying equations (2.2.21) and (2.2.22). To do so we will push the system slightly away from its steady state and see how it behaves.

Let  $a = a_0 + a_1$  and  $\gamma = \gamma_0 + \gamma_1$ , where  $a_0$  and  $\gamma_0$  are the steady-state solution and satisfy the steady-state equations (2.2.23) and (2.2.24).  $a_1$  and  $\gamma_1$  are the small deviations from the steady state. Substituting the expanded expression for  $a$  into the first time-varying equation (2.2.21), we get

$$\begin{aligned} D_1 a_1 &= -\mu a_0 - \mu a_1 + \frac{k}{2\omega_0} \sin(\gamma_0 + \gamma_1) = \\ &= -\frac{k}{2\omega_0} \sin \gamma_0 - \mu a_1 + \frac{k}{2\omega_0} (\sin \gamma_0 \cos \gamma_1 + \sin \gamma_1 \cos \gamma_0) \approx \\ &\approx -\mu a_1 + \gamma_1 \frac{k}{2\omega_0} \cos \gamma_0 \text{ for small } \gamma_1. \end{aligned} \quad (2.2.54)$$

Similarly, substituting the expanded expression for  $a$  into the second time-varying equation (2.2.22), we obtain

$$\begin{aligned} D_1 \gamma_1 &= \sigma - \frac{3\alpha}{8\omega_0} (a_0 + a_1)^2 + \frac{k}{2\omega_0(a_0 + a_1)} \cos(\gamma_0 + \gamma_1) \text{ where } \sigma = \frac{3\alpha}{8\omega_0} a_0^2 - \frac{k}{2\omega_0 a_0} \cos \gamma_0 \\ D_1 \gamma_1 &= \frac{3\alpha}{8\omega_0} a_0^2 - \frac{k}{2\omega_0 a_0} \cos \gamma_0 - \frac{3\alpha}{8\omega_0} a_0^2 - \frac{3\alpha}{8\omega_0} a_1^2 - \frac{3\alpha}{4\omega_0} a_0 a_1 + \\ &+ \frac{k}{2\omega_0(a_0 + a_1)} (\cos \gamma_0 \cos \gamma_1 - \sin \gamma_0 \sin \gamma_1) \approx \\ &\approx -\frac{k a_1}{2\omega_0(a_0 + a_1)} \cos \gamma_0 - \frac{3\alpha a_0 a_1}{4\omega_0} - \frac{k}{2\omega_0(a_0 + a_1)} (\sin \gamma_0) \gamma_1 \approx \\ &\approx \left[ \frac{3\alpha a_0}{4\omega_0} + \frac{k}{2\omega_0 a_0^2} \cos \gamma_0 \right] a_1 - \left[ \frac{k}{2\omega_0 a_0} \sin \gamma_0 \right] \gamma_1. \end{aligned} \quad (2.2.55)$$

By considering only small deviations from the steady state ( $a_1 \ll 1$  and  $\gamma_1 \ll 1$ ) and neglecting terms of order  $a_1^2$  and  $\gamma_1^2$ , we have effectively linearized the problem so that the above two equations

can be written down as a linear system in matrix form:

$$\begin{aligned} \begin{pmatrix} \frac{da_1}{dT_1} \\ \frac{d\gamma_1}{dT_1} \end{pmatrix} &= \begin{pmatrix} -\mu & \frac{k}{2\omega_0} \cos \gamma_0 \\ -\frac{3\alpha a_0}{4\omega_0} - \frac{k}{2\omega_0 a_0^2} \cos \gamma_0 & -\frac{k}{2\omega_0 a_0} \sin \gamma_0 \end{pmatrix} \begin{pmatrix} a_1 \\ \gamma_1 \end{pmatrix} = \\ &= \begin{pmatrix} -\mu & -a_0\sigma + \frac{3\alpha}{8\omega_0} a_0^3 \\ \frac{1}{a_0}(\sigma - \frac{9\alpha}{8\omega_0} a_0^2) & -\mu \end{pmatrix} \begin{pmatrix} a_1 \\ \gamma_1 \end{pmatrix}. \end{aligned}$$

For such a linear system, in general, one can diagonalize the matrix and so obtain a matrix with (complex) eigenvalues,  $\lambda_i$ , on the diagonal that determine the time-evolution of variables,  $\dot{x}_i = \lambda_i x_i$ . The solution of this equation gives the time evolution of a variable:  $x_i(t) = e^{\lambda_i t}$ . If a variable diverges exponentially as it evolves in time according to this equation, we will call this behavior unstable. It's easy to see that the system is unstable in this sense when  $Re(\lambda_i) > 0$  for even one  $\lambda_i$ . The decay of a variable in time corresponds to  $Re(\lambda_i) < 0$ , which describes a stable behavior for the system if true for all  $\lambda_i$ . The oscillatory behavior is also stable and occurs when  $Re(\lambda_i) = 0$ .

We apply this general principle to our system in order to analyze its stability. The characteristic polynomial to find the eigenvalues of the time-evolution matrix is

$$\det(A - I\lambda) = \begin{vmatrix} -\mu - \lambda & -a_0(\sigma - \frac{3\alpha}{8\omega_0} a_0^2) \\ \frac{1}{a_0}(\sigma - \frac{9\alpha}{8\omega_0} a_0^2) & -\mu - \lambda \end{vmatrix} = (\mu + \lambda)^2 + \left(\sigma - \frac{9\alpha}{8\omega_0} a_0^2\right) \left(\sigma - \frac{3\alpha}{8\omega_0} a_0^2\right) = 0.$$

Let's solve this equation for  $\lambda$  to find the eigenvalues. Let

$$\Gamma = \left(\sigma - \frac{9\alpha}{8\omega_0} a_0^2\right) \left(\sigma - \frac{3\alpha}{8\omega_0} a_0^2\right) + \mu^2. \quad (2.2.56)$$

Then the quadratic equation that we need to solve becomes

$$\begin{aligned} \lambda^2 + 2\mu\lambda + \Gamma &= 0 \\ \frac{\mathcal{D}}{4} = \mu^2 - \Gamma &\implies \lambda_{1,2} = -\mu \pm \sqrt{\mu^2 - \Gamma}. \end{aligned} \quad (2.2.57)$$

It is easy to see that when  $\Gamma > 0$ ,  $\sqrt{\mu^2 - \Gamma} < \mu$  and this means that the first root  $\lambda_1 = -\mu + \sqrt{\mu^2 - \Gamma} < 0$  as well as the second root  $\lambda_2 = -\mu - \sqrt{\mu^2 - \Gamma} < 0$ . This means that when  $\Gamma > 0$ , the steady state motion of the system is stable.

However, when  $\Gamma < 0$ ,  $\sqrt{\mu^2 - \Gamma} > \mu$ . This means that the second root of the system is always negative ( $\lambda_2 = -\mu - \sqrt{\mu^2 - \Gamma} < -2\mu < 0$ ), but the first root of the system is positive ( $\lambda_1 = -\mu + \sqrt{\mu^2 - \Gamma} > 0$ ). So the system diverges in time for  $\Gamma < 0$  and is, therefore, unstable.

Let's notice that the expression for  $\Gamma$  (2.2.56) is identical to the expression for the inflection points given in equation (2.2.36). It's easy to see that  $\Gamma$  is positive along the curve except for the middle region between the two inflection points, where it changes sign to negative. Therefore, the condition for instability  $\Gamma < 0$  corresponds exactly to the portion of the curve between the two inflection points.

The analysis of the Duffing resonator equation using the method proposed by Landau and Lifshitz [73] is presented in Appendix A. The results obtained by the Landau and Lifshitz method are equivalent to the results obtained by the method of multiple scales.

## 2.3 Nonlinear NEMS

This section discusses sources of nonlinearity in NEMS beams and cantilevers, and applies theories of elasticity and nonlinearity developed in the previous two sections to the analysis of dynamical properties of NEMS.

### 2.3.1 Sources of nonlinearity

When the oscillations are small, the response of beams and cantilevers can be accurately described by linear equations. However, as the displacement amplitude increases, nonlinear effects become significant. Nonlinearities in both MEMS and NEMS devices have been widely observed experimentally [56, 21, 70, 1]. The sources of nonlinear behavior in vibrating elastic beams include material, inertial, geometric, and damping nonlinearities.

Material nonlinearities exist in systems which exhibit nonlinear stress-strain relationships. Since

the stress,  $\sigma$ , and the strain,  $\epsilon$ , satisfy the inequality  $\frac{d^2\sigma}{d\epsilon^2} \leq 0$  for the majority of known materials, nonlinearity of this kind generally will be softening [12]. Nylons and rubber-like materials, including latex, can exhibit stress-strain behavior in which linear and nonlinear effects are of equal importance. In silicon devices, material effects are significant for bulk acoustic wave micromechanical resonators where geometric nonlinearity is not dominant [60]. The material nonlinearities in strings under tension were found to be small, but if they grow more significant, they can influence both the degree of nonlinearity in the overall response as well as its softening or hardening nature [77].

Inertia nonlinearities arise as a result of concentrated or distributed masses in dynamical systems [43, 85]. This type of nonlinearity is present in the equations describing the motion of an elastic pendulum (a mass attached to a massive spring) and those describing the transverse motion of a cantilever beam. During transverse vibrations, every section of a beam undergoes some longitudinal displacement. The influence of the longitudinal force is included in the equations of motion in terms of time derivatives of the displacements, e.g.,  $x(x\ddot{x} + \dot{x}^2)$  for beams [12]. Other examples of inertia nonlinearities include centripetal and Coriolis acceleration terms. Longitudinal inertia nonlinearities are softening [5].

Geometric nonlinearities arise from nonlinear strain-displacement relationships due to large deformations and are usually of the hardening type. This type of nonlinearity is present, for example, in the equation governing the large-angle motion of a simple pendulum, in the nonlinear strain-displacement relations due to mid-plane stretching in strings, and due to nonlinear curvature in cantilever beams. The geometric nonlinearity in a beam becomes significant when the vibration amplitude grows so large that the tension in the beam becomes dependent on its displacement from the equilibrium position. In order to account for the geometric nonlinearity, the displacement-dependent tension should be included in the equation of motion (2.1.1) in addition to a constant residual tension,  $T_0$ , that might be present in the beam [74]. In doubly-clamped beams, the curvature of a vibrating beam is small, so inertia nonlinearities due to longitudinal forces are generally much smaller than geometric nonlinearity due to midplane stretching. This tension nonlinearity is responsible for the hardening nonlinear behavior for all modes of a doubly-clamped beam.

In singly-clamped cantilevers, where one end is free to move longitudinally and curvatures can be quite large, the effective nonlinearity depends on the contributions of both inertia and geometric nonlinearities, which are usually of the same order [29]. In contrast to doubly-clamped beams, the geometric nonlinearity in cantilevers is dominated by large curvature rather than stretching [3]. The contributions of two types of nonlinearity vary with the mode number. The fundamental mode is dominated by the geometric nonlinearity, which is of the hardening type [89, 3]. For the second and higher modes, the nonlinearity due to nonlinear longitudinal inertia, which is of the softening type, becomes dominant [5, 89, 3].

Nonlinear damping is perhaps the most difficult to describe theoretically because there is a large number of factors and complex processes that could reduce the effect of linear damping on the system. Nonlinear damping usually adds a term of the form  $x^2\dot{x}$  to the equation of motion [12, 80]. It has also been suggested that different nonlinear damping models need to be considered for different modes [3].

Nonlinearities can also appear in the boundary conditions. A nonlinear boundary condition exists, for instance, in the case of a cantilever attached to a flexible support that behaves more like a torsional spring than a fixed clamping point [110]. If cantilevers from nanowires and nanotubes are used in AFM-type tapping mode, nonlinearities in tip-surface interaction become important as well [78].

To further complicate the matter, nonlinearities observed in the system response might be due to nonlinear terms in the drive (e.g., a capacitive drive would produce a softening nonlinearity [122]) or detection scheme. In these cases, both intrinsic system nonlinearities and nonlinearities due to external driving have to be taken into account [61].

### 2.3.2 Dynamic range of beams<sup>3</sup>

This section presents the detailed analysis of a beam with the tension nonlinearity. We show how the onset of the nonlinear regime decreases with decreasing diameter, while the thermomechanical

---

<sup>3</sup>The work in this section has been done together with Henk Postma and Ali Husain and published in Applied Physics Letters [92].

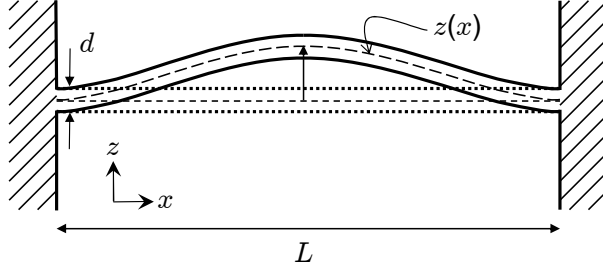


Figure 2.3: Schematic representation of a doubly-clamped nanomechanical resonator of length  $L$  and diameter  $d$ . An applied force leads to a bending profile  $z(x)$ .

noise increases with aspect ratio. We conclude that the useful linear dynamic range of such devices is severely limited, with the result that many applications will involve operation in the nonlinear regime.

A typical layout for a doubly-clamped nanomechanical resonator is shown in Figure 2.3. The resonator can be driven and detected in several ways, e.g., magnetotomotively [26] or optically [21]. The driving force,  $f(t)$ , leads to a time dependent bending profile,  $z(x, t)$ . I will denote the spatial derivative of  $z(x, t)$  as  $z_x = \frac{\partial z(x, t)}{\partial x}$ . When such a beam is stretched to a displacement  $z(x, t)$ , its total length increases from  $L$  to  $L + \Delta L = \int_0^L \sqrt{1 + z_x(x, t)^2} dx$ . For a slight bending, the square root expression can be expanded in a Taylor series around  $z = 0$ , so that the incremental change in length is given by  $\Delta L = \frac{1}{2} \int_0^L z_x(x, t)^2 dx$ . The extra displacement-dependent tension  $T(z(x, t))$  is then

$$T(x, t) = ES \frac{\Delta L}{L} = \frac{ES}{2L} \int_0^L z_x(x, t)^2 dx. \quad (2.3.1)$$

The full differential equation of motion that includes the geometric nonlinearity in the beam's vibration is

$$\begin{aligned} \mathcal{L}[z(x, t)] &= EI z_{xxxx} - \left( T_0 + \frac{ES}{2L} \int_0^L z_x^2 dx \right) z_{xx} \\ &+ \rho S z_{tt} - f(x, t) = 0. \end{aligned} \quad (2.3.2)$$

with boundary conditions  $z(0, t) = z(L, t) = z_x(0, t) = z_x(L, t) = 0$ . Here,  $S$  is the cross-sectional

area,  $E$  is Young's modulus,  $\rho$  is the density, and  $I$  is the moment of inertia about the longitudinal axis of the beam. The term in between brackets describes tension in the beam, and is a sum of residual tension,  $T_0$ , and a bending-induced tension, respectively.

Since equation (2.3.2) cannot be solved exactly, we use the Galerkin discretization procedure [85], representing the solution to equation (2.3.2) in terms of a linearly independent set of basis functions,  $\phi_k(x)$ , where each basis function satisfies the boundary conditions. The error  $e(x, t)$  associated with this approximation technique,

$$e(x, t) = \mathcal{L} \left[ \sum_{k=1}^N z_k(t) \phi_k(x) \right] - \mathcal{L}[z(x, t)] \quad (2.3.3)$$

is required to be orthogonal to each basis function:

$$\int_0^L e(x, t) \phi_n(x) dx = 0. \quad (2.3.4)$$

Performing the integration and noticing that  $\mathcal{L}[z(x, t)] = 0$  as given in the equation (2.3.2), we arrive at the Duffing-type equation describing the time-varying behavior of the system:

$$\ddot{z}_1(t) + \omega_n^2 z_1(t) + \alpha z_1^3(t) = 0. \quad (2.3.5)$$

for free vibrations of the elastic beam ( $f(z(x), t) \equiv 0$ ). The resonant frequency,  $\omega_n$ , is given by equation (2.1.15) and the nonlinear coefficient,  $\alpha_n$ , for vibration in the  $n^{th}$  mode is

$$\alpha_n = -\frac{E}{2\rho L} \frac{\left( \int_0^L \phi_n'(x)^2 dx \right) \left( \int_0^L \phi_n''(x) \phi_n(x) dx \right)}{\int_0^L \phi_n^2(x) dx}. \quad (2.3.6)$$

Using the integration by parts and clamped boundary conditions, the expression for nonlinear coefficients simplifies to

$$\alpha_n = \frac{E}{2\rho L} \frac{\left( \int_0^L \phi_n'(x)^2 dx \right)^2}{\int_0^L \phi_n^2(x) dx}. \quad (2.3.7)$$

Clearly,  $\alpha_n > 0$  for all modes. This means that the geometric nonlinearity due to the appearance

of displacement-dependent tension is hardening and results in nonlinear frequency pulling to higher frequencies for larger drive powers.

We are interested in the response of the beam at resonance when the first mode is dominant, so it suffices to consider the case  $n = 1$ .<sup>4</sup> For a doubly-clamped beam, the simplest function that approximates the first mode is  $\phi_1(x) = \sqrt{2/3} [1 - \cos(2\pi x/L)]$  [38, 112]. The normalization  $\sqrt{2/3}$  ensures that the time dependent amplitude  $z_1(t)$  we find below is the root mean square displacement averaged over the length of the beam (not time). For the fundamental mode,

$$\begin{aligned}\omega_0 &= \frac{4\pi^2}{L^2} \sqrt{\frac{EI}{3\rho S} \left(1 + \frac{L^2 T_0}{4\pi^2 EI}\right)} \\ \alpha &= \frac{E}{18\rho} \left(\frac{2\pi}{L}\right)^4.\end{aligned}\tag{2.3.8}$$

The resonant frequency,  $\omega_0$ , obtained in this approximation is slightly higher than the exact value. We add a phenomenological damping term,  $z_1\omega_0/Q$ , to equation (2.3.5), where  $Q$  is the mechanical quality factor in the linear regime. Then the critical amplitude for the onset of nonlinearity is given by equation (2.2.39) [85]

$$a_c = \omega_0 \frac{L^2}{\pi^2} \sqrt{\frac{\rho\sqrt{3}}{EQ}}.\tag{2.3.9}$$

The critical amplitude describes at what displacement nonlinearity sets in, i.e., the displacement at which the resonance curve just starts to lean over and the hysteresis still has zero width. A smaller value of  $a_c$  signifies an earlier onset of nonlinearity and generally a stronger nonlinear behavior. A nanotube or a nanowire can be well described by a cylindrical rod with diameter  $d$ :  $S = \pi d^2/4$  and  $I = \pi d^4/64$ . We parametrize a rectangular beam with width,  $d$ , in the direction of motion and thickness,  $t$ , yielding  $S = dt$  and  $I = td^3/12$ . This gives us

$$\begin{aligned}a_c &= \frac{2}{\sqrt[4]{3}} \sqrt{\frac{1}{Q} \left(\frac{d^2}{4} + \frac{4T_0}{\pi^3 E} \frac{L^2}{d^2}\right)} && \text{(cylindrical)} \\ a_c &= \frac{2}{\sqrt[4]{3}} \sqrt{\frac{1}{Q} \left(\frac{d^2}{3} + \frac{T_0}{\pi^2 E} \frac{L^2}{td}\right)} && \text{(rectangular)}.\end{aligned}\tag{2.3.10}$$

A typical response of a Duffing oscillator described by equation (2.3.5) is shown in Figure 2.4.

---

<sup>4</sup>More accurate multi-mode Galerkin discretization models have been developed [41], but they do not offer the ease and convenience of deriving analytical dependencies on system parameters.

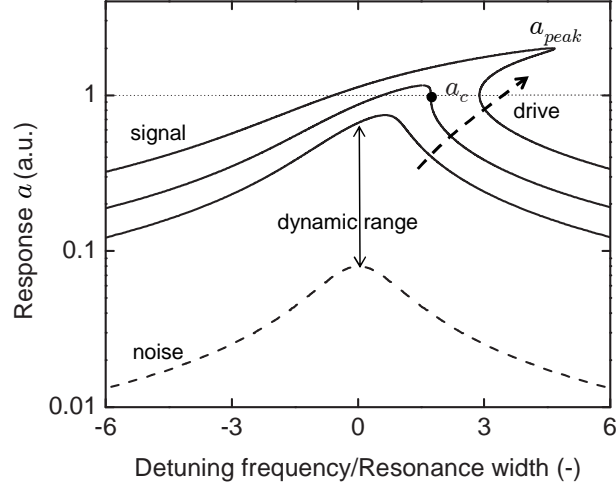


Figure 2.4: Solid lines indicate typical response of a Duffing oscillator as a function of frequency with increasing driving strength. The solid lines are plots of equation  $Q(\omega - \omega_0)/\omega_0 = \frac{2}{3}\sqrt{3}a^2/a_c^2 \pm \sqrt{a_{peak}^2/a^2 - 1}$ , where  $a_c$  is chosen 1, for  $a_{peak} = 0.745, 2/\sqrt{3}, 2$  [85]. The dashed line is a plot for  $a_{peak} = 0.1$ , indicating an arbitrarily chosen RMS noise floor.

At low driving strength, the amplitude has the Lorentzian shape from the linear regime. Increasing the driving strength causes the peak to be pulled over to high frequencies at high amplitudes. A common definition of the onset of nonlinearity is the 1 dB compression point, i.e., the point at which the signal is 1 dB lower than expected for the case of purely linear response. At resonance, this happens when  $a_{peak} = 0.745a_c$ , which is the lowest solid curve in Figure 2.4. This sets the upper limit of the useful linear range.

The lower limit of the dynamic range is set by the incoherent sum of all stochastic processes driving the resonator [27], such as thermomechanical fluctuations, quantum noise, noise from adsorption and desorption of gaseous species [39], and extrinsic sources such as vibrational and instrumental (readout) noise. For simplicity, and in the spirit of considering ultimate thermodynamic limits, we solely consider thermal noise. The spectral density of displacement noise on resonance is

$$S_x = \frac{4k_B T Q}{m\omega_0^3} \quad , \quad (2.3.11)$$

where  $m$  is the total resonator mass,  $m = \pi\rho Ld^2/4$ .

Table 2.1: Input parameters for Figure 2.5.

	$d$ (nm)	$\rho$ (kg/m <sup>3</sup> )	$E$ (TPa)	$Q$
SWNT	1.4	1930	1	1000
MWNT	20	1930	1	1000
Pt nanowire [56]	43	21060	0.168	8500
SiC beam [54]	150( $t = 100$ )	2880	0.430	8000

We now define the useful dynamic range  $DR$  as the ratio of the 1 dB compression point ( $0.745a_c$ ) to the noise amplitude at resonance

$$DR \text{ [dB]} \equiv 20 \log \left( \frac{0.745a_c}{\sqrt{2S_x\Delta f}} \right) , \quad (2.3.12)$$

where  $\Delta f$  is the measurement bandwidth ( $\Delta f = 1$  in Figure 2.5), and the  $\sqrt{2}$  comes from the conversion of  $a_c$  to RMS.

For the moment neglecting the residual tension  $T_0$ ,

$$\begin{aligned} DR &= 20 \log \left( 2.41 d \left( \frac{d}{L} \right)^{5/2} \sqrt{\frac{E^{3/2}}{Q^2 k_B T \Delta f \sqrt{\rho}}} \right) && \text{(cylindrical)} \\ DR &= 20 \log \left( 3.9 \sqrt{dt} \left( \frac{d}{L} \right)^{5/2} \sqrt{\frac{E^{3/2}}{Q^2 k_B T \Delta f \sqrt{\rho}}} \right) && \text{(rectangular)}. \end{aligned} \quad (2.3.13)$$

It is apparent that the dynamic range depends strongly on the aspect ratio  $L/d$  and directly on diameter. Figure 2.5 shows the dynamic range plotted for several device geometries of interest: a single-wall carbon nanotube (SWNT), a multi-wall carbon nanotube (MWNT), a Pt nanowire [56], and a SiC rectangular beam [54] with parameters as given in Table 2.1. We assume a mechanical quality factor,  $Q$ , for MWNT and SWNT of about 1000, although first measurements [99] indicate a lower value. The dynamic range is very limited, and in the case of SWNTs even drops below 0 dB above a length of 2  $\mu\text{m}$ , which renders the device useless as a linear detector. It is worth noting that a change in temperature or measurement bandwidth shifts these curves along the vertical axis, but does not change the scaling behavior. Generally, the resonator with the smallest diameter will have the smallest dynamic range.

We now discuss the effect of residual tension,  $T_0$ . It may arise from differential thermal contrac-

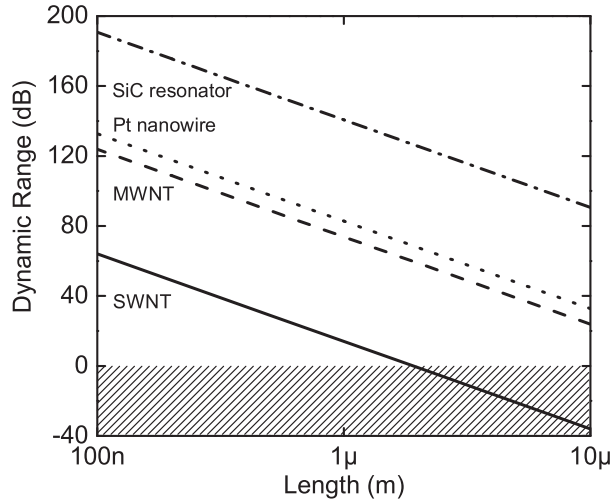


Figure 2.5: Dynamic range at 4K for several doubly-clamped resonators as indicated in the figure and Table 2.1. The shaded region below 0dB indicates the absence of a linear region of operation.

tion [56], or, for instance, may be induced by a DC-voltage on a gate nearby [98]. Increasing tension will increase the resonant frequency. We therefore account for the presence of tension by using  $a_c$  from equation (2.3.9),

$$DR = 20 \log \left( 3.08 \frac{(f_0 L)^{5/2} d \rho}{Q \sqrt{E k_B T \Delta f}} \right) , \quad (2.3.14)$$

where  $\omega_0 \equiv 2\pi f_0$ . The dynamic range can therefore be increased or decreased through a change in resonant frequency due to tension. An upper limit to the frequency tuning is set by how high tension can be before deforming, breaking, or irreversibly pulling the resonator to the gate [32]. This places an upper limit on the available dynamic range, but that limit is strongly dependent on the actual sample geometry, tuning mechanism, and material properties, and is therefore not treated here.

It has been observed that the mechanical quality factor  $Q$  also depends on the dimensions of the resonator, which would alter the scaling behavior presented in this paper. For instance, in an empirical study, it was shown that  $Q$  scales roughly as the inverse of the surface to volume ratio [83]. In another study, it was shown that extra dissipation may also arise from eddy-current damping [26] which scales as  $(Q^{-1} - Q_0^{-1}) \propto (L/d)^3$ , where  $Q_0$  is the quality factor without eddy-current damping. Many other dissipation mechanisms exist, and it is therefore difficult to derive a general

scaling law of  $Q$  with sample parameters.

We have shown that for large aspect ratio resonators, one is forced to work close to the nonlinear regime or even in it, a rather undesirable situation for using nanoresonators as linear sensors. This new nonlinear regime that promises to dominate the nanoscale beyond the conventional dynamic range, however, offers new opportunities for studies and applications of nanoresonators. Several of these opportunities are explored in the later chapters of this thesis.

## Chapter 3

# Experimental Techniques

This chapter discusses fabrication and characteristics of various devices that I have used in nonlinear NEMS experiments and includes gold beams fabricated on silicon nitride, silicon carbide beams, and metal nanowires. This chapter also outlines the transduction schemes that have been used with these devices, including electron-beam detection inside the SEM, magnetomotive transduction, and piezoresistive detection. At the end I discuss a fitting procedure for resonance signals on top of a background that allows us to extract accurate resonant frequency and quality factor.

### 3.1 Devices

Inanimate objects can be classified scientifically into three major categories; those that don't work, those that break down and those that get lost.

---

RUSSELL BAKER

#### 3.1.1 Gold beams on silicon nitride membranes

Gold beams, fabricated on a silicon wafer using silicon nitride membranes, were used during the early stages of nonlinear studies described in this thesis, including the first measurements of mode coupling. Measurements of a beam's vibration were done in the chamber of a JEOL scanning electron microscope (JSM 6400), by scattering the electron beam off an edge of a gold beam and recording the signal reaching the secondary electron detector. This measurement technique will be discussed

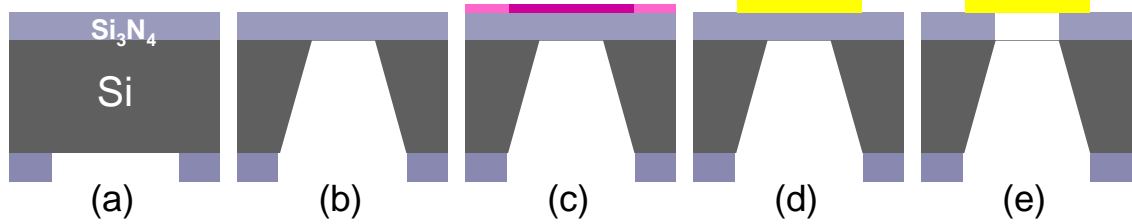


Figure 3.1: Fabrication process for gold beams on top of a silicon nitride membrane. Removal of a square window of silicon nitride on the back side of the wafer (a) allows KOH to etch the silicon layer, leaving a silicon membrane on the top side of the wafer (b). Electron beam lithography is then used to define the structure on top of the membrane (c). After thermal evaporation of gold (d), the silicon membrane is etched away to leave the metal structure suspended (e).

in detail later in this chapter. For these measurements, the gold beams have an advantage of high contrast in the SEM because of the relatively high secondary-electron yield of gold. The biggest disadvantage is the low quality factor of these devices.

The devices are fabricated using bulk micromachining techniques. The process is illustrated in Figure 3.1. We start out with a 500nm-thick silicon wafer covered with a 100nm-thick layer of silicon nitride on both sides. Photolithography is used to define a square hole in the nitride on the back side of the wafer. The mask *SI MEMBRANES* has a choice of four sizes for the square membranes, 0, 50 $\mu\text{m}$ , 100 $\mu\text{m}$ , and 150 $\mu\text{m}$ . For the process I used, the size of the membrane determines the length of the resulting beam. The unexposed photoresist AZ5214 is used in the ECR etch as a mask to clear out the desired square hole (Figure 3.1(a)). For the 2 : 1 mixture of corrosive  $\text{NF}_3$  gas and argon, the double layer of photoresist proved the most effective.

The wafer is then subjected to potassium hydroxide (KOH) at 85 $^\circ$  over several hours, which selectively etches along the 111-plane of the silicon crystal and leaves a square silicon nitride membrane on the front of the wafer (Figure 3.1(b)). The nitride is then covered with PMMA layer so that the desired pattern can be defined by electron beam lithography using a scanning electron microscope (Figure 3.1(c)). Gold with a small addition of palladium is then thermally evaporated onto the wafer surface and, with the help of a chromium adhesion layer, sticks to the silicon nitride membrane where the PMMA has been exposed. The extra metal outside the defined pattern is lifted off when the unexposed PMMA is removed in acetone (Figure 3.1(d)). A small amount of palladium reduces the grain size of the gold film and makes the liftoff easier. Electron cyclotron resonance

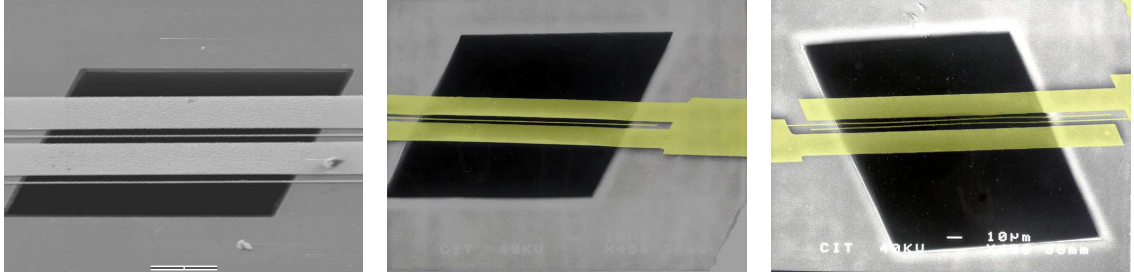


Figure 3.2: Typical gold devices fabricated on silicon nitride membranes. Left: Two suspended gold beams 500nm wide, 200nm thick, and  $50\mu\text{m}$  long positioned  $2\mu\text{m}$  away from gate electrodes. Center: A gold beam 500nm wide, 220nm thick, and  $150\mu\text{m}$  long positioned  $4\mu\text{m}$  away from both gates. Right: A set of two gold beams 500nm wide, 93nm thick, and  $150\mu\text{m}$  long positioned  $4\mu\text{m}$  away from the gate and each other.

(ECR) plasma etching from the backside of the wafer gets rid of the silicon nitride membrane. This leaves the gold structure suspended over the square hole (Figure 3.1(e)). Typical devices made for the studies inside the SEM are shown in Figure 3.2.

### 3.1.2 Silicon carbide beams and cantilevers

Silicon carbide beams with various metal electrode layouts were used for the majority of later experiments, including dynamic range and frequency tuning, multiple mode interaction, and higher flexural modes studies. The vibrations of silicon carbide beams were measured using the magnetomotive driving and detection technique [25] and, for later experiments, using the piezoresistive downmixing scheme [9]. Silicon carbide beams are relatively easy to fabricate and yield devices with sufficiently high quality factors for careful studies of dynamics as well as for application as sensors.

Silicon carbide devices are fabricated by electron beam lithography from single-crystal 3C-SiC layers grown epitaxially upon Si substrate [117]. These wafers were kindly provided by Chris A. Zorman and Mehran Mehregany from Case Western Reserve University. The resonator is defined by electron beam lithography from the SiC layer. A 2-5nm chromium adhesion layer and 15-35nm layer of 60%-40% gold-palladium alloy or gold with an addition of small amount of palladium are thermally evaporated onto the resonator to serve as a conducting electrode layer. Adding palladium to gold reduces the grain size and facilitates liftoff allowing for thinner continuous films. If the metalized pattern is not meant to cover the entire device, a lithographically defined chromium or

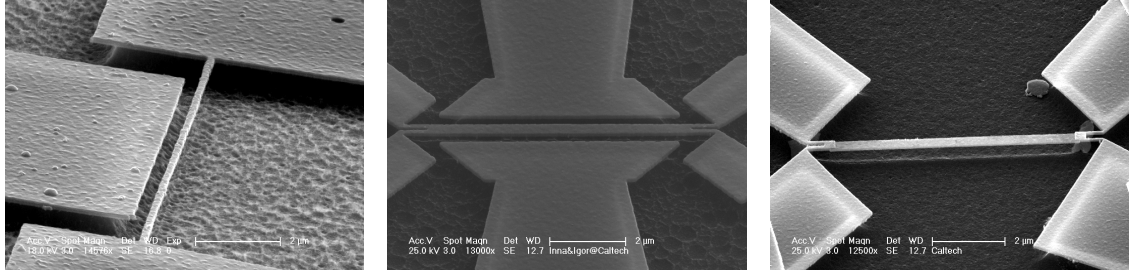


Figure 3.3: Typical silicon carbide devices. Left: A suspended fully metalized SiC beam 150nm wide, 100nm thick, and  $15\mu\text{m}$  long positioned 400nm away from a gate electrode. Center: A metalized beam 300nm wide and  $8.5\mu\text{m}$  long with 750nm-long legs, positioned 350nm away from both gates. Right: A bare SiC beam 300nm wide and  $8.3\mu\text{m}$  long with metal electrode loops.

aluminum mask is used to cover the full structure. The SiC structure is suspended when the Si substrate is partially dry-etched in the ECR. If used, a chromium mask is removed in the chrome etch solution; an aluminum mask is removed in 0.67% KOH solution.

It is usual for built-in strain in an epitaxially grown film and multilayered structure to yield an intrinsic tension within the beam, raising the expected resonant frequency. In theoretical calculations and simulations, the Young's modulus for the silicon carbide film structure is taken to be 430 GPa, which is consistent with the recent measurements [57], and the density is the bulk value of  $3200\text{g}/\text{cm}^3$ .

Figure 3.3 shows typical devices fabricated out of silicon carbide for magnetomotive (left) and piezoresistive (center and right) detection.

### 3.1.3 Metal nanowires

Platinum nanowires have been used to study basins of attraction of a nonlinear nanoresonator in the bistable regime as well as noise-induced transitions between the two accessible states. The vibrations of platinum nanowires were measured using the magnetomotive driving and detection technique [25]. Platinum nanowires are the only bottom-up devices that I have worked with and, besides being an exciting foray into the world of nanoscale self-assembly, they have quality factors comparable with silicon carbide beams. A significant inconvenience, however, is having to locate each nanowire individually after they have been grown so that an electrical contact can be made.

The electroplating setup for growing metal nanowires was originally designed and built by Mladen

Barbic [6, 56] and is suitable for growing platinum, gold, and silver nanowires. Platinum nanowires are synthesized by electrodeposition of platinum into a commercially available nanoporous membrane [82]. SPI-Pore polycarbonate membrane filters, with a nominal pore diameter of 20nm and thickness of  $10\mu\text{m}$ , can be obtained from SPI Supplies ([www.2spi.com](http://www.2spi.com)). Gold is evaporated on one side of the membrane to serve as one of the electrodes for electrodeposition. A platinum electroplating solution (available from Technic, Inc.) fills the holes in the membrane, and the other side of the polycarbonate membrane is covered with aluminum foil, which serves as the second electrode. For gold nanowires, a gold electroplating solution (also from Technic, Inc.) was used. The wires are electroplated by passing a  $20\mu\text{A}$  current between the two electrodes for 3-6 hours, depending on the desired length of the wires. Silver nanowires do not need to be electroplated and can be simply deposited out of a silver enhancement solution (available from Ted Pella) [6]. When the wires are grown, the membrane is dissolved in chloroform, suspending the wires in solution. This suspension is then dried, one drop at a time, upon a silicon substrate that has been capped by 300nm-thick layer of thermally grown silicon dioxide and pre-patterned with gold alignment marks. Using the alignment marks, the location of the deposited wires can be mapped in an optical microscope [6]. Metallic leads (50nm of gold on top of a 5nm Cr adhesion layer) to individual nanowires are patterned by electron beam lithography, evaporation, and lift-off in acetone. Finally, the nanowires are suspended above the substrate by etching  $\text{SiO}_2$  in hydrofluoric acid. In this step the electrode pattern also serves as a self-aligned mask, forming the anchor points from which the nanowires are suspended. Critical point drying, in order to avoid the destruction by meniscus forces, is the final step in fabrication.

## 3.2 Transduction schemes

... nothing tends so much to the advancement of knowledge as the application of a new instrument. The native intellectual powers of men in different times are not so much the causes of the different success of their labours, as the peculiar nature of the means and artificial resources in their possession.

---

SIR HUMPHRY DAVY

During my studies of nonlinear NEMS, I have tried three different transduction techniques to measure the vibrations of mechanical beams: electron beam detection inside a scanning electron microscope; magnetomotive transduction; and, most recently, piezoresistive detection. I include a lengthy description of the electron beam transduction scheme that I developed and implemented inside a JEOL SEM, based on a suggestion by Eyal Buks. Even though this scheme has been used in the past [113, 119], virtually no literature exists that discusses its operation and limitations for detection of NEMS. When the latter became clear to me, I turned to the magnetomotive transduction technique, which was developed in our group [24] and for years has been the standard workhorse for nanomechanical vibration measurements providing femtometer ( $10^{-15}$ m) displacement resolution. Recent interest in employing nanoscale resonators for biological and chemical applications stimulated the development of various room-temperature transduction schemes. In our group, in particular, piezoresistive detection technique was developed [9, 79] and we have recently been able to combine it with thermoelastic actuation to obtain a convenient low-noise technique capable of detecting multiple vibrational modes from several MHz to over 1GHz [7].

### 3.2.1 Electron beam detection<sup>1</sup>

Detection of mechanical vibrations using a scanning electron microscope is analogous to optical detection. Instead of photons from a laser, electrons emitted from a heated filament in a scanning electron microscope scatter off a vibrating mechanical beam. Instead of a photodetector, a sec-

---

<sup>1</sup>Some of the work in this section was done with the help from Eyal Buks, Ronen Almog, Nick Melosh, and Steve Stryker.

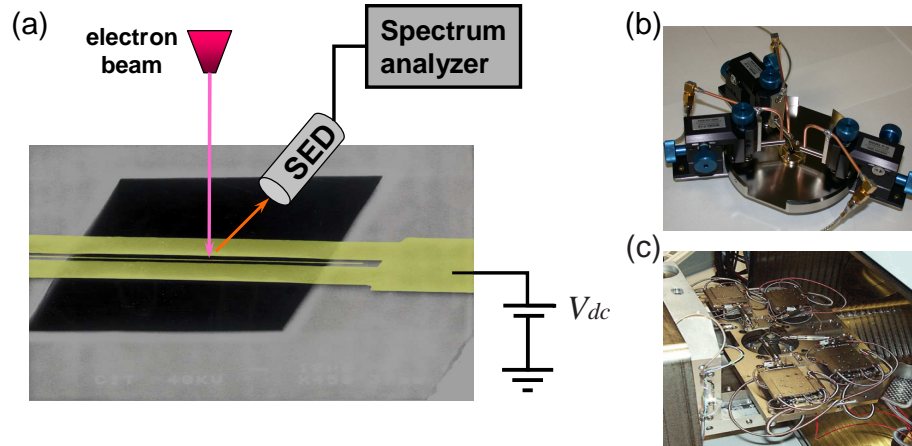


Figure 3.4: (a) Schematic of electron beam detection setup. Electrons scattered off a vibrating NEMS beam are captured in the secondary electron detector (SED) and the signal is fed into a spectrum analyzer. (b) Photograph of the probe station made to make electrical contact to beams for driven resonance measurements inside the JEOL SEM. (c) Commercially available probe station for FEI SEMs.

Secondary electron detector inside the SEM captures the scattered electrons and translates them into an electrical signal. Schematic of an electron beam detection setup is shown in Figure 3.4(a).

### 3.2.1.1 SEM Detector system

When the primary electrons – emitted from the filament, accelerated, and guided through the column – enter the sample, they are scattered elastically (by Coulomb interactions with atomic nuclei) and inelastically (by interaction with atomic electrons). During the inelastic collisions, energy lost by primary electrons is gained by atomic electrons. This acquired energy may enable the atomic electrons to escape from an atom and into the vacuum as "secondary" electrons, which are generated within 1-2nm below the surface of the substrate. The elastically scattered electrons are called "backscattered" electrons and have higher energy than secondary electrons. By convention, the limit between secondary and backscattered electrons is drawn at 50eV [93].

A detection system for secondary electrons used in most SEMs is the Everhart-Thornley detector, developed in 1950s by two graduate students at the University of Cambridge [44]. This detector is inefficient at the conversion of electron-hole pairs into light quanta, but it produces very low noise [93]. The low-energy secondary electrons emitted from the sample are collected in front of a

scintillator by a positively biased grid biased at 20kV. The electrons are further accelerated so that they strike the scintillator surface with enough energy to excite light emission. The current that falls on the scintillator is

$$I_{SE} = I_P \delta f_{SE}, \quad (3.2.1)$$

where  $I_P$  is the electron probe current,  $\delta$  is the secondary electron yield ( $\delta \approx 0.2 - 0.4$  for gold, and depends on the energy of primary electrons and the angle of incidence [104]), and  $f_{SE}$  is the collection efficiency of the detector for secondary electrons ( $f_{SE} \approx 20 - 50\%$  [93]). In general, backscattered electrons also comprise part of the detected signal and the simple formula (3.2.1) is generally much more complicated [93], but since the measurement technique is sensitive primarily to the change of the number of electrons hitting the scintillator, the exact composition of the signal is not very important as long as it is constant in time.

Scintillator, a quartz disk with phosphorus powder coating, converts electrons to photons by cathodoluminescence. When a high energy electron crashes into a semiconductor, electrons in the valence band acquire enough energy to move into the conduction band, leaving behind a hole. When an electron and a hole recombine, it is possible for a photon to be emitted. A large fraction of electron-hole pairs, however, recombine without radiating, and only 1-3% of secondary electrons are converted into light. The emitted light is guided into a photomultiplier tube which amplifies the signal and converts it into an electric signal that is usually fed into the video amplifier of the SEM.

### 3.2.1.2 Experimental setup

The scanning electron microscope JEOL JSM-6400 was used for electron beam detection measurements of gold beams. The measurement of a vibrating beam is done in the spot mode, so that a circular spot shines on the edge of the metal beam and illuminates more and less of it as the beam vibrates. In these measurements, the detector signal, which is usually sent to the video output of the SEM, is sent to an oscilloscope, a network or spectrum analyzer, or a lock-in amplifier.

It is possible to excite thermal vibration of a suspended NEMS beam inside the SEM with an electron beam. A typical thermal spectrum from a vibrating beam is shown in Figure 3.5(a). The

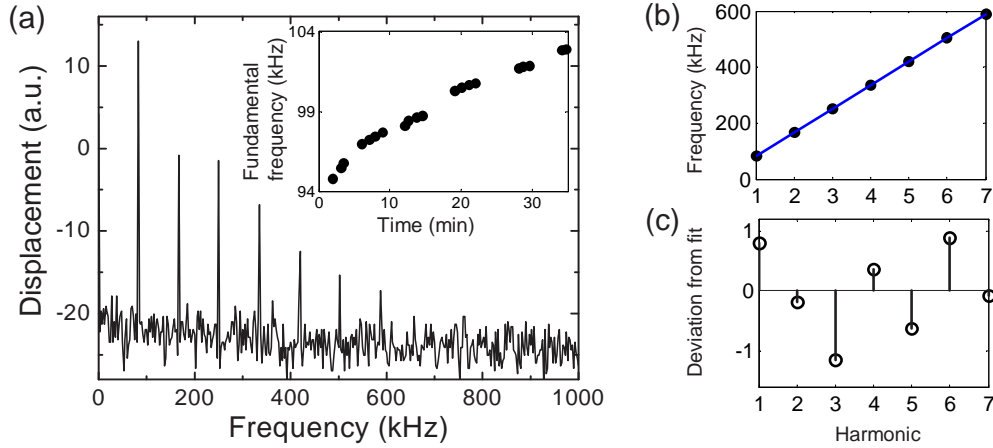


Figure 3.5: (a) Fourier transform of the oscilloscope trace recorded from the secondary electron detector of an FEI SEM. The electron beam, with a current of 150pA at the acceleration voltage of 30kV, was scattered by a gold beam tilted  $45^\circ$  to allow the measurement of the transverse mode. (Inset) The fundamental transverse-mode frequency drifts up with time. (b) Frequencies of the first seven harmonics fitted to a straight line. (c) Deviation of the data points from the fit. Randomness of deviation supports the hypothesis that multiple peaks correspond to higher harmonics of the signal rather than higher vibrational modes.

detected fundamental resonance of 82.5kHz is higher than the predicted frequency of 27.2kHz for the transverse mode of the beam with no tension. A residual tension of about  $0.46\mu\text{N}$  is present in the gold beam due to thermal contraction after high-temperature metal evaporation. The fundamental resonance signal is accompanied by harmonics at multiples of this frequency. These harmonics are an artifact of the detector signal that is not perfectly sinusoidal. All harmonic frequencies can be fitted to a straight line (Figure 3.5(b)). The difference plot between harmonic frequencies and the straight line fit (Figure 3.5(c)) shows no consistent trend that could suggest that evenly-spaced frequencies correspond to higher vibrational modes of a string rather than simply harmonics of the fundamental mode. Moreover, the spectrum is collected while the spot is at a fixed position along the beam (close to the middle), and the signal from higher vibrational modes would show smaller amplitudes for even modes compared to odd modes, which is not observed experimentally.

One of the biggest difficulties with e-beam detection of mechanical resonances is the lack of frequency stability. As shown in the inset to Figure 3.5(a), the fundamental frequency drifted about 1kHz in 30 minutes without reaching a steady state. This drift is most likely due to continuous charging of the gold beam by electrons. The charged beam is pulled to the gate, on which the

opposite charges are induced, increasing the tension and consequently the frequency for the vibration out of the plane of the gate [66]. As electrons keep striking the beam while the measurement is made, no steady state is reached. Simple heating of the beam does not account for the drift as it would decrease the resonant frequency and reach a steady state temperature on the order of milliseconds.

Another difficulty is the formation of contamination carbon growth on the beam at the irradiation spot. The growth rate of carbon is related to the presence of carbon-containing contaminants in the chamber, such as residue pump oil, graphite lubricants, and other organic remnants. Reducing the acceleration voltage to 6kV and the current to 50-100pA slows down the carbon growth.

It is also possible to drive and detect driven vibrations of beams in the SEM. In order to excite the resonators inside the SEM chamber, I fitted the microscope with a modified flange that included four SMA feedthroughs. With the help from Steve Stryker, I also built the probe station shown in Figure 3.4(b) to make immediate electrical contact to a device inside the SEM. Hand-sharpened probing needles can be moved with the help of xyz-micropositioners (Model P-10 from Miller Design & Equipment, [www.miller-design.com](http://www.miller-design.com)) to make an electrical contact with the device contact pads and are connected, through the feedthroughs in the flange, to a function generator or a network analyzer. The use of the probe station eliminates the need for wire bonding that is usually necessary to connect the contact pads of the device to contacts on a sample stage. Such probe stations have recently become available commercially with the micropositioners movable by picomotors inside the SEM chamber for more precise positioning (Figure 3.4(c)). Beams inside the SEM were excited capacitively with the ac voltage applied to a nearby gate or the beam itself. Reducing the gap between a gate and a beam makes capacitive excitation more efficient, but lowers the voltage at which the electrostatic pull-in of the beam can happen [90].

### 3.2.1.3 Nonlinearity of the detector response

Since the electron beam measurement technique aims at measuring the nonlinear response of a vibrating beam, it is important to ensure that the response of the detector is completely linear, so that nonlinearities in the detector response do not adulterate the experimental data.

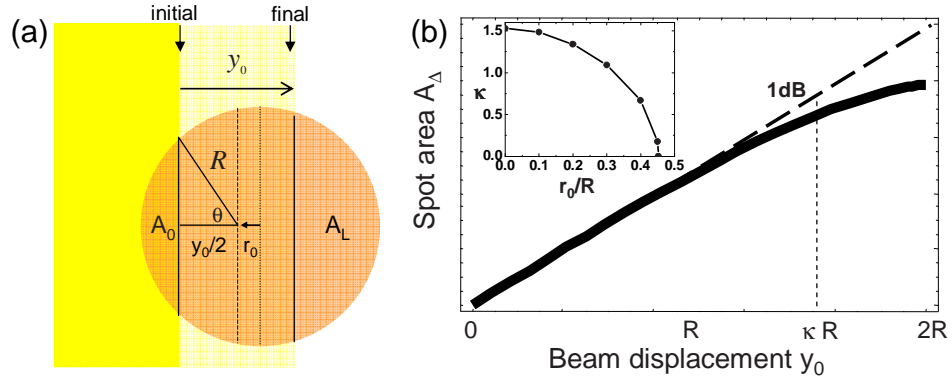


Figure 3.6: (a) Schematic for estimating the nonlinearity in detector response in the scanning electron microscope measurement scheme.  $R$  is the radius of an electron beam spot;  $y_0$  is the displacement of the center of a metal beam;  $r_0$  is the distance by which the mean of vibration amplitude is displaced from the center of the circle.  $A_0$  is the area of the metal beam that reflects electrons into the detector before the beam is displaced;  $A_L$  is the area of the electron spot that doesn't reflect anything into the detector when the beam is deflected. (b) The response measured with a round spot exhibits a 1dB compression from the linear response at  $y_0 = \kappa R$ , where  $R$  is the spot radius and  $\kappa$  is a coefficient that depends on where in the spot the vibrating edge of a metal beam was positioned. The inset shows the falling off of the coefficient  $\kappa$  with the scaled distance from the origin,  $r_0/R$ .

In the usual measurement, the magnification of the microscope is adjusted so that the displacement of a vibrating beam is less than the diameter of the electron beam spot, but is large enough compared to the spot size to result in a visible signal. During the measurement, the metal beam covers less or more of the electron beam spot of radius  $R$  when it vibrates and so reflects less or more electrons into the detector. I will assume that the voltage measured out of the secondary electron detector is proportional to the number of reflected electrons, and so to the area on the metal beam that reflected them.

The spot is usually positioned half-way along the beam where the deflection is expected to be the largest, so that the measured displacement  $y_0 \leq \max[y(x, t)]$ . I also try to position the edge of the metal beam in the center of the spot, so that vibrations are symmetric with the respect to the origin. However, this is not always possible to do accurately and some displacement off the center of the spot, which I will call  $r_0$ , is expected. This situation is illustrated in Figure 3.6(a). If the spot were not a circle, but a rectangle, we would expect a perfectly linear response  $V_{detector} \propto 2Ry_0$ . The nonlinearity in the detector response is due to the circular shape of the spot that results in a smaller signal for larger deflections from its central axis. In order to estimate where this nonlinearity sets

in, we need to calculate the areas of the metal beam illuminated by the circular spot at its minimum (i.e., initial) and maximum (i.e., final) deflections.

Let's call  $A_0$  the area of the metal beam that is illuminated initially. From simple geometric considerations, the area of segment  $A_0$  is

$$A_0 = R^2 \arccos\left(\frac{y_0/2 + r_0}{R}\right) - \left(\frac{y_0}{2} + r_0\right) \sqrt{R^2 - \left(\frac{y_0}{2} + r_0\right)^2}. \quad (3.2.2)$$

When the beam is deflected, the illuminated area now is  $A_{circle} - A_L$  (see Figure 3.6(a)), where  $A_L$  is

$$A_L = R^2 \arccos\left(\frac{y_0/2 - r_0}{R}\right) - \left(\frac{y_0}{2} - r_0\right) \sqrt{R^2 - \left(\frac{y_0}{2} - r_0\right)^2}. \quad (3.2.3)$$

The total change in the area that reflects the electrons,  $A_\Delta = \pi R^2 - A_L - A_0$ , is proportional to the detected signal. This difference in the spot areas is plotted in Figure 3.6(b) as a function of the metal beam displacement. The signal is linear until a certain point, after which the response becomes compressed. A common definition of the onset of nonlinearity is the 1dB compression point, i.e., the point at which the signal is 1dB lower than expected for the case of purely linear response. Let's say that this 1dB compression point occurs when  $y_0 = \kappa R$ , where  $\kappa$  is a coefficient that depends on the how far from the central axis of the circle the edge is placed. The inset to Figure 3.6(b) shows how this coefficient falls off with the distance of the original location from the center of the spot. Typical spot sizes range from 50-70nm in older scanning electron microscopes (e.g., JEOL JSM 6400) to 20nm and less in newer SEMs (e.g., FEI Quanta and Sirion).

The effect of the edge of the metal beam being off the central axis of the spot is dramatic. For the perfect placement in the spot, nonlinearity sets in at the beam displacement  $y_0 = 1.53R$ , an easily avoided regime for most nanoscale and microscale devices (it's about 30nm for a 20nm spot). For an offset of 45% from the origin, nonlinear response appears already at  $y_0 = 0.174R$ , about 3nm for a 20nm spot, a length scale at which device nonlinearity sets in most doubly-clamped nanoscale beams. For an offset of 45.4%, the response of the detector is always nonlinear. It is very important to take extreme care not to deviate from the central position in the spot too much. Going to a

bigger spot size is also a solution, but it comes at the expense of the signal magnitude because the differential change in the number of reflected electrons is smaller for bigger spot sizes.

If the nonlinearity of the detector starts to become a problem for small spot sizes, a useful trick is to adjust the stigmatism of the SEM column lenses so that the spot is elliptical instead of circular, with its major axis aligned perpendicular to the direction of metal beam vibration. This should allow for a wider range of displacement in the linear regime without sacrificing resolution.

#### 3.2.1.4 Detector bandwidth

Another potential limitation of this detection scheme for high-frequency vibrations of NEMS beams is that the Everhart-Thornley secondary electron detectors in the current SEMs have a bandwidth of about 10 MHz [93]. The bandwidth is limited by the response time of the attached pre-amp and the scintillator material. It is possible to replace these components and improve the time resolution of the detector by an order of magnitude, pushing the bandwidth to about 100 MHz [47].

Achieving detection of GHz signals with the SEM measurement technique might be possible if we use the voltage contrast technique developed for non-contact testing of integrated circuits [51]. The voltage contrast technique for testing ICs operates on the basic principle that the emission of secondary electrons by a sample bombarded with the primary electron beam of a SEM is restricted or enhanced by the presence of local electric fields within the circuit. This is equivalent to the effect of mechanical vibrations on the emitted secondary electrons. In this technique, the measurement of signals with higher frequencies utilizes a sampling technique pulsing the electron beam. Each pulse of the primary electron beam samples the signal in a specific phase relation. Continuously shifting the phase between the signal and the sampling beam allows an entire waveform to be recorded. This mode promises to provide a bandwidth of several GHz, depending on the e-beam pulse duration and the overall stability [16]. In practice, the beam-blanking system of the SEM will have to be modified to allow sufficiently fast and accurate control.

### 3.2.2 Magnetomotive drive and detection

Magnetomotive drive and detection technique was developed in our group by Andrew Cleland about 10 years ago [24]. In magnetomotive technique, a conducting beam of length  $L$  is placed in vacuum in a uniform magnetic field  $B$ , with its longitudinal axis perpendicular to the magnetic field. An alternating current  $I_d(t)$ , driven along the length of the beam and transverse to the magnetic field, generates a Lorentz force,  $F_d(t) = LBI_d(t)$ , that excites vibrations of the beam transverse to its length and the magnetic field direction. The scheme is illustrated in Figure 3.7. The motion of the beam can be described by the equation:

$$\ddot{z} + \frac{\omega_0}{Q}\dot{z} + \omega_0^2 z = \frac{LB}{m}I_d(t), \quad (3.2.4)$$

where  $z(t)$  is the displacement of the beam,  $\omega_0$  its resonant frequency,  $m$  its mass, and  $Q$  its quality factor that describes the damping in the system. The motion of the beam with an alternating current running along its length generates an electromotive force (EMF),  $V_{EMF}(t) = \xi LB dz(t)/dt$ , that, by Faraday's Law, opposes the flow of current and effectively increases the impedance of the conducting beam on resonance. The geometric constant,  $\xi$ , depends on the mode shape; for the fundamental mode of a doubly-clamped beam  $\xi = 0.83$ . In order to maximize the signal, magnetic fields used for these measurements range from 1 to 8 Tesla, requiring the use of superconducting solenoids operating at the liquid helium temperature of 4K.

The signal read-out from the magnetomotive measurement is the generated EMF (detected as a drop in conductance of the beam on resonance) on top of the drive background. This means that the magnetomotive technique directly measures the velocity rather than the displacement of the vibrating beam, which makes it suitable for detection of very small displacements at very high frequencies. A resonance of 1.03 GHz has been detected using this technique [55].

The beam displacement can be extracted from the measured EMF voltage signal  $V_{EMF}$  as  $z(t) = V_{EMF}(t)/(\xi LB\omega_0)$ . From the equation of motion (3.2.4), the beam's displacement on resonance is

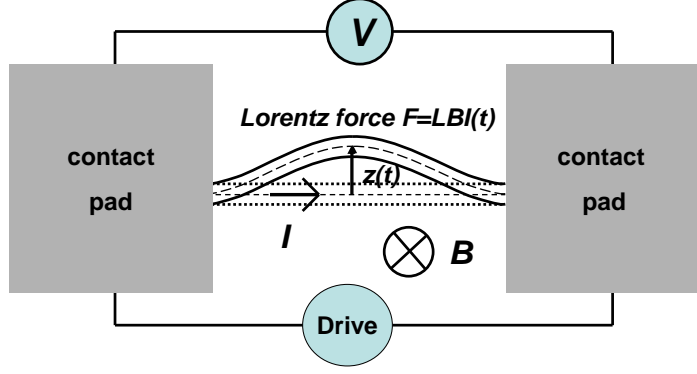


Figure 3.7: Schematic of magnetomotive drive and detection technique. An alternating current runs along the beam transverse to the magnetic field  $B$  and generates a Lorentz force exciting the beam. A vibrating current-carrying beam in the magnetic field produces an EMF voltage read out as a signal.

$z(t) = LBQ/(m\omega_0)I_d(t)$ . Then the measured signal in terms of the driving current is

$$V_{EMF}(t) = \frac{\xi L^2 B^2 Q}{m\omega_0} I_d(t) \equiv R_{em} I_d(t). \quad (3.2.5)$$

Here we have defined the electromechanical resistance of the beam  $R_{em}$  that describes its response on resonance to the driving current. Magnetomotive drive and detection technique can also be described using a circuit model [26], where the electromechanical resistance  $R_{em}$  is part of the complex impedance in the model circuit that behaves like a mechanical resonator.

In general, the EMF generated in the device will also give rise to eddy currents that produce another force opposite to the motion of the beam and has an effect of adding more damping to the resonator [100]. If this damping is significant, the resonator's quality factor measured in the experiment  $Q_{meas}$ , is lower than its intrinsic quality factor  $Q_0$  :

$$\frac{1}{Q_{meas}} = \frac{1}{Q_0} + \frac{1}{Q_{eddy}} = \frac{1}{Q_0} + \frac{\xi L^2 B^2}{m\omega_0 R_e}. \quad (3.2.6)$$

The effect of eddy current damping is negligible if the second term is much smaller than the first one, i.e., if  $R_{em}/R_e \ll 1$ . Unfortunately, this is usually not the case for nanoscale beams and nanowires [53]. The intrinsic quality factor without eddy current damping can then be recovered by

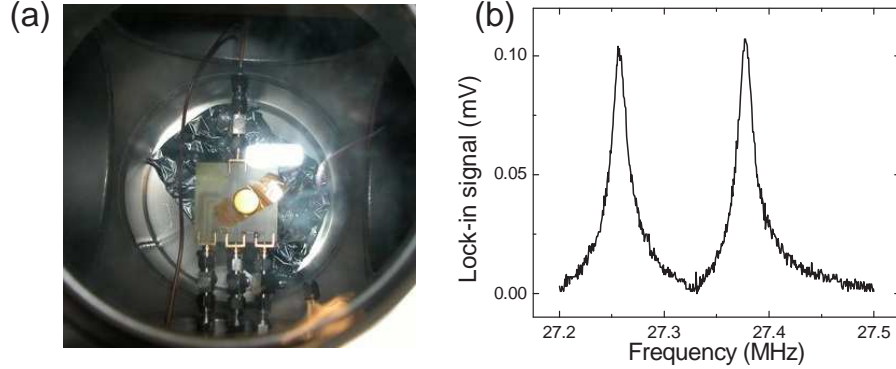


Figure 3.8: (a) Photograph of the room-temperature magnetomotive excitation setup using an  $\sim 0.5\text{T}$  permanent magnet and piezoresistive downmixing detection. (b) Fundamental resonance excited magnetomotively. Two peaks instead of one correspond to the frequency offset between the drive and bias in the piezoresistive downmixing detection scheme.

$$Q_0 = Q_{meas}/(1 - R_{em}/R_e).$$

A major drawback of the magnetomotive technique is the need for a high magnetic field that usually requires operation at low temperatures (maintained by costly and time-consuming liquid helium transfers 2-3 times a week) in a bulky superconducting solenoid (whose size defeats the purpose of nanoscale device dimensions). Another disadvantage is the coupling between excitation and detection producing a large parasitic background, which makes it very difficult to see small resonance signals on top of it. This problem can be partially solved by the balanced bridge technique [40]. Also, only odd-mode detection is possible with the magnetomotive technique due to cancellation of EMF voltages in even modes; moreover, the signals from the third and higher modes are so small that they have never been seen.

### 3.2.3 Magnetomotive drive and piezoresistive detection<sup>2</sup>

We have also developed and implemented magnetomotive excitation coupled with piezoresistive detection at room temperature using a permanent 0.5T magnet. A photograph of the experimental setup is shown in Figure 3.8(a). A permanent magnet taped to the back of the sample stage inside a vacuum chamber and providing a magnetic field transverse to the longitudinal axis of the beam is clearly visible in the photograph. Devices suitable for this technique are similar to the one shown

<sup>2</sup>This work has been done together with Igor Bargatin.

in Figure 3.3(Center)): they are fully metalized and have two contact points at each end that form metal piezoresistor loops. A typical signal from a magnetototively excited beam is shown in Figure 3.8(b). The in-plane resonance of the beam was detected piezoresistively using the downmixing scheme [9], in which a drive and bias voltages, offset by some frequency, mix inside a piezoresistor to produce a low-frequency signal amplified on resonance. The two peaks in the detected signal are offset by this downmixed frequency and correspond to both the drive and bias passing the beam's resonance frequency. This technique is very simple to implement and requires no superconducting solenoids or helium transfers.

### 3.2.4 Thermoelastic drive and piezoresistive detection<sup>3</sup>

Thermoelastic excitation combined with piezoresistive detection is a convenient room-temperature technique for measuring vibrations of nanomechanical beams. In addition to being fully integrated onto a NEMS device, it has an advantage of decoupling detection from the drive and so ensuring a low background. This technique has enabled us to observe resonances of multiple vibrational modes of individual silicon carbide nanomechanical beam resonators, covering a broad frequency range from several MHz to over a GHz.

Figure 3.9(b) shows a schematic of the thermoelastic drive and piezoresistive detection setup. The devices are actuated thermoelastically at room temperature using localized heating in the thicker metal loop. Because of different thermal expansion coefficients of metal and silicon carbide, local heating of a metal loop results in nonuniform expansion and thermal stresses that tend to flex the beam. Periodic temperature variations at drive frequency,  $\omega_d$ , are induced by applying a drive voltage at half the frequency  $\omega_d/2$  to the actuation loop. An AC bias voltage of frequency  $\omega_d - \Delta\omega$  is applied to the detection loop on the other end of the beam. The downmixed signal at frequency  $\Delta\omega$  that is generated in the piezoresistor [9] is amplified by a high-input-impedance preamplifier and detected with a lock-in amplifier. Fractions of the drive and bias RF signals are split off with directional couplers (DC) and fed to a broadband frequency doubler (FD) and mixer in order to

---

<sup>3</sup>This work has been done together with Igor Bargatin and accepted for publication in Applied Physics Letters [7].

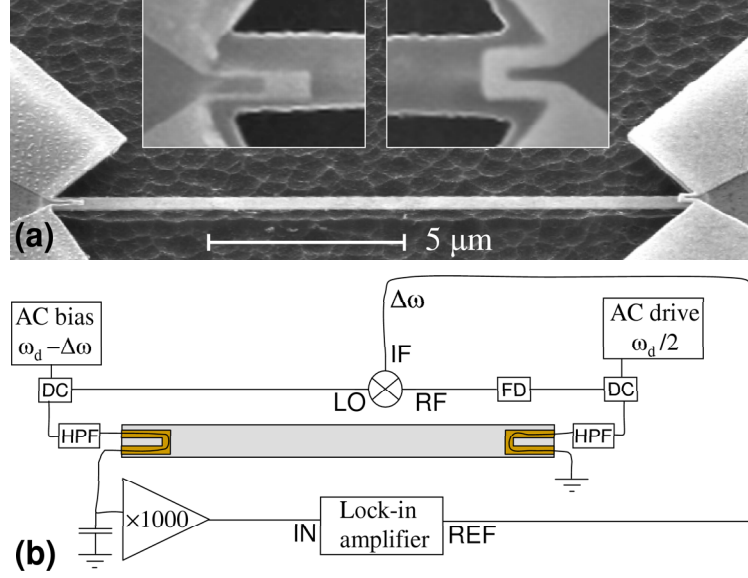


Figure 3.9: (a) Scanning electron micrograph of one of the devices used to implement thermoelastic excitation with piezoresistive detection (oblique view). The insets show top-view closeup images of the drive (right) and detection (left) metal loops. (b) Schematic of the thermoelastic drive and piezoresistive detection setup. Drive loop is heated by voltage at half the resonant frequency. A bias voltage is applied to one side of the detect loop, mixed with the drive voltage by the device, and the downmixed signal is read out from the other side of the drive loop.

produce the reference signal at the downmixed frequency,  $\Delta\omega$ , for the lock-in amplifier.

Piezoresistive detection of motion relies on variation in the resistance,  $\Delta R$ , of the conducting loop, which in metals is largely caused by the changes in the shape of the conductor [79]. The amplitude of the detected downmixed piezoresistive signal is approximately  $V \approx V_b \Delta R / (2R) \approx V_b g \langle \varepsilon_{xx} \rangle / 2$ , where  $V_b$  is the amplitude of the applied AC bias voltage,  $g$  is the effective gauge factor of the piezoresistor, and  $\langle \varepsilon_{xx} \rangle$  is the average longitudinal strain in the detection metal loop.

The measured strain in a beam of thickness,  $t$ , can be converted into displacement by considering the radius of curvature of a bending beam profile,  $z(x)$  [74]:

$$\varepsilon_{xx} = \frac{t}{2R_{curvature}} = \frac{z''(x)}{[1 + z'(x)^2]^{3/2}}. \quad (3.2.7)$$

For small displacements,  $\varepsilon_{xx} \approx z''(x)t/2$ .

The ability to detect multiple modes using this technique can be explained by the fact that the local heating near the clamping point couples to all the possible modes in the structure and that

piezoresistive detection measures strain at the clamping point, rather than displacement or velocity. The strain in the piezoresistive loop gets suppressed when the inflection point in the mode shape occurs in the middle of the piezoresistive loop, but this effect can be engineered by choosing the detection loop size.

### 3.3 Resonant response analysis<sup>4</sup>

Errors using inadequate data are much less than those using no data at all.

---

CHARLES BABBAGE

A small signal on top of a large and often frequency-varying background is a common theme shared by all the transduction schemes described above. Experimental cleverness, filters, and phase shifters can all help in lowering background, but even the best schemes can do no better than the thermal Johnson noise level in the circuit resistors. It is especially difficult to compensate for the background that varies in frequency. This section describes a procedure for accurate extraction of resonance frequency, amplitude, quality factor, and background from the experimental data.

The resonant response of a harmonic resonator is a Lorentzian. The equation of motion of a harmonic resonator is

$$\ddot{u} + \gamma\dot{u} + \omega_0^2 u = K e^{i\omega t}, \quad (3.3.1)$$

where the damping coefficient is inversely proportional to the system's quality factor,  $\gamma = \omega_0/Q$ . Substituting a solution of the form  $u(t) = a e^{i\omega t}$  into this equation of motion, gives us

$$(\omega_0^2 - \omega^2) + i \frac{\omega\omega_0}{Q} = K/a. \quad (3.3.2)$$

We can solve this for the response amplitude as a function of driving frequency  $\omega$ :

$$a(\omega) = \frac{K}{(\omega_0^2 - \omega^2) + i \frac{\omega\omega_0}{Q}}. \quad (3.3.3)$$

---

<sup>4</sup>This work has been done together with Igor Bargatin.

If  $A$  is the resonant peak amplitude, the response at resonance is  $-iA$ . Since the resonator is linear, we can write the drive amplitude,  $K$ , in terms of the response peak amplitude,  $A$ :  $K = A\omega_0^2/Q$ . The resonant response of a linear resonator with zero background is

$$a(\omega) = \frac{A\omega_0^2/Q}{(\omega_0^2 - \omega^2) + i\frac{\omega\omega_0}{Q}}. \quad (3.3.4)$$

If this Lorentzian response is superimposed on a background with a frequency-varying component, then the resonator response will have the following form:

$$R(\omega) = \frac{Ae^{i(\theta_0 - 3\pi/2)}\omega_0^2/Q}{(\omega_0^2 - \omega^2) + i\frac{\omega\omega_0}{Q}} + C_0 + C_1(\omega - \omega_0). \quad (3.3.5)$$

Here, the complex values  $C_0$  and  $C_1$  are the constant component of the background and the slope of the frequency variation, respectively. The phase factor  $e^{i(\theta_0 - 3\pi/2)}$  accounts for the background phase that rotates the circle in the  $xy$ -plane from its zero-background position, with  $a = -iA$ . For convenience, we can incorporate this background phase into the complex amplitude,  $A$ , of the response.

In order to obtain the accurate values for the resonant frequency,  $\omega_0$ , response amplitude,  $A$ , and quality factor,  $Q$ , we need to fit the raw experimental data to the full form of response in equation (3.3.5). The real and imaginary components,  $x$  and  $y$ , have to be fitted separately. This makes for eight parameters over which the fit has to be done:  $A_x, A_y, \omega_0, Q, (C_0)_x, (C_0)_y, (C_1)_x$ , and  $(C_1)_y$ . Because of the number of free parameters, the fit converges in a reasonable time only if the initial guesses are very close to the true values. We will describe below how to obtain good guesses for the initial values of the eight fit parameters.

The initial step is to plot the  $x$  and  $y$  components of the raw data in the  $xy$ -plane. A linear resonator with a Lorentzian response traces out a circle in the  $xy$ -plane with radius,  $R$ . The circle has an experimentally inaccessible gap corresponding to the infinite frequencies in both direction. When there is no background, this gap is centered at the origin and the circle is rotated so that the resonant frequency point (directly opposite the middle of the gap) has coordinates  $(0, -iA)$ , where

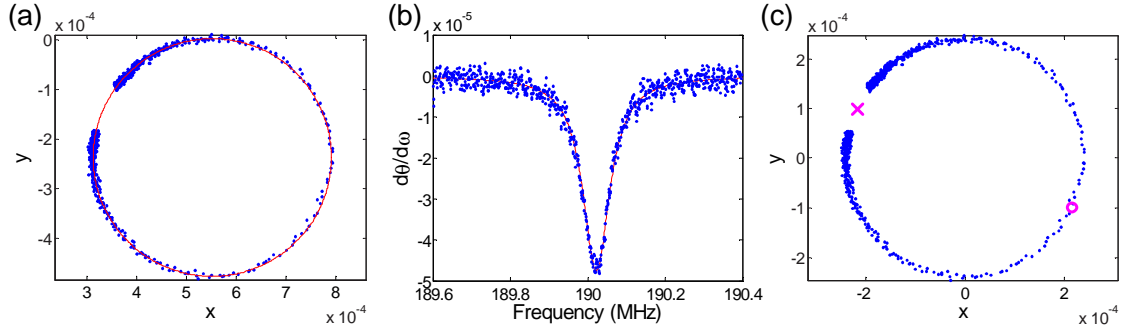


Figure 3.10: Steps in the fitting procedure. (a) Fit (red line) of raw  $x$  and  $y$ -data (blue points) to a circle. (b) Fit of experimental  $d\theta/d\omega$  (blue points) to the theoretical expression (3.3.9) (red line). (c) Background point (magenta cross) is opposite the resonant frequency point (magenta circle) on the re-centered circle.

$A = 2R$  is the peak amplitude. The effect of the background is to shift the circle to other locations in the  $xy$ -plane and rotate it from its zero-background position. The frequency-varying background can also smear out the end segments of the circle trace closest to the gap. When the resonance is nonlinear, a part of the circle appears missing as the sharp drop from one stable state to the other corresponds to a "cut" through the circle.

Raw data is fitted to a circle with radius,  $R$ , and center point,  $(x_0, y_0)$ , as parameters (see Matlab function `circfit.m` in Appendix C and Figure 3.10(a)). The fit works less well for the extreme cases of nonlinear resonance data (when part of the circle is absent) and of fast-varying background (when a large part of the circle is smeared away). The peak amplitude is the diameter of the fitted circle.

The apparent value of  $Q$  is strongly dependent on the background and the guess for  $Q$  obtained from full width at half-maximum of raw power signal is not accurate enough to be used for the full 8-parameter fit. To obtain much more accurate  $\omega_0$  and  $Q$  values, we fit the background-free experimental values of  $d\theta(\omega)/d\omega$  to the theoretical function. Here,  $\theta$  is the phase measured from the center of the circle. The value of  $d\theta(\omega)/d\omega$  is background-free, since we do not need to know the background amplitude when considering the phase and we do not need to know the background phase offset when considering the derivative of the phase with respect to frequency. Experimentally,  $\Delta\theta/\Delta f$  can be derived by projecting experimental points onto a tangent to the circle and estimating

$\Delta\theta$  as the projected distance between them divided by the circle radius. This gives

$$\frac{\Delta\theta}{\Delta f} = \frac{(x_i - x_0)(y_{i+1} - y_{i-1}) - (y_i - y_0)(x_{i+1} - x_{i-1})}{2\Delta f/R^2}, \quad (3.3.6)$$

where  $\Delta f$  is the frequency difference between two adjacent data points.

Theoretically,  $d\theta(\omega)/d\omega$  can be derived from the Lorentzian with no background (3.3.4) as follows: The phase angle  $\phi(\omega) = \arctan(\text{Im}[a(\omega)]/\text{Re}[a(\omega)])$  is measured from the background point (the origin for no-background Lorentzian (3.3.4)) and the x-axis. We don't know exactly where this background point is for the experimental data, so we will look instead at the phase angle,  $\theta$ , measured from the center of the circle,  $(x_0, y_0)$ . From simple geometrical considerations,  $\theta = 2\phi$ , so that

$$\theta = 2 \arctan\left(\frac{\text{Im}[a(\omega)]}{\text{Re}[a(\omega)]}\right) = 2 \arctan\left(-\frac{\omega\omega_0}{Q(\omega_0^2 - \omega^2)}\right). \quad (3.3.7)$$

The derivative with respect to frequency  $\omega$  is

$$\frac{d\theta}{d\omega} = -\frac{2Q\omega_0(\omega_0^2 + \omega^2)}{\omega^2\omega_0^2 + Q^2(\omega^2 - \omega_0^2)^2}. \quad (3.3.8)$$

Substituting  $\gamma = \omega_0/Q$  as in equation (3.3.1) and using the fact that  $\omega$  is the same order as  $\omega_0$  to make an approximation  $\omega + \omega_0 \approx 2\omega$  and  $\omega^2 + \omega_0^2 \approx 2\omega^2$ , we can simplify the expression (3.3.8) to

$$\frac{d\theta}{d\omega} = -\frac{4\gamma}{\gamma^2 + 4(\omega - \omega_0)^2}. \quad (3.3.9)$$

This expression, in the form of  $d\theta(\omega)/df$ , is used in `fitdtheta.m` to fit the experimental values of  $\Delta\theta/\Delta f$  (Figure 3.10(b)) and extract the values for  $f_0$  and  $Q$  from these fits. The estimates for constant background values,  $(C_0)_x$  and  $(C_0)_y$ , are obtained from the point opposite the resonance frequency point on the circle (Figure 3.10(c)). The initial guess for the slope of the frequency-varying background is usually zero. The extracted parameters are then used as initial guesses in the eight-parameter fit to the Lorentzian function (3.3.5) to obtain the accurate values for amplitude,

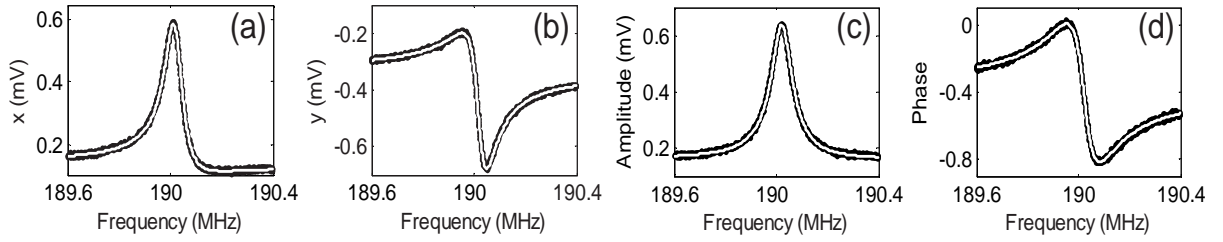


Figure 3.11: Example of the fits (white line) obtained with the fitting procedure applied to piezoresistively detected tenth-mode resonance data (black points) of a doubly-clamped beam for x-quadrature (a), y-quadrature (b), amplitude (c), and phase (d).

resonance frequency, quality factor, and background (`fullresfit.m` and Figure 3.11).

Appendix C lists the Matlab code that implements the fitting procedure described above. The code was successfully tested on the resonant data obtained through different transduction schemes and in different setups. Several options are included in the program to allow for various manual tweaking of parameters when the experimental data is very noisy or incomplete.

## Chapter 4

# Exploring Nonlinear Dynamics with NEMS

In Nature's infinite book of secrecy  
A little I can read.

---

*Anthony and Cleopatra*  
WILLIAM SHAKESPEARE

This chapter describes the experimental studies of nonlinear dynamics performed with nonlinear NEMS resonators. It presents the mapping of the basins of attraction of a nonlinear resonator in its bistable state. I also discuss our studies of the observed transitions between the two stable states of the resonator induced by the environmental and artificially added noise. Since nonlinear regime is readily accessible in nanoscale devices, the details of their dynamical behavior are not only easy and exciting to study, but their understanding is important for proper engineering and analysis of nanoscale systems. Ideas for potential applications of resonators operating in nonlinear regime for enhancing the sensitivity of experimental measurements are presented at the end of the chapter.

### 4.1 Basins of attraction<sup>1</sup>

As discussed in Chapter 2, when a system is driven strongly, the Duffing nonlinearity causes the resonance response curve to become asymmetric. The resonance is pulled either to the right for positive, also known as hardening, nonlinearity (e.g., geometric nonlinearity [74], Figure 4.1(b)) or

---

<sup>1</sup>The work in this section has been done together with Henk Postma, Ali Husain, and Oleg Kogan and will be submitted for publication [67].

to the left for negative, or softening, nonlinearity (e.g., nonlinearities of material [12], capacitive, or inertial [5] origins). When the resonance is pulled far enough to one side, hysteretic behavior is observed as two stable states appear in the system [73]. The stable states, known as "attractors" or "fixed points", correspond to the points in state space to which trajectories originating from initial conditions tend with time. For each attractor, a set of initial states that dynamically evolves to that attractor forms its basin of attraction, which is separated from the rest of the state space by the separatrix curve.

There have been very few experimental studies of basins of attraction because following the evolution of initial conditions in low-frequency macroscopic systems is very time consuming and system parameters tend to drift over the course of many data-taking runs. The previous mappings of basins of attraction [31, 114] used the method of stochastic interrogation, where the system is stochastically perturbed and initial states are sampled at random without fully covering the basins.

This section describes a well-controlled experiment that systematically probes the basins of attraction of two fixed points of a nonlinear, Duffing-type nanomechanical resonator and maps them out with high resolution. Our experiment benefits from the fact that the relevant time scale per data point,  $\sim Q/f_0$ , is very short for high-frequency nanoscale devices, which allows us to take many data points before the parameters of the system drift too much. We also observe the separatrix change shape for varying drive strength, so that one of the basins becomes progressively smaller and eventually disappears. The mapped basins of attraction show a good agreement with theory. However, the observed separatrix is blurred due to ambient fluctuations, including residual noise in the drive system, which cause uncertainty in the preparation of an initial state close to the separatrix.

The device used for mapping the basins of attraction, a doubly-clamped platinum nanowire, is shown in the scanning electron microscope (SEM) photograph in Figure 4.1(a). The nanowire, with a length,  $L$ , of  $2.25\mu\text{m}$  and a diameter of  $35\text{nm}$ , is grown by electrodeposition of platinum into a nanoporous membrane [82]. Gold contact pads on both ends and a gate are fabricated using electron beam lithography, and about  $150\text{ nm}$  of the substrate is subsequently etched away to suspend the device [56]. We actuate and detect the vibration of the nanowire magnetomotively [26] in a magnetic

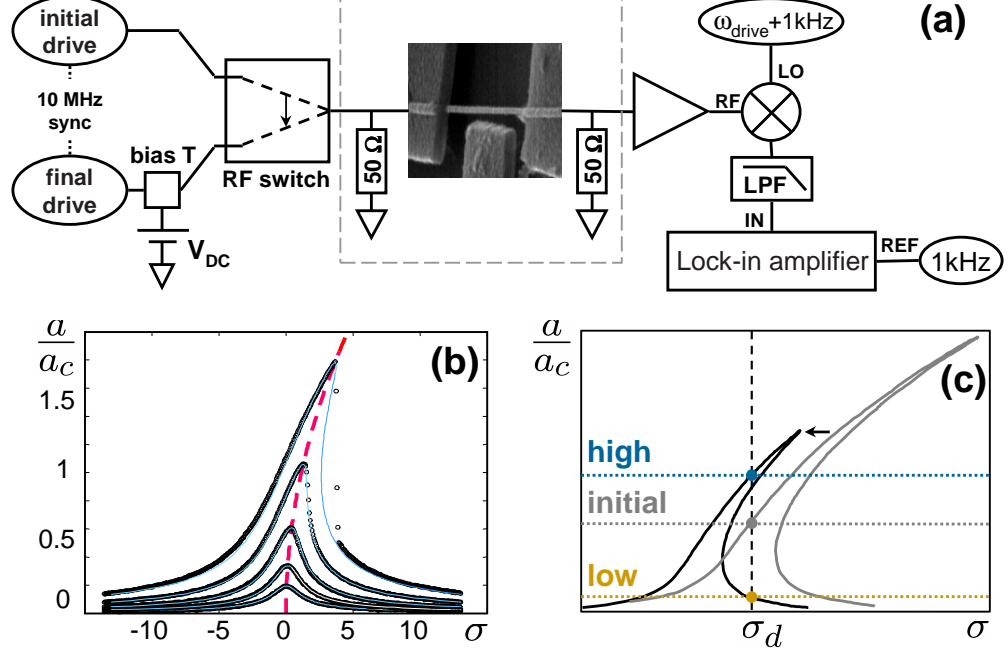


Figure 4.1: (a) Experimental layout. The initial drive prepares an initial state of the platinum nanowire resonator (shown in the SEM photo), a 5ns RF switch is then flipped to connect to the final drive, and the state of the device is measured by a lock-in amplifier after mixing down to a low (1kHz) frequency and filtering the residual RF signal. (b) Vibration amplitude versus frequency, for various driving powers at the sample (-90, -85, -80, -75, -70dBm, or normalized to the critical drive,  $V_c=28.4\mu\text{V}$ ,  $V/V_c = 0.249, 0.443, 0.788, 1.401, 2.492$ ) showing the onset of nonlinearity in the platinum nanowire resonator. We plot the response normalized to the critical amplitude  $a_c$  versus normalized detuning frequency,  $\sigma \equiv 2Q(f/f_0 - 1)$ . The backbone curve (dashed line) connects the maxima of the resonance curves and follows  $(a_p/a_c)^2 = \sqrt{3}\sigma/2$ . (c) The state of the nanowire resonator is first prepared in an initial state on the initial response curve (grey) by choosing an appropriate drive strength for the fixed detuning frequency,  $\sigma_d = 4.26$ . After the RF switch is flipped to connect the final drive, the response curve changes to the one shown in black and the initial state evolves to either the high-amplitude state or low-amplitude state. The small bias voltage, applied to the nanowire together with the final drive, is chosen so that the hysteresis loop of the initial curve is at higher frequency than the operating frequency.

field,  $B = 8\text{T}$ , in a cooled probe in vacuum. The magnetic field is applied perpendicular to the device so that the vibration is in the plane of the gate electrode. At low driving powers the resonance curve is linear, and we extract a resonant frequency of  $45.35\text{MHz}$  and a mechanical quality factor of  $6045$ . The resonant frequency is higher than the expected  $17.71\text{MHz}$  for this device geometry, most likely due to differential thermal contraction between the silicon wafer and the gold contacts that results in residual tension. The ratio of electromechanical impedance,  $R_{em}$ , to electrical impedance,  $R_e$ , is  $0.222$ , which indicates the presence of significant eddy current damping [100]. The quality factor corrected for the eddy current damping is  $Q_0 = Q/(1 - R_{em}/R_e) = 7770$ .

The resonance response of the nanowire to different drives is shown in Figure 4.1(b). With increasing drive power, the resonance is pulled to higher frequencies at large amplitudes, ultimately forming a hysteretic region. The nonlinearity of the device is fully characterized by the critical amplitude  $a_c$ , the point where the resonance curve develops infinite slope,  $da/df(a = a_c) = -\infty$ . The theoretical curves (thin solid lines) in Figure 4.1(b) are generated using the critical amplitude,  $a_c$ , as the only fitting parameter. We determine  $a_c$  by fitting the backbone curve that connects the peaks of resonant curves for different drives to the theoretical expression  $(a_p/a_c)^2 = \sqrt{3}\sigma/2$  [85], where  $\sigma \equiv 2Q(f/f_0 - 1)$  is the detuning frequency scaled by the width of the resonance and  $a_p$  is the peak amplitude. The measured value  $a_c = 2.684\text{nm}$  is in reasonable agreement with the value calculated for our nanowire geometry [92] when the round-trip loss in the experimental circuit is taken into account.

The dominant source of nonlinearity in doubly-clamped NEMS resonators is the additional tension in the beam that appears when vibrations are sufficiently large. This extra tension gives rise to a cubic nonlinearity in the spring constant term in the equation of motion [92], giving it a Duffing oscillator form:

$$\ddot{x} + \frac{\omega_0}{Q}\dot{x} + \omega_0^2(x + \alpha x^3) = F \cos(\Omega t). \quad (4.1.1)$$

Here,  $x(t)$  is the displacement of the beam,  $\omega_0 = 2\pi f_0$  is the resonance frequency,  $\alpha = 8\sqrt{3}/(9a_c^2Q)$  is the nonlinearity parameter [85],  $\Omega = 2\pi f = (\sigma/(2Q) + 1)\omega_0$  is the driving frequency, and  $F$  is the force per unit mass acting on the resonator of mass  $m$ . The driving force in the magnetomotive

transduction scheme is the Lorentz force that acts on the nanowire when a current  $I_d(t)$  is passed through it in a magnetic field,  $F = LBI_d(t)/m$ .

#### 4.1.1 Theoretical analysis

In order to calculate the location of the fixed points and the separatrix in state space, we will obtain the time-dependent solution  $x(t)$  that describes the response of the nonlinear system to a disturbance. In our devices, we can separate the dynamics described by the equation of motion (4.1.1) into two parts: the fast dynamics on time scale of  $1/\omega_0$ , corresponding to the fast oscillations of the undamped harmonic version of the system; and the slow dynamics on a much longer time scale,  $Q/\omega_0$ , associated with a slight detuning,  $\sigma$ , of the driving frequency from resonance as well as damping and nonlinearity (method of multiple scales [85]). Then the solution to the equation of motion (4.1.1) can be written as  $x_0(t, T) = A(T)e^{i\omega_0 t} + \bar{A}(T)e^{-i\omega_0 t}$ , where the slowly varying amplitude  $A(T) = (X(T) + iY(T)) \exp(i\omega_0 \sigma / 2T)$  obeys the envelope equations:

$$\begin{aligned} \frac{dX}{dT} &= -\frac{\omega_0 X}{2} + \frac{\sigma \omega_0}{2} Y - \frac{3\alpha' \omega_0}{2} (X^2 + Y^2) Y \\ \frac{dY}{dT} &= -\frac{\omega_0 Y}{2} - \frac{\sigma \omega_0}{2} X + \frac{3\alpha' \omega_0}{2} (X^2 + Y^2) X - \frac{F'}{4\omega_0}. \end{aligned} \quad (4.1.2)$$

We have assumed here that  $1/Q \ll 1$ , and the slowly-varying amplitude approximation implies that  $\ddot{A}(t)$  terms are negligible compared to  $\dot{A}$  terms.

The slowly-varying amplitude equations describe the nonlinear dynamics of the system and allow us to determine the location of two attracting fixed points and one metastable saddle point in state space for different values of parameters  $F$  and  $\sigma$ , which can be extracted from the experimental data. A set of points in state space that evolve into the saddle point defines the separatrix. To calculate the separatrix, we evolve the initial conditions, lying close to this fixed point and along the negative-eigenvalue eigenvector (which is obtained by linearizing the above equations around the saddle fixed point), backwards in time according to full equations (4.1.2). The curves generated by this procedure constitute the separatrix. To compare these theoretical calculations to the experimental

data in Figure 4.2, we scale computed amplitudes by the calculated value of the critical amplitude,  $a_c$ .

### 4.1.2 Experimental technique and results

As illustrated in Figure 4.1(a), we prepare the system by exciting it with an initial drive power,  $V_i$ , and then switching to a final drive power,  $V_f$ . Two RF sources (HP 8648B for initial and SR DS345 for final drive) are tuned to the same fixed frequency off resonance,  $\sigma_d = 4.26$ , and their internal clocks are synchronized to a 10 MHz clock reference. The phase of the final drive lags behind the initial drive phase by the phase difference,  $\phi$ . By changing the phase difference,  $\phi$ , while holding the initial drive power,  $V_i$ , constant, we can prepare the resonator in the initial states corresponding to a circle in state space. By also stepping the initial drive values,  $V_i$ , we can cover a disk of initial states in state space. We switch from the initial to final drive using a 5ns ( $< 1/f_0 \sim 22$ ns) RF switch (Mini-Circuits ZASWA-2-50DR). After the switch occurs, we measure the final amplitude of the oscillator and mark it as a low or a high final amplitude. In order to access a continuum of initial states, we apply a small DC bias voltage of  $V_{dc} \approx 10$ mV to the wire in the final state. The capacitive interaction with the gate lowers the resonant frequency of the final state [66] so that the hysteretic frequency response of the final state occurs at the same frequency as the single-valued resonant response of the initial state (Figure 4.1(c)). Without this technique, an annulus of states in state space, corresponding to the unstable branch of the initial drive resonance curve, would not be accessible.

To map the basins of attraction in this manner, the initial states were driven with  $-90$  to  $-50$ dBm in 60 concentric circles with 60 phase points per circle, corresponding to a displacement range of 0 to  $2.477a_c$ . Each of the initial states was marked according to the attractor that it evolved to after the switch was flipped: blue for the high-amplitude state and yellow for the low-amplitude state. This data was re-rastered, using the nearest neighbor search algorithm to create a continuous color plot shown in Figure 4.2.

For very low final drives, there is only one state the resonator can be in (refer to Figure 4.1(b)).

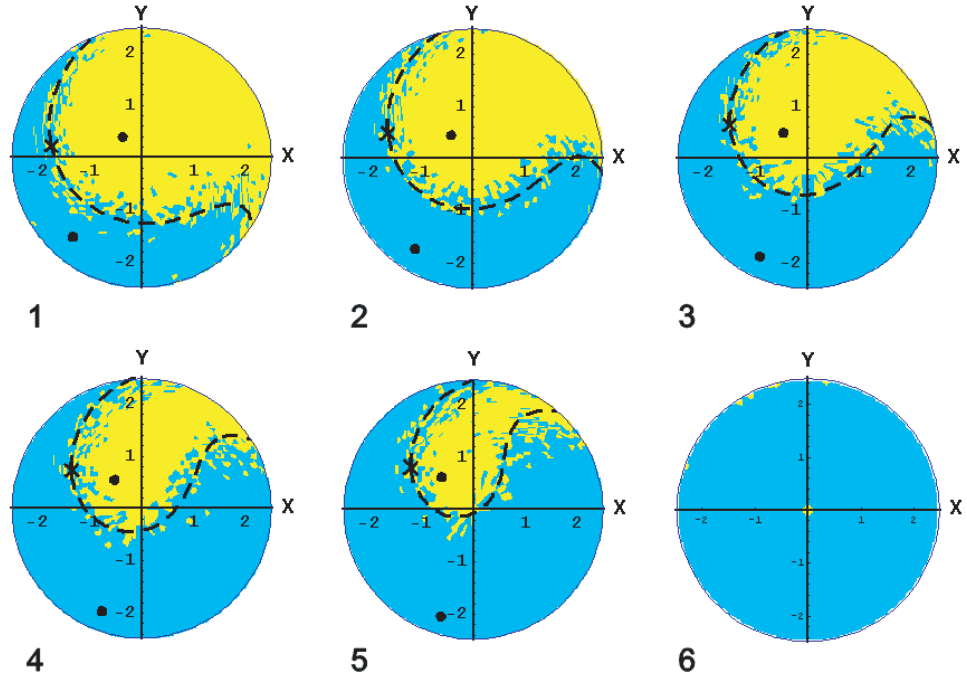


Figure 4.2: Basins of attraction of a nanowire resonator at a fixed frequency,  $\sigma_d = 4.26$ , for increasing final drive values,  $V_f/V_c = (1)1.867, (2)2.049, (3)2.237, (4)2.434, (5)2.640, (6)2.741$ . Blue and yellow colors indicate the final high- and low-amplitude states, respectively. The data consists of 60 concentric circles with 60 points each, corresponding to a displacement range of 0 to  $2.477a_c$ . This data is converted into a continuous plot using the nearest neighbor search algorithm to fill out the space between data points. Theoretical fixed points, saddle point, and separatrix curve are indicated by black points, black cross, and the dashed black curve respectively.

As the final drive starts exciting a nonlinear response, a second basin of high-amplitude stable state appears, but occupies a smaller fraction of the state space (Figure 4.2(1)). When the final drive power is increased, the high-amplitude basins grows, and the low-amplitude basin gets progressively smaller and eventually disappears (Figure 4.2(6)). We can see the disappearance of the low-amplitude state in Figure 4.1(b): a large final drive results in a wider hysteresis region that moves to the right, where the low amplitude branch starts at  $\sigma > \sigma_d$ , and so only the high-amplitude state is available to the system operating at  $\sigma_d$ . The black points in Figure 4.2 are the theoretical fixed points, the black cross is the saddle point, and the dashed black curve corresponds to the theoretical calculation of the separatrix for the experimental parameters used:  $\sigma_d = 4.26$ ,  $(a/a_c)_{max} = 2.477$ , and the first five final drive values scaled by critical drive,  $V_f/V_c$ , listed in the caption. We observe good agreement of experimental data and theoretical calculations for the basins of attraction.

The agreement with theory is best deep inside each basin, far away from the separatrix. Near the separatrix, however, we observe a stochastic variation in the final state. We believe that this blurring of the experimentally observed separatrix is due to ambient fluctuations, most of which are due to voltage noise of about  $5\mu\text{V}/\sqrt{\text{Hz}}$  in the drive circuit <sup>2</sup>.

The experimental mapping of basins of attraction of a nanowire mechanical resonator presented here fills a large gap in our understanding of nonlinear dynamics of nanoscale systems. It was recently shown that precision of some experimental measurements on nanoscale can be improved by deliberately operating the system in nonlinear regime. For example, a nonlinear resonator can be employed to suppress amplifier noise in an oscillator circuit [120], noise-induced switching between two stable states in a nonlinear beam resonator enables precision measurement of the resonant frequency [2], and the sensitivity of a resonator for mass detection is greatly improved when the resonator is driven into a region of nonlinear oscillations [18]. Finally, in a Josephson junction, which is dynamically similar to a mechanical resonator in nonlinear regime, the bistable state of

---

<sup>2</sup>The blurring of the separatrix,  $\delta a/a_c$  is about 0.1, which translates to fluctuations of  $\delta V \approx 2.8\mu\text{V}$  for the measured critical drive,  $V_c = 28.4\mu\text{V}$ . The relevant noise bandwidth for this resonator is  $\pi f_0/Q = 23.6\text{kHz}$ . The noise spectrum that would account for the 10% fluctuation is then  $18.2\text{nV}/\sqrt{\text{Hz}}$ . The residual voltage noise from the initial-drive function generator and the rest of the drive circuit of about  $5\mu\text{V}/\sqrt{\text{Hz}}$  is attenuated by 50.8dBm by the switch and additional attenuators (not shown), and results in the voltage noise of  $14.4\text{nV}/\sqrt{\text{Hz}}$  at the sample. The drive-circuit noise accounts for most, but not all of the observed fluctuations near the separatrix.

the nonlinear system can be used as a bifurcation amplifier to perform a non-dissipative, low-back-action measurement of the phase across the junction [102]. When nanomechanical devices reach the quantum-limited regime [72], a nanomechanical version of such an amplifier could be used for a similar sensitive low-back-action measurement of the state of a quantum mechanical resonator. The knowledge of basin dynamics should prove useful for such precision measurement applications, especially for engineering a nanomechanical bifurcation amplifier.

## 4.2 Noise-induced transitions<sup>3</sup>

In addition to blurring of basins of attraction near the separatrix, we also observed the same noise-induced switching between two stable states as did References [2] and [105], where ambient noise has an effect of shrinking the size of the hysteresis loop and inducing transitions of a resonator from one state to the other near bifurcation points. By adding noise to the resonator drive and recording the statistics of the time it takes for the system to switch when it's near a bifurcation point, we found that the transition rate varies as  $\exp(-E_a/\nu)$ , where  $\nu = k_B T_{eff}$  is the noise power and  $E_a$  is the height of the energy barrier that the system needs to overcome for the transition to happen. The energy barrier depends on the distance to the bifurcation point,  $V_b$ :  $E_a \sim (V - V_b)^\delta$ . We measured the critical exponent,  $\delta$ , to be  $1.8 \pm 0.3$ , which agrees well with the established value of  $3/2$  [71, 35]. This section describes the details of experimental techniques and data analysis.

Measurement of transitions induced by noise in the bistable regime of a nanoscale resonator could give rise to a sensitive experimental technique to detect ambient noise. Adding noise during a specially engineered frequency sweep and inducing appropriate switching could also be used to prepare a resonator in an initial state located on the metastable branch of a nonlinear resonance curve without using the gate [64].

---

<sup>3</sup>The work in this section has been done together with Henk Postma, Ali Husain, and Oleg Kogan.

### 4.2.1 Theoretical results

Fluctuation-induced transitions between two stable states of a system have been thoroughly studied theoretically. For a system in thermal equilibrium, the escape rate from a metastable state can be determined from the height of free-energy barrier [69]. The barrier decreases as the control parameter,  $\eta$ , approaches a bifurcation point,  $\eta_c$ , and the barrier height scales as  $(\eta - \eta_c)^\delta$ , where the critical exponent,  $\delta$ , has been shown to be  $3/2$  [71]. Non-equilibrium systems, such as driven nanomechanical resonators, cannot be characterized by free energy, but transitions between stable states can still be described by an effective energy barrier. Without an assumption of the energy barrier, the analysis of the dynamics of a bistable system near the bifurcation point gives a critical exponent  $\delta = 3/2$  for relatively large detuning from the resonant frequency and  $\delta = 2$  for the operation close to the critical point [35].

Numerical simulations show that the critical exponent,  $\delta = 3/2$ , characterizes also the transitions further away from the bifurcation points, except for the case of very large detuning and hysteresis ( $\sigma > 10$ ), where the critical exponent further away from the bifurcation point is 1 and the behavior is no longer exponential very far from it. This exception applies only to transitions from high- to low-amplitude state [65]. The detuning of this magnitude have not yet been explored experimentally.

In addition to our experimental studies of noise-induced switching in a platinum nanowire mechanical resonator, this phenomenon has been explored in two-mode lasers [94], silicon nitride nanomechanical resonators [2], micromechanical torsional resonators [105], and Josephson junctions [101], as well as in parametrically driven systems (e.g., micromechanical torsional parametric resonators [22] and electron in a Penning trap [75]).

### 4.2.2 Waiting time measurements

There are two ways to gather the noise-induced transition statistics: we can either prepare the system in one state and record the time we have to wait until the transition occurs, or we can sweep drive frequency or amplitude through the bifurcation point and record where the transition happened. A histogram of transitions occurring in a specified time contains the same information

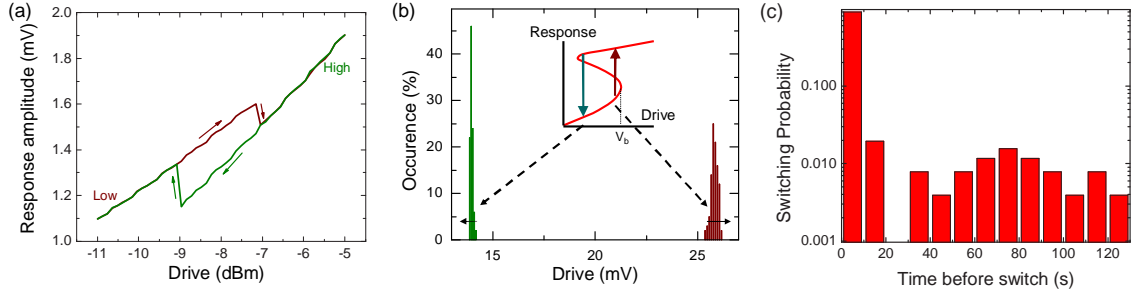


Figure 4.3: (a) Hysteretic response to sweeping drive amplitude corresponding to a theoretical curve in Figure 2.1(b). (b) Histograms of transitions occurring during drive sweeps for both bifurcation points. The drive at the histogram peak corresponds to the bifurcation drive,  $V_b$ . The histogram heights are given as a percentage of the total number of performed sweeps. (c) A histogram of times the system took to spontaneously switch from the prepared low-amplitude state to the high-amplitude stable state, for the right bifurcation point. No additional noise is added to the system. Switching probability is normalized to the total of 256 recorded events.

as a histogram of the number of transitions that occur at different drive points during the sweep if the sweep rate is known.

I will first describe the waiting time measurements that we have performed on the platinum nanowire when we first noticed the spontaneous switching of the system from one state to another near bifurcation points. To explore the dynamics in the hysteretic regime, we excite the resonator at a fixed frequency and change the drive amplitude. We chose to work with the hysteresis in drive amplitude instead of drive frequency in order to avoid phase slips that could occur during frequency stepping with the particular generators that we used. The response to changing drive at various frequency detuning from resonance,  $\sigma$ , is illustrated schematically in Figure 2.1(b). Figure 4.3(a) shows an experimental hysteretic response to changing drive amplitude. Since magnetomotive detection allows us to measure the decrease in impedance on resonance, the raw signal is a resonant dip rather than a peak. Therefore, the experimentally measured lower amplitudes correspond to theoretical high-amplitude branch and vice versa. The proper subtraction of background will make the response look as expected, so we will label the states according to amplitudes in Figure 2.1(b).

The resonator is prepared in the low-amplitude state by driving it with such a low amplitude that its response falls before the onset of hysteresis and is single-valued. Analogously, the resonator is prepared in the high-amplitude state by driving it so strongly that its response is beyond the

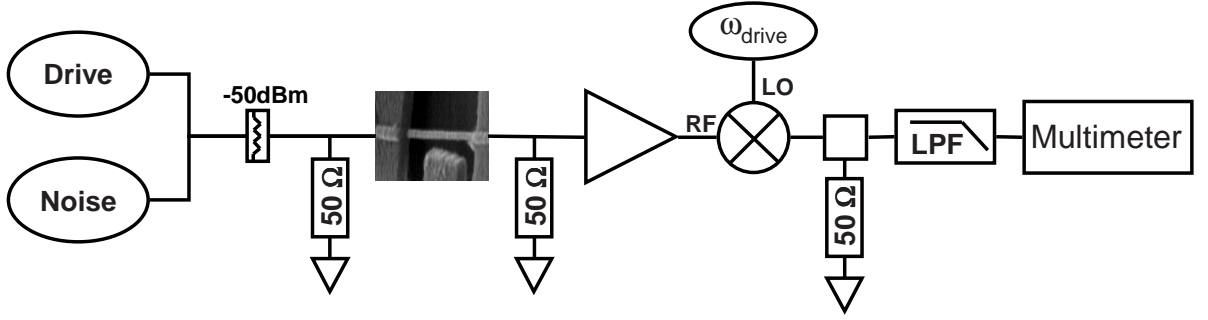


Figure 4.4: Experimental setup to measure the effect of added noise on the transition rate between two stable states of the nanowire resonator.

hysteretic region and can only have high amplitude. The location of the bifurcation point is determined by sweeping the drive and collecting the histograms of where the transition occurred (Figure 4.3(b)) – the peak of the sweep histogram is assumed to correspond to the bifurcation point. After the resonator is prepared in the low-amplitude state, the drive is increased to operate the system slightly before the (right) bifurcation point, where transitions from low- to high-amplitude branch happen. We then record the time that the system takes to switch to the high-amplitude state. The high- to low-amplitude transitions are measured in a similar way, decreasing the drive after initial state preparation. The histograms of switching times at different values of the drive are shown in Figure 4.3(c) for the right bifurcation point (low-to-high amplitude transition). These were observed without any additional noise added to the system and are most likely due to the residual noise in the drive circuit, since the thermal noise in a liquid-helium cooled probe is much less (see Section 4.2.4).

To verify that it is indeed ambient noise that causes the system to switch from one stable state to another, we add white noise (generated by the arbitrary waveform generator Agilent 33250A) to the drive (generated by the function generator HP8648B). The schematic of the setup is shown in Figure 4.4. The noise powers,  $\nu$ , listed in the caption, were chosen to be much higher than thermal noise and any residual drive noise. We can then consider the generated noise to be the prevalent noise in the system setting the switching rates. The reference, generated by sending the signal from the synchronized source SR DS34 at  $\omega_{\text{drive}}/2$  through the frequency doubler, is mixed with

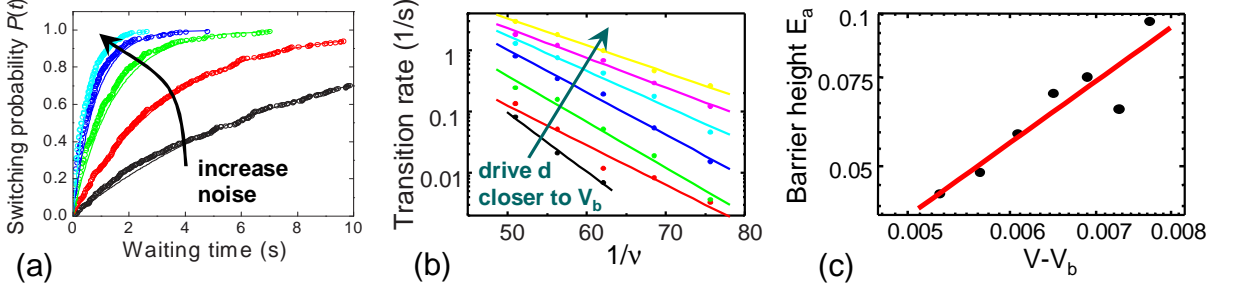


Figure 4.5: (a) Switching probability dependence on waiting times for different powers of added noise. The arrow indicates the direction of increasing noise powers:  $0.115, 0.121, 0.127, 0.133, 0.140V_{rms}$ . (b) Transition rate from the high- to low-amplitude state (plotted on the log scale) as a function of inverse added noise power,  $\nu$ , for different drive detuning from the bifurcation point. Slopes of linear fits give heights of the effective energy barriers. (c) The height of the effective energy barrier,  $E_a$ , as a function of how far from the bifurcation point,  $V_b$ , the system operates (i.e., parameter  $V - V_b$ ). Both variables are plotted on the log scale, so that the slope of the linear fit (red line) gives the critical exponent in the dependence of the energy barrier on proximity to the bifurcation point:  $E_a \sim (V - V_b)^\delta$ . The critical exponent was found to be  $1.8 \pm 0.3$ .

drive to DC, so that the output low- or high-amplitude signal is detected by the digital multimeter Agilent 34401A. The operating frequency is fixed at 45.414MHz. The resonator is prepared in a high-amplitude state, then the drive amplitude is decreased to  $-73.25\text{dBm}$  at the sample to be close to the (left) bifurcation point,  $V_b$ , where the transitions from high- to low-amplitude state occur. The maximum time that we wait for the switch to occur is limited to 10 seconds. The waiting times are tabulated in a histogram similar to those shown in Figure 4.3(b).

For every noise power, we can integrate the histogram data,  $h(t)$ , to obtain switching probability in an elapsed time period:

$$P(t) = \int_0^t h(t') dt'. \quad (4.2.1)$$

The switching probability is plotted in Figure 4.5(a) as a function of elapsed time for different noise powers increasing in the direction of the arrow. The probability,  $P(t)$ , of switching depends on the transition rate,  $\Gamma$ , as [71, 48]

$$P(t) = 1 - \exp\left(-\int_0^t \Gamma dt'\right) = 1 - \exp(-\Gamma t). \quad (4.2.2)$$

The solid curves in Figure 4.5(a) are the fits to this exponential function that allow us to extract

the transition rate  $\Gamma$  for every noise power. We can also plot the probability of remaining in the original state up to time  $t$ ,  $1 - P(t)$ , versus waiting time,  $t$ , on the log scale and extract the rate from the slopes of straight-line fits. Alternatively, we take the derivative of  $P(t)$  in both (4.2.1) and (4.2.2) and then the transition rate,  $\Gamma$ , can be calculated directly from the histogram,  $h(t)$ , as

$$\Gamma(t) = \frac{h(t)}{1 - P(t)} = \frac{h(t)}{1 - \int_0^t h(t') dt'}. \quad (4.2.3)$$

The procedure to determine transition rates for the five noise powers was repeated for seven different drive amplitudes:  $-73.00, -73.05, -73.10, -73.15, -73.20, -73.25, -73.30$ dBm, moving closer to the bifurcation point,  $V_b = -73.95$ dBm. Theoretical analysis of the dynamics [35] gives the exponential dependence of the transition rate,  $\Gamma$ , at a particular driving frequency on noise intensity,  $\nu$ , and the activation barrier height,  $E_a$ , that the system has to overcome for the switch to take place:

$$\Gamma = \Gamma_0 \exp\left(-\frac{E_a}{\nu}\right), \quad (4.2.4)$$

where  $\Delta V = V - V_b$  is the difference between the applied drive,  $V$ , and the drive value,  $V_b$ , at the bifurcation point. The transition rate,  $\Gamma$ , is plotted on a logarithmic scale versus inverse of the added noise power,  $1/\nu$ , in Hz/V<sup>2</sup>, for different drive values in Figure 4.5(b). We can conclude from the straight line fits that  $\ln(\Gamma) \propto -1/\nu$  as expected, and the slopes give the activation barrier heights,  $E_a$ , for different distances to the bifurcation point.

The effective activation barrier,  $E_a$ , decreases as the system approaches the bifurcation point,  $V_b$ . The barrier height scales as  $(V - V_b)^\delta$ . By plotting  $E_a$  as a function of the distance to the bifurcation point  $\Delta V = V - V_b$  on a log-log scale, we can determine the critical exponent  $\delta$  from the slope of the linear fit to be  $1.8 \pm 0.3$ . This value agrees with the theoretical prediction of  $3/2$  [71, 35].

The main disadvantage of the waiting-time method is that waiting for a switch to occur can take a lot of time and performing the experiment can take arbitrarily long. During such long waits, the system parameters could drift and change the state of the system. To limit the time it takes to perform these experiments, we usually set the maximum time we waited for the switch. This

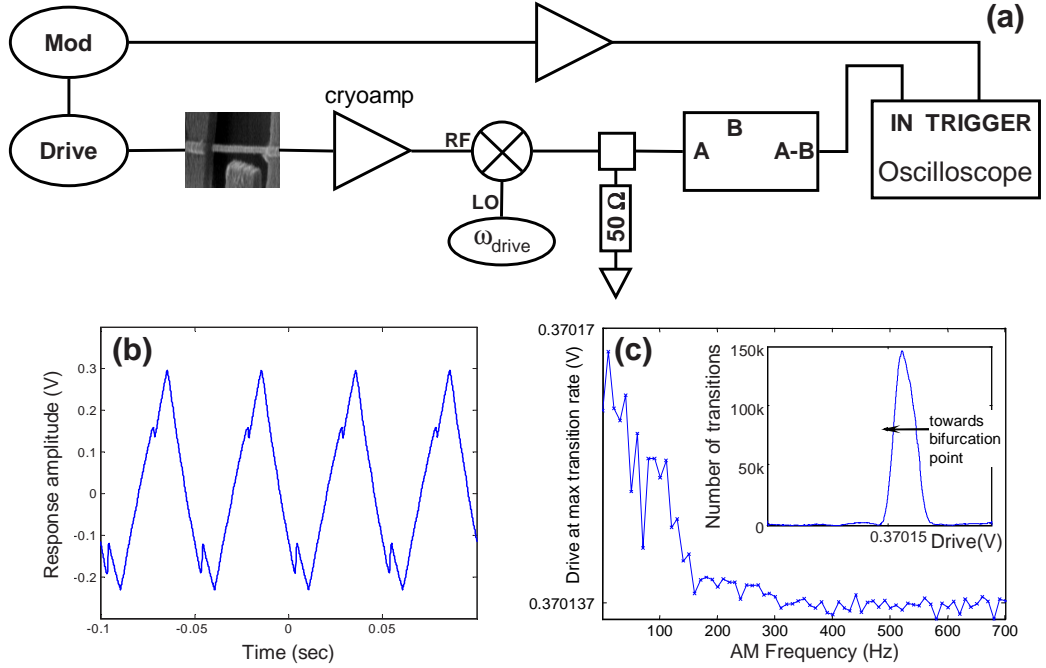


Figure 4.6: (a) Experimental setup to collect the statistics of noise-induced transitions by using amplitude-modulated signal to sweep through both bifurcation points. (b) Oscilloscope signal with both low- to high-amplitude transition, when the drive is swept up, and high- to low-amplitude transition, when the drive is swept down. As above, the magnetomotive detection scheme results in a dip on resonance, so that we measure a higher amplitude for the actual low-amplitude state, but label the states as would be seen for a resonant peak (obtained after the proper background subtraction). (c) (Inset) Sum of all the delta functions for the low- to high-amplitude state transition forms a histogram,  $h(V)$ . The drive is swept up at 111Hz. (Main panel) Drive values at which most transitions occur (histogram peaks) shift towards the bifurcation point,  $V_b$ , as the sweep rate (frequency,  $f_{AM}$ , of the modulation signal) is increased.  $V_b$  can be inferred from the saturation drive value approached at large sweep rates.

technique throws away data at one end of the obtained histograms, somewhat distorts the shape of the switching probability function, and might result in inaccurate values of critical exponent extracted from the experimental data.

### 4.2.3 Sweep measurements

An alternative method is to collect the statistics of state switches by sweeping the drive amplitude through the bifurcation point and recording the drive values at which the transitions happen. An elegant way to do so very fast is to modulate the driving signal by a low-frequency sawtooth-shaped signal. By choosing the amplitude of the modulation signal appropriately, we can sweep through

both bifurcation points in one period of modulation making sure to cover the drives low and high enough so that we prepare the system in either low- or high-amplitude state before recording a switch. This technique highly facilitates and speeds up the collection of noise-induced transition histograms. Figure 4.6(a) illustrates the experimental setup that realizes the amplitude-modulation technique. The low-frequency triangle-shaped modulation signal is produced by function generator HP3325A and sent into amplitude modulation input of the drive generator HP8648B. The signal from the device is amplified by a cryogenic amplifier and mixed down to DC. The SR650 filter is then used to subtract the triangle-shaped modulation signal from the device signal in order to minimize the background. The final signal is measured by oscilloscope Agilent 54625A triggering on the edge of the modulation signal.

The device used in the sweep measurement experiment was fabricated by Philip Feng, and consisted of two suspended metalized silicon carbide beams  $1.70\mu\text{m}$  and  $1.74\mu\text{m}$  long,  $150\text{nm}$  wide, and  $80\text{nm}$  thick. The response of the beams was measured magnetomotively in the bridge configuration [40], using variable attenuators and a voltage-controlled phase shifter to minimize the background for each resonance. The resonant frequencies of the beams were  $395\text{MHz}$  and  $410\text{MHz}$  with  $Q\sim 2400$  at  $20\text{K}$ . In these experiments, the temperature of the device was stabilized for each run using a thermometer, homemade heater, and Lake Shore 340 Temperature Controller.

An example of an oscilloscope trace that we obtained in the measurement is shown in Figure 4.6(b), where jumps at both bifurcation points are clearly visible. The time axis in the graph can be converted to the drive values during the sweep since we know the amplitude and frequency of the modulation signal. Taking a derivative of the entire trace in real time with the oscilloscope gives us positive delta functions for low- to high-amplitude state switches and negative delta functions for high- to low-amplitude switches. The curve shown in the inset to Figure 4.6(c) is a sum of all the delta functions for the intrinsic low- to high-amplitude state transition. This curve,  $h(V)$ , together with our knowledge of the sweep rate,  $dV/dt$ , contains all the necessary information to deduce the transition rate,  $\Gamma$ , assuming that it does not depend on the drive voltage,  $V$ . The probability of

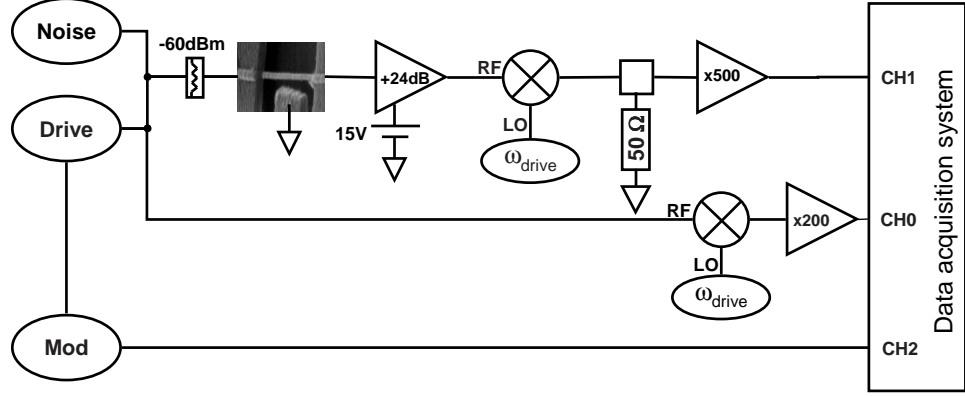


Figure 4.7: Experimental setup to collect the statistics of noise-induced transitions by using amplitude-modulated signal to sweep through both bifurcation points. Using the data acquisition system NI-DAQ 6.9.2 (National Instruments DAQ 6036E) instead of the oscilloscope allows for processing the signal in real time before recording it. The two amplifiers right before the DAQ are isolation amplifiers powered by batteries instead of external voltage.

switching to the other state up to drive value,  $V$ , is

$$P(V) = \int_0^V h(V') dV'. \quad (4.2.5)$$

To find the transition rate from this probability, we can still use the equation (4.2.2), but we need to change the variable of integration from  $t$  to  $V$  [48]:

$$P(V) = 1 - \exp\left(-\int_0^t \Gamma(V) dt'\right) = 1 - \exp\left(-\int_0^V \frac{\Gamma(V)}{dV'/dt} dV'\right) = 1 - \exp\left(-\frac{\Gamma}{f_{AM}} V\right). \quad (4.2.6)$$

Here,  $dV'/dt$  is the drive sweep rate given by the frequency of the modulation signal,  $f_{AM}$ . If we plot  $1 - P(V)$  versus drive,  $V$ , on the log scale, the slope of straight-line fits will be  $-\Gamma/f_{AM}$ . Alternatively, we can take the derivative of  $P(V)$  in both (4.2.5) and (4.2.6) with respect to  $V$  and calculate  $\Gamma$  directly from the histogram  $h(V)$  as

$$\Gamma(V) = \frac{h(V)}{1 - P(V)} f_{AM} = \frac{h(V)}{1 - \int_0^V h(V') dV'} \frac{dV}{dt}. \quad (4.2.7)$$

When the sweep rate is slow, the system is very likely to switch before reaching the bifurcation

point and the histogram will be peaked at some drive,  $V < V_b$ . As the sweep rate is increased, we expect the system to have the most switches closer and closer to the bifurcation point and approach it for fast sweep rates. This saturation with increasing modulation frequency is shown in Figure 4.6(c), where the value of the drive where most transitions occur (peaks of histograms,  $h(V)$ ) is plotted against  $f_{AM}$ . Increasing the sweep rate, therefore, allows us to accurately determine the drive value,  $V_b$ , at the bifurcation point, something we could not easily do for the waiting time experiments.

Differentiating and recording traces with the oscilloscope as shown in Figure 4.6(a) introduces a small distortion to delta function peaks due to the slight curvature of the response curve (Figure 2.1(b)) right before both bifurcation points. The derivative of such a curve is not a perfect delta function as desired, but has an extra lobe on the steeper side, noticeable, for example, in the histogram shown in the inset to Figure 4.6(c). A much better method would be to record the maxima of the derivative peaks for the histogram, but this function cannot be performed by the oscilloscope.

The setup for a better scheme for recording the peaks of the derivatives of a sweep trace is shown in Figure 4.7. Here, the data acquisition board is used instead of an oscilloscope, allowing for real-time unlimited processing of data using the DAQ software.

#### 4.2.4 Noise analysis

The effective noise temperature associated with the intrinsic switching rates, when no extra noise is added to the system, is estimated to be thousands of Kelvin. Since the experiment was conducted in the dipper cooled by liquid helium, the temperature of the sample was 5-15K most of the time so thermal noise cannot be the dominant noise inducing switching between the states. When the temperature is stabilized, thermal noise lies well below any drive circuit noise. Spectral density of displacement noise on resonance for a doubly-clamped nanomechanical resonator with resonant

frequency,  $\omega_0$ , and mass,  $m$ , at temperature,  $T$ , is given by

$$S_x = \frac{4k_B T Q}{m\omega^3}. \quad (4.2.8)$$

In terms of force noise,  $x=QF/k$ ,

$$S_F = \frac{4k_B m\omega_0 T}{Q}. \quad (4.2.9)$$

The driving force in the magnetomotive transduction scheme is the Lorentz force that acts on the nanowire when a current,  $I_d$ , is passed through it in a magnetic field,  $F = LBI_d = LBV/R$ . Thermomechanical noise of a nanomechanical resonator driven and detected magnetomotively can then be expressed in terms of spectral density of voltage noise:

$$S_V = \frac{4k_B m\omega_0 T R^2}{QB^2 L^2}. \quad (4.2.10)$$

For dimensions and parameters of the platinum nanowire given in the previous section, thermomechanical noise of the platinum nanowire resonator at 10 K is calculated to be  $\sqrt{S_V} = 0.89\text{nV}/\sqrt{\text{Hz}}$ . Even a  $50\Omega$  resistor at room temperature on the drive side will dominate the noise that could induce the transitions between the states, since its thermomechanical noise floor is  $\sqrt{4k_B T R} = 1\text{nV}/\sqrt{\text{Hz}}$ .

The measured noise from the function generator HP8648B supplying the drive for the platinum nanowire resonator is about  $1\mu\text{V}/\sqrt{\text{Hz}}$  at the source for the drive values used, which translates to about  $3\text{ nV}/\sqrt{\text{Hz}}$  at the sample after 50.8dBm attenuation in the drive line. This noise is dominant in the magnetomotive scheme and is most likely responsible for the intrinsic switching between two stable states in studied platinum nanowire and silicon carbide resonators.

Intrinsic transitions induced by thermomechanical noise have not yet been observed in nanomechanical resonators, but it should be straightforward to do using a room-temperature driving and detection technique, such as thermoelastic driving coupled with piezoresistive detection.

### 4.3 Ideas for future experiments

This section presents some ideas for applications that can be developed on the basis of the studies presented above. Understanding nonlinear dynamics paves the road to using nanoresonators in the bistable regime as bifurcation amplifiers, as well as offers a sensitive way to detect the transition to quantum regime using noise properties of nonlinear NEMS resonators. Mapping of the basins of attraction can be extended to coupled resonators in an effort to broaden our knowledge of nonlinear dynamics of interacting systems.

#### 4.3.1 Bifurcation amplifier

A bifurcation amplifier is based on the switching of a driven nonlinear resonator between two stable states. If a nanomechanical Duffing resonator is driven at a fixed frequency,  $\sigma_d$ , in the nonlinear regime, the probability of switching depends on the the amplitude of the drive (refer to Figure 4.1(b)). The drive magnitude determines the shape of the response curve: larger drive results in a larger hysteresis and a larger distance between two states. While keeping the frequency of the drive constant, we can change the drive amplitude in such a way that the system goes from the response curve where only low-amplitude branch is available to it at the operating frequency, to the response curve where only high-amplitude branch is available to it. As we change the drive amplitude,  $V_f/V_c$ , the fixed point and the separatrix delineating the basins of attraction are modified as shown in Figure 4.2. If a small incoming signal periodically modulates the drive amplitude moving the fixed points back and forth, the nonlinear resonator will respond with a periodic signal whose peak-to-peak amplitude is equal to the distance between low-amplitude and high-amplitude branches. This scheme constitutes a bifurcation amplifier. Analogously, it can be implemented for a fixed drive amplitude and an incoming signal modulating the operating frequency (refer to Figure 2.1(b)).

As mentioned earlier, a bifurcation amplifier has been implemented in a Josephson junction to perform a non-dissipative, low-back-action measurement of the phase across the junction [102, 101]. In this case, the incoming phase signal was modulating the critical current across the nonlinear Josephson junction, but the dynamics of the amplification process were identical to what I described

above.

It is important to note that the gain of such an amplifier is binary and limited by the distance between low- and high-response amplitudes of the nonlinear resonator in the bistable regime, which is a few nanometers at best in nanomechanical resonators. It is probably impractical to use this amplifier only for the gain. In the context of quantum-limited detection, however, we can hope to benefit from the non-dissipative, low-back-action nature of the amplification exploited in the Josephson junction amplifier and use it to perform a similar sensitive measurement of the state of a quantum mechanical resonator.

Another complication is the intrinsic noise-induced transitions that occur in the bistable regime close to bifurcation points. The small signal to be amplified has to be larger than the portion of the hysteresis region susceptible to these noise transitions. For very small signals, amplification will not be reliable.

### 4.3.2 Basins of attraction of coupled resonators

While dynamics of a single Duffing-type nonlinear resonator are fairly well understood, dynamics of two or more coupled resonators can be much more complex and have not been explored in detail. We can either study several coupled single-degree-of-freedom resonators fabricated together or two (or more) degrees of freedom in a single resonator (e.g., its in-plane and out-of-plane modes or multiple flexural modes as discussed in the next chapter). The advantage of fabricating two (or more) resonators separately is the freedom to design the coupling between them.

An example response for a two-degrees-of-freedom Duffing resonator system found in literature [115, 68] is shown in Figure 5.6, and the bifurcation diagrams were shown to get very convoluted as the driving force increases. It would be interesting to map out the basins of attractions of coupled NEMS and explore changes in the basin boundaries as the coupling between resonators is increased. These studies would fill in the gap in the literature concerning basin of attraction dynamics in interacting systems and once again show usefulness of nanomechanical resonators for fundamental studies of nonlinear dynamics.

### 4.3.3 Noise-induced transitions in a quantum nonlinear resonator

When a nanoresonator is cooled to mK temperature in an effort to see quantum effects [72], quantum fluctuations become the dominant source of noise. The spectral density of the displacement noise is no longer given by equation (2.3.11), but by [50]

$$S_x = 2\hbar\omega_0 \coth\left(\frac{\hbar\omega_0}{2k_B T}\right) \frac{Q}{m\omega_0^3}. \quad (4.3.1)$$

In a comment on our dynamic range paper [92], Stampfer et al. pointed out that the floor for the dynamic range of nanomechanical resonators under 100nm in length at 100mK is set by quantum fluctuations, rather than thermal noise [106]. If such resonator is driven into nonlinear regime [62] (which is possible, say, for a 1 $\mu$ m long nanotube, 10nm in diameter with a resonance frequency of about 1GHz) and we find a way to isolate the device from the instrument noise, the dominant noise that would induce transitions between two stable states is due to quantum fluctuations. Moreover, the transitions in such system will happen via quantum tunneling, rather than thermal escape.

In order to demonstrate this effect experimentally, measurements of noise-induced transitions in the bistable state of the resonator can be carried out as described in the previous section. The critical exponent,  $\delta$ , that describes the dependence of the effective barrier height on the proximity to the bifurcation point, is the parameter of interest. For classical systems, where the mechanism of escape for a metastable state is thermal,  $\delta = 3/2$  almost universally. For quantum systems, where the mechanism of escape is quantum tunneling and quantum fluctuations set the noise floor, the critical exponent,  $\delta$ , has been calculated to be 5/4 for systems with no damping [19, 20] and 1 for systems with high damping [76]. Therefore, by extracting the critical exponent from the noise-induced transition rates, it is possible to determine the classical or quantum nature of the transitions in a nanomechanical resonator.

## Chapter 5

# Making Versatile Devices using Nonlinear NEMS

The real and legitimate goal of the sciences is the endowment of human life with new inventions and riches.

---

FRANCIS BACON

Understanding the dynamics of NEMS resonators opens up possibilities for better devices for sensor applications. For example, by operating the resonator at the onset of nonlinearity close to the infinite negative slope,  $da/d\omega$ , at  $a_c$  in Figure 2.4, the charge sensitivity can be increased drastically, as suggested by Krömmmer et al. [70]. It is also possible to use a nonlinear resonator as the frequency stabilizing element in a feedback loop: the long term phase stability of an oscillator can be improved considerably with this technique [49]. This chapter describes several other effects in NEMS that promise to enhance versatility, performance, and sensitivity of NEMS sensors. They include resonant frequency tuning, dynamic range enhancement, orthogonal mode coupling, and operation of NEMS in higher vibrational modes. I present both experimental and theoretical investigations of these effects. Ideas for future experiments based on the completed work conclude the chapter.

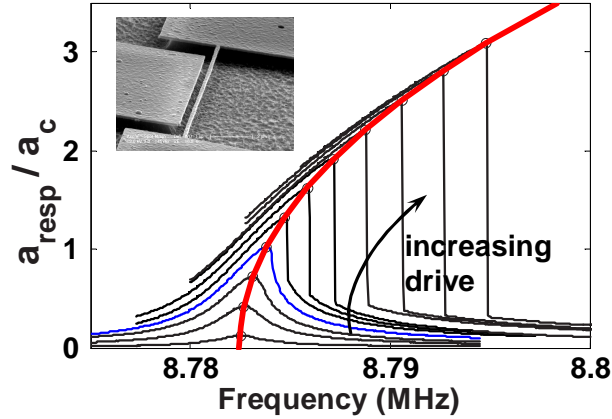


Figure 5.1: Family of resonant response curves of the suspended SiC doubly-clamped beam to a progressively increased drive. Solid red line shows a backbone curve used to characterize the onset of nonlinearity:  $f_{peak} = f_0 (1 + 1/\sqrt{3}Q(a_{peak}/a_c)^2)$ . SEM image of the device is shown in the inset.

## 5.1 Tuning frequency, nonlinearity, and dynamic range<sup>1</sup>

Sensing, imaging, and detection applications of NEMS require a large dynamic range, over which the device responds linearly to the stimulus, as well as operation at desired and, preferably, adjustable frequencies. However, we have shown [92] that as nanomechanical beam resonators become smaller, their dynamic range decreases, making them less useful as linear sensors. The ability to tune nonlinearity, and consequently dynamic range, allows us to overcome this limitation, which can be especially pronounced in NEMS based upon high aspect ratio structures such as nanotubes and nanowires. In addition, a controllable method of tuning provides a way to adjust resonant frequency both for control applications such as phase locking, as well as to null inevitable, fabrication-induced device variations.

In this section we demonstrate an electrostatic mechanism for tuning the nonlinearity in nanomechanical resonators. As a direct consequence, it becomes possible to increase their dynamic range. In addition, we demonstrate an ability to tune the resonant frequency of resonators both upward and downward and evaluate the electromechanical dissipation associated with different regimes of frequency tuning. The results are described by a model that qualitatively agrees with the experiment and can serve as a simple guide for design of tunable nanomechanical devices.

<sup>1</sup>The work in this section has been done with the help of Henk Postma and Igor Bargatin, and published in Applied Physics Letters [66].

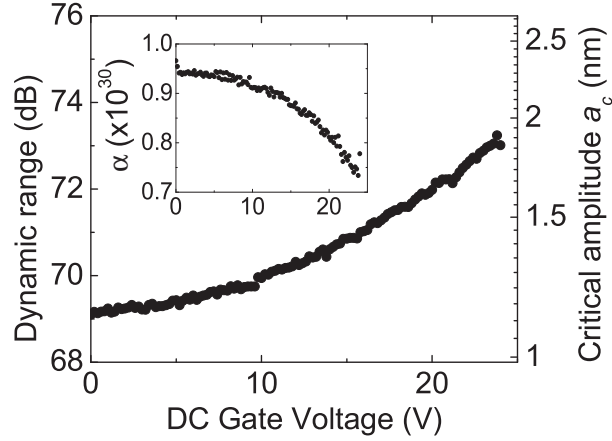


Figure 5.2: Variation of dynamic range and critical amplitude with the gate voltage. The inset shows the observed decrease in effective nonlinearity,  $\alpha$ , with the gate voltage.

The inset to Figure 5.1 shows the device used for the tuning measurements: a suspended metalized SiC beam [117] 150nm wide, 100nm thick, and  $15\mu\text{m}$  long is positioned 400nm away from a gate electrode, to which a DC bias can be applied. Built-in strain in the multilayered structure yields an intrinsic tension within the beam, raising the resonant frequency from the calculated 4.7MHz to the observed 8.78MHz. From the model below, we calculate this residual tension to be  $5.3\mu\text{N}$ . The mechanical resonant characteristics of the beam were measured using the magnetomotive driving and detection technique [25] in a 7T magnetic field. The beam’s resonant frequency was measured to be 8.78MHz for the in-plane mode and 7.60MHz for the out-of-plane mode.

Figure 5.1 shows a typical resonant response of the beam, where the vibration is in the plane of the gate and the gate is grounded. As the drive amplitude is increased, the response becomes nonlinear. In such doubly-clamped beams, the origin of nonlinearity is the additional tension that appears when the beam vibrates with sufficiently large amplitude. The nonlinearity can be characterized by the critical response amplitude,  $a_c$ , the point where the resonance curve develops infinite slope (onset of hysteresis) [85, 92]. We determine  $a_c$  from the “backbone” curve (shown as solid red line in Fig (5.1)) connecting peaks of resonant curves for different drives when the frequency is swept upward.

The electrostatic tuning setup, shown in the inset of Figure 5.1, allows us to tune both nonlinearity and the resonant frequency of the beam. Figure 5.2 shows that critical amplitude increases with DC gate bias. In other words, as the gate voltage is increased, the onset of nonlinearity occurs

at higher drives. This translates into a less nonlinear behavior and, consequently, into the increase in the dynamic range of the device. Figure 5.2 shows the dynamic range growth with the gate voltage, calculated from the measured critical amplitude values and the experimental noise floor of  $1\text{nV}/\sqrt{\text{Hz}}$ . In general, the ultimate noise floor limit is set by thermomechanical noise and quantum fluctuations.

The physical reason for the observed nonlinearity tuning is the appearance of even-order nonlinear terms in the equation of motion. The effective nonlinearity of the system is  $\alpha = \alpha_3 - (10/9\omega_0)\alpha_2^2$ , where  $\alpha_3$  and  $\alpha_2$  are cubic and quadratic nonlinear coefficients, respectively [85]. The cubic nonlinearity is primarily due to the elastic properties of the beam. The quadratic nonlinearity arises when the symmetry of the beam's displacement from its central axis is broken by the capacitive attraction to the gate. DC bias voltage on the gate increases quadratic nonlinearity in the beam, which decreases the overall nonlinearity and results in larger values for the critical amplitude. The observed decrease in the effective nonlinearity,  $\alpha$ , with the DC gate voltage is shown in the inset to Figure 5.2. The possibility of such a nonlinearity tuning mechanism has been suggested by Younis and Nayfeh [118], but we are not aware of any experimental realization of nonlinearity tuning in nanomechanical resonators.

Using the same setup, we can also tune the resonant frequency of the beam. Figure 5.3 illustrates the results obtained by varying the DC bias applied to the gate electrode. When the out-of-plane mode of vibration is excited, we observe an increase in the resonant frequency of the beam with gate voltage (Figure 5.3(a,b)). As the applied gate voltage pulls the beam toward the gate, the resonant frequency increases in a manner similar to the increase in pitch produced by stretching a guitar string. Since the quality factor remains constant throughout the increase in the DC gate voltage (inset of Figure 5.3(b)), this mechanism is well-suited for applications where a change in frequency is the only desired effect.

For the in-plane mode, we observe the decrease in the resonant frequency (Figure 5.3(c,d)). The beam is electrostatically attracted to the gate and this makes its spring constant smaller. This tuning is accompanied by increased dissipation (inset of Figure 5.3(d)) as the modulated capacitance

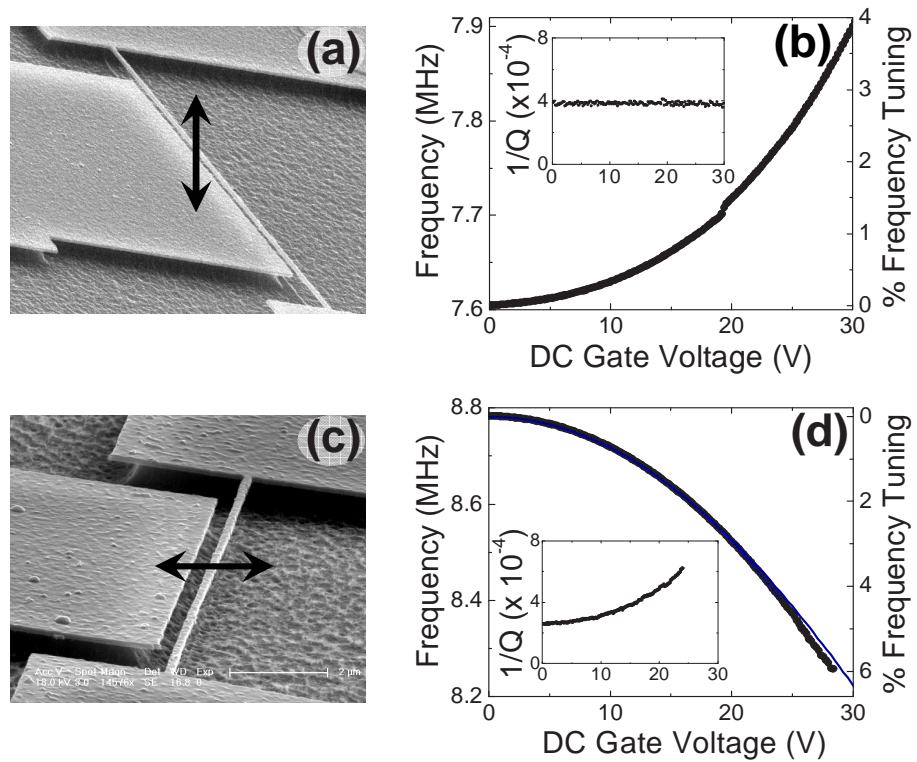


Figure 5.3: Elastic tuning of frequency upward (b) for the beam's vibration out of plane with the gate (a). Capacitive tuning of frequency downward (d) for vibration in plane of the gate (c). The blue curve in (d) is the prediction of the theoretical model for the capacitive frequency tuning.

between the beam and the gate gives rise to dissipative current flow.

Various reversible frequency-tuning mechanisms have been explored in the past. These include STM-aided resonator length adjustment [121], stiffness variation with thermal stress [109], and electrostatic tuning [100, 99]. The frequency has been observed to tune either up [99] or down [100], and the theoretical models built to explain the data took into account a single tuning mechanism, either elastic or capacitive, that seemed dominant in that particular experiment.

In our experiment, we observe both softening and hardening types of frequency tuning in the same device. Here we present a model that reconciles the existence of these two types as it takes into account elastic and capacitive frequency tuning, as well as the beam nonlinearity. The model reliably predicts the decrease in nonlinearity and increase in dynamic range, as well as the two frequency tuning mechanisms that we observe.

Our device is a thin beam that is displaced by DC bias voltage on the gate and driven by small AC voltage. We can write the beam's total displacement,  $u(x, t)$ , as a sum of a static DC displacement,  $z_s(x)$ , and a time-varying AC displacement,  $z(x, t)$ :  $u(x, t) = z_s(x) + z(x, t)$ .

The combination of the electrostatic force, attracting the beam towards the gate, and the elastic restoring force, trying to pull the beam back to its undeformed state, gives us the equation of motion for the beam:

$$EIu_{xxxx} - [T_0 + T(u_x)]u_{xx} + \rho S u_{tt} = \frac{1}{2}c_z[u(x, t)]V^2, \quad (5.1.1)$$

with the boundary condition at the two clamped ends.  $S$  is the beam's cross-sectional area,  $E$  is the Young's modulus,  $\rho$  is the beam density, and  $I$  is the moment of inertia about the longitudinal axis of the beam. The total tension term in brackets is a sum of residual tension,  $T_0$ , and bending-induced tension,  $T(u_x) = (ES/2L) \int_0^L u_x^2 dx$ , where  $L$  is the beam length. The capacitance per unit length,  $c[u(x, t)]$ , is calculated using an approximation of an infinite wire near the semi-infinite plane of the gate [10]:

$$c[u(x, t)] = \frac{2\pi\epsilon\epsilon_0}{\ln \left[ \frac{R+r-u(x, t) + \sqrt{(R+r-u(x, t))^2 - r^2}}{r} \right]} \quad (5.1.2)$$

Because the capacitance per unit length,  $c[u(x, t)]$ , is a nonlinear function of displacement,  $u(x, t)$ ,

it will contribute additional nonlinearities to the resonator dynamics. In order to keep the second and third-order nonlinearities from the capacitive coupling to the gate, we expand  $c[u(x, t)]$  to the fourth order in  $u(x, t)/R$ . The capacitance expansion coefficients,  $K_i$ , are given by the geometry of the system and the DC displacement of the beam.

To find the frequency and nonlinear coefficients in the equation for the time-varying displacement, we approximate the beam shape as  $z(x, t) = z_1(t)\sqrt{2/3}[1 - \cos(2\pi x/L)]$  [92, 38]. A similar expansion of static deflection,  $z_s(x, t) = A_{DC}\sqrt{2/3}[1 - \cos(2\pi x/L)]$ , is used in the static equilibrium equation to solve for the static deflection amplitude,  $A_{DC}$ . The Galerkin discretization procedure [85] gives the time-variant part of the equation of motion:

$$\ddot{z}_1(t) + \omega_0^2 z_1(t) + \alpha_2 z_1^2(t) + \alpha_3 z_1^3(t) = 0, \quad (5.1.3)$$

where

$$\begin{aligned} \omega_0^2 &= \left[ \frac{EI}{3\rho S} + \frac{EA_{DC}^2}{6\rho} \right] \left( \frac{2\pi}{L} \right)^4 + \frac{T_0}{3\rho S} \left( \frac{2\pi}{L} \right)^2 - \frac{K_2 V^2}{\rho S} \\ \alpha_3 &= \frac{E}{18\rho} \left( \frac{2\pi}{L} \right)^4 - \frac{35}{9} \frac{K_4 V^2}{\rho S} \\ \alpha_2 &= \frac{EA_{DC}}{6\rho} \left( \frac{2\pi}{L} \right)^4 - \frac{5}{2} \sqrt{\frac{2}{3}} \frac{K_3 V^2}{\rho S}. \end{aligned} \quad (5.1.4)$$

The resulting equation of motion (5.1.3) is solved numerically (see Appendix B for the Mathematica script that implements the solution) and predicts the observed tuning behavior. The overall nonlinearity is reduced because the quadratic nonlinearity (5.1.4) grows with static DC deflection due to the voltage applied to the gate, and partially cancels out the cubic nonlinearity:  $\alpha = \alpha_3 - 10/(9\omega_0)\alpha_2^2$  [85]. The decrease in  $\alpha_3$  itself with the increased DC voltage is a higher-order effect and is negligible compared to the increase in  $\alpha_2$ .

Compared to the experimental data, the model predicts a sharper increase in  $a_c$  at higher DC voltages (see the last graph in Appendix B). In the experiment, the increase in critical amplitude is probably limited by higher-order and non-tension nonlinearities, e.g., material and inertial nonlinearities [29], that become significant when the induced quadratic nonlinearity cancels the cubic

nonlinearity.

The different frequency tuning behaviors are also explained by equation (5.1.4). The frequency increases in the out-of-plane vibration mode because increasing the gate voltage only stretches the beam (increasing static displacement  $A_{DC}$ ), but does not interact with it electrostatically. For the in-plane vibration mode, there is both stretching (increase in  $A_{DC}$ ) and electrostatic interaction (described by the  $K_2V^2$  term). Electrostatic attraction to the gate has a softening effect on the beam for low gate voltages before the hardening due to stretching overcomes it. If the mass loading by a metal layer on the SiC beam is taken into account, the theoretical expression for resonant frequency (5.1.4) can be fit to the data with excellent agreement as shown in Figure 5.3(d).

The ultimate limit to electrostatic tuning in these devices depends on the pull-in voltage when the beam gets close enough to the gate to irreversibly snap in [17]. The pull-in voltages for the geometry that we describe here were observed to range from 29V to 42V.

A device that has an additional gate electrode below or above the beam should allow tuning of frequency both up and down for the same mode of the resonator if the two electrodes can be biased independently. Such a device could also be used to keep the frequency of the beam constant while tuning its dynamic range.

We have experimentally observed electrostatic tuning of the onset of nonlinearity and, consequently, tuning of dynamic range of nanomechanical resonators. We also demonstrated the ability to tune resonant frequencies of our devices upward and downward. These mechanisms and their analysis provided here are helpful for any applications requiring adjustable frequency or dynamic range. Among these are frequency adjustment to overcome fabrication inaccuracy and embedding a tunable NEMS resonator in a feedback loop to allow for real-time frequency stabilization. Nonlinearity tuning will allow applications of small and sensitive devices (such as single-wall nanotubes) as linear sensors. The proposed theoretical model can be used to experiment with different geometries to optimize frequency or nonlinearity tuning, and to increase the pull-in threshold for specific applications.

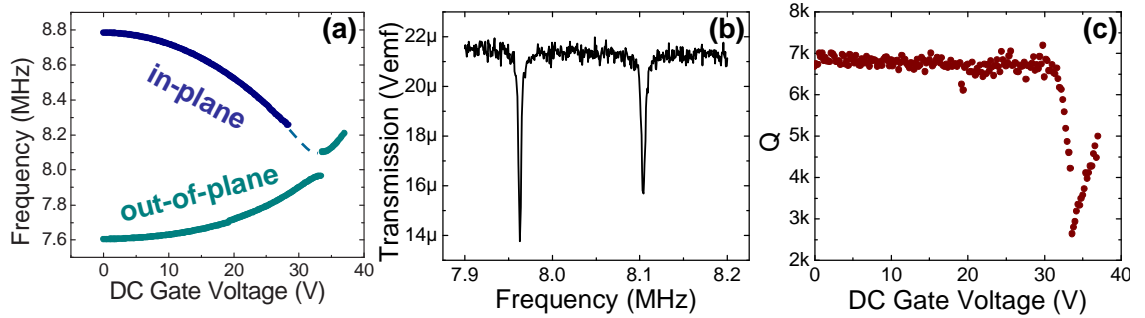


Figure 5.4: Interaction of orthogonal modes in a silicon carbide beam resonator observed magnetotomatively. (a) Frequency tuning of in-plane and out-of-plane modes with DC bias on the gate, resulting in anti-crossing behavior when the interaction is induced at 33.5V. (b) Resonant responses of both modes become visible at 33.5V. (c) The exchange of energy in the interaction induced at 33.5V is seen in the drop of Q for the out-of-plane mode (left branch) and in the growth of Q for the in-plane mode (right branch).

## 5.2 Interaction of orthogonal modes<sup>2</sup>

An interesting application of frequency tuning is the ability to controllably couple the in-plane and out-of-plane modes as the frequencies of the two modes are tuned closer to each other. The mode coupling was observed on two different types of devices and with two different detection techniques.

As described in the previous section, a gate can be used to tune the frequencies of in-plane and out-of-plane modes in different directions (Figure 5.3). In this experiment, temperature of the sample stage was stabilized at 25K, so that the temperature-induced frequency shifts were negligible compared to the effect of DC bias. For a silicon carbide beam 160nm wide and 80nm thick, the resonant frequency of in-plane vibration (8.8MHz) at zero bias is higher than the frequency of out-of-plane vibration (7.6MHz). As we increase the DC bias voltage on the gate positioned 300nm away from the beam, the vibration in the plane of the gate becomes capacitively coupled to the gate and its frequency decreases, whereas the frequency of vibration out of the plane of the gate increases. Finally, the frequencies of the two modes are tuned close enough to each other for the interaction to arise. For the geometry described above, we observed the avoided mode-crossing when the neighboring gate voltage was increased to 33.5V with the frequency gap of 100kHz. The observed coupling is shown in Figure 5.4(a). At this DC bias, both in- and out-of-plane modes are visible at

<sup>2</sup>The SEM detection of coupled modes was performed on devices fabricated by Ronen Almog. The linear coupling mechanism through the supports was suggested by Igor Bargatin.

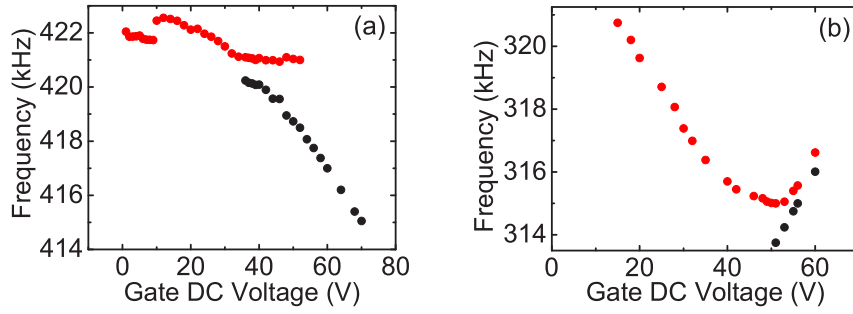


Figure 5.5: Interaction of orthogonal modes in nominally identical gold beam resonators observed in the SEM. (a) A device is driven with 15dBm of power. Mode coupling occurs at 36V with a frequency gap of 860Hz. (b) A different device is driven with 10dBm of power. Mode coupling occurs at 56V with a frequency gap of  $\sim 600$ Hz.

7.964MHz and 8.105MHz respectively (Figure 5.4(b)). The induced interaction is associated with the energy exchange between the two modes: the quality factor of the out-of-plane mode decreases as the quality factor of the in-plane mode starts to grow (Figure 5.4(c)). When the device is tilted  $45^\circ$  in the magnetic field, both modes are visible for all bias voltages and their tuning can be monitored simultaneously.

A similar coupling of in-plane and out-of-plane modes of gold beam resonators has also been observed with the SEM detection technique. Gold beams were fabricated on top of silicon nitride membranes as described in section 3.1.1. Figure 5.5 illustrates mode coupling induced by increased DC voltage on the gate for two nominally identical devices: gold beams 800nm wide, 200nm thick, and  $100\mu\text{m}$  long positioned  $5\mu\text{m}$  away from the gate. The device, whose response is shown in Figure 5.5(a), is driven with 15dBm of power and the mode coupling occurs at about 36V. The gap between two frequencies at this voltage is 860Hz. Figure 5.5(b) shows the response of the other device driven with 10dBm of power with the mode coupling occurring at about 56V. The smallest frequency gap for the avoided crossing is about 600Hz. Judging by the starting resonant frequencies of the in-plane modes, the two devices are under different initial tension calculated to be (a)  $T_0 \approx 13.5\mu\text{N}$  and (b)  $T_0 \approx 7\mu\text{N}$ . With the SEM detection, we cannot measure the starting frequency of the fundamental out-of-plane modes, but using these values of initial tension, we can estimate them to be (a) 390kHz and (b) 290kHz. This situation is the same as for the silicon carbide beams:

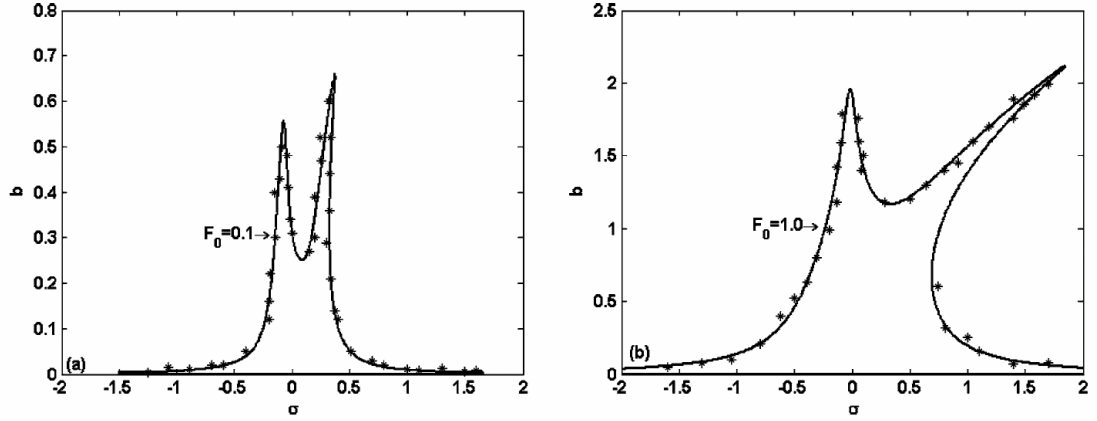


Figure 5.6: Frequency-response curve,  $b(\sigma)$ , of a two-degree-of-freedom Duffing system with internal resonance (from Ref.[115]).

out-of-plane mode frequencies are below the in-plane mode frequencies and are tuned upwards when DC voltage is applied to the gate. The difference in the onset of mode coupling in these two nominally identical devices can be attributed to the variation in geometry and residual tension due to fabrication inaccuracy.

In engineering literature, interaction of modes at commensurate frequencies or multiples of frequency is referred to as "internal resonance" [84]. Figure 5.6, taken from Ref.[115], illustrates a typical response of a two-degree-of-freedom Duffing system with cubic coupled terms when internal resonance is present in the system. If one of the degrees of freedom has a lower onset of nonlinearity than the other one, the dynamics of the system can get complicated (Figure 5.6(b)). For both silicon carbide and gold beams, we observe the coupling of in-plane and out-of-plane fundamental modes, which in this language would be called "one-to-one internal resonance".

We do not understand exactly what physical mechanism is responsible for the coupling of orthogonal modes, and more experiments are needed to clarify the dominant contribution. The anti-crossing behavior points to a dominant linear coupling mechanism. It is likely that the orthogonal modes are coupled linearly through the clamping structures. FEMLAB simulations performed on a slightly asymmetric beam show that the orthogonal modes move away from the out-of-plane and in-plane orientation and become non-planar when the resonant frequencies are very close to each other (about

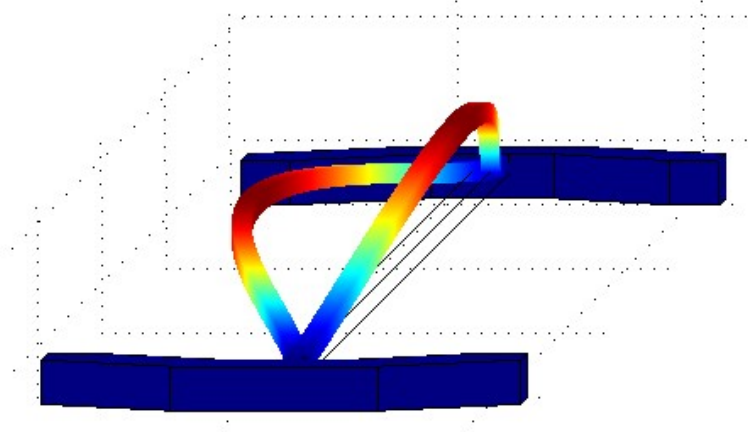


Figure 5.7: Shapes of coupled orthogonal modes when their frequencies are very close (FEMLAB simulation).

1kHz in Figure 5.7). The distortion by the gate and the clamping supports play a significant role in determining the coupling of these modes through their influence on resonant frequency and the overall symmetry of the structure. The anti-crossing gap for such a mechanism would be the measure of asymmetry present in the vibrating beam, and we would expect a perfect frequency match and a crossing behavior for beams that are perfectly symmetric and whose modes would be tilted  $45^\circ$  at the interaction.

Another possible linear coupling mechanism is electrostatic. This mechanism has been studied extensively by Truitt et. al [111], but the authors point out that electrostatic simulations suggest a coupling which would result in a splitting frequency 10 times smaller than what is observed. A clean experimental way to test the presence of electrostatic coupling is to measure the frequency splitting for several devices with varying beam-to-gate gap sizes.

Nonlinear coupling between two modes is also present in the system, but is not likely to be dominant. Two-mode vibration of a doubly-clamped beam is described by the coupled equations of motion for the out-of-plane motion,  $z(x, t)$ , and in-plane motion,  $y(x, t)$ :

$$EI_z z_{xxxx} - Tz_{xx} + \rho S z_{tt} - f(x, t) = 0 \quad (5.2.1)$$

$$EI_y y_{xxxx} - Ty_{xx} + \rho S y_{tt} - f(y, t) = 0. \quad (5.2.2)$$

The nonlinear coupling between the two modes can come in through the additional displacement-dependent tension,  $T(z, t)$ , induced when the beam is vibrating in both y- and z-directions and is stretched from its original length,  $L$ , by the length,  $\Delta L$  [74]:

$$T(x, t) = ES \frac{\Delta L}{L} = \frac{ES}{2L} \int_0^L (z_x(x, t)^2 + y_x(x, t)^2) dx. \quad (5.2.3)$$

This is simply a two-dimensional version of equation (2.3.1). If we include both residual tension,  $T_0$ , and the extra induced tension,  $T = T_0 + \int_0^L (z_x(x, t)^2 + y_x(x, t)^2) dx$ , and apply the Galerkin discretization procedure as discussed in Chapter 2, we find that equations (5.2.1) and (5.2.2) have coupling terms of the form  $z(x, t)y(x, t)^2$  and  $y(x, t)z(x, t)^2$  respectively. Using Galerkin mode shapes,  $\phi_1(x) = \sqrt{2/3}[1 - \cos(2\pi x/L)]$  [38, 112], for both in-plane and out-of-plane modes, we arrive at analytical formulas for the frequencies of two nonlinearly-coupled modes:

$$\omega_z^2 = \left[ \frac{EI_z}{3\rho S} + \frac{Ey_1(t)^2}{18\rho} \right] \left( \frac{2\pi}{L} \right)^4 + \frac{T_0}{3\rho S} \left( \frac{2\pi}{L} \right)^2 \quad (5.2.4)$$

$$\omega_y^2 = \left[ \frac{EI_y}{3\rho S} + \frac{Ez_1(t)^2}{18\rho} \right] \left( \frac{2\pi}{L} \right)^4 + \frac{T_0}{3\rho S} \left( \frac{2\pi}{L} \right)^2. \quad (5.2.5)$$

Dependence of the resonant frequency of one mode on the amplitude of the other mode is the signature of nonlinear coupling. The frequency splitting would in this case depend on the magnitude of the driving force.

If the nature of interaction between in-plane and out-of-plane modes is indeed nonlinear, a nonlinear detection scheme for quantum nanomechanical resonators could be implemented using the energy exchange between two orthogonal modes similar to the theoretical proposal of Santamore et al. [96, 97].

### 5.3 Higher flexural modes of beams<sup>3</sup>

Thermoelastic excitation combined with piezoresistive detection, described in detail in Section 3.2.4, has enabled us to observe resonances of multiple vibrational modes of individual silicon carbide nanomechanical beam resonators, covering a broad frequency range from several MHz to over a GHz. I will show in this section that the dynamic range of higher flexural modes in doubly-clamped piezoresistive beams increases with the mode number.

The schematic of the thermoelastic drive and piezoresistive detection setup is shown in Figure 3.9(b). The devices used for this experiment are bare silicon carbide doubly-clamped beams with metal loops on both ends (Figure 3.9(a)) to implement actuation and detection. The devices varied in length from 4 to 24 $\mu\text{m}$ , and had a width of 400nm and a thickness of 80nm. Two different thin metal film loops were patterned near the two ends of the beam. The 80nm-thick, 100nm-wide loop was patterned from thermally evaporated gold and formed a part of the thermoelastic bilayer actuator (right inset to Figure 3.9(a)). The thinner piezoresistor loop was patterned from a 30nm-thick metal layer created by evaporating a 60%-40% gold-palladium alloy. It consisted of 250nm-long, 50nm-wide legs connected by a larger pad (left inset to Figure 3.9(a)). A 2nm-thick chromium adhesion layer was used in both cases. Typical resistances of metal loops were 30 $\Omega$  for the actuation loop, and 300 $\Omega$  for the detection loop.

Figure 5.8 shows the magnitude of the raw signal from a 16 $\mu\text{m}$ -long beam detected as both the drive and bias voltages are swept over a very wide range of frequencies while keeping the downmixed frequency constant at 95kHz. The large peaks correspond to the first eight out-of-plane flexural modes of the beam. The small peak near the second large peak corresponds to the first in-plane mode. On resonance, both quadratures of the lock-in signal fit the Lorentzian curve shape very well (inset to Figure 5.8) using the procedure described in Section 3.3. The noise floor of  $\approx 3\text{nV}/\text{Hz}^{1/2}$  is largely due to the Johnson noise of the piezoresistor. The small background signal originates from the parasitic coupling between bias, drive, and detection channels and the slight nonlinearity of the

---

<sup>3</sup>This work has been done together with Igor Bargatin. The first part of this section has been accepted for publication in Applied Physics Letters [7].

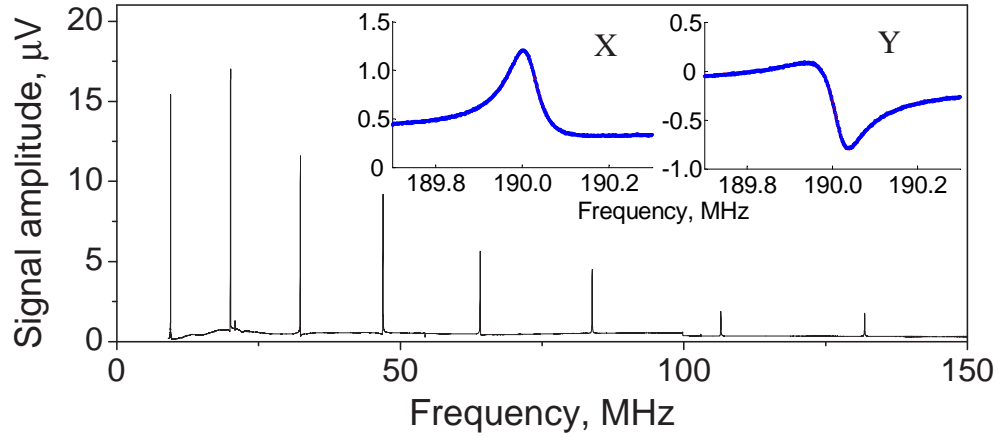


Figure 5.8: Raw signal, referred to the preamplifier input, from a  $16\mu\text{m}$ -long beam. The root-mean-square amplitudes of the drive and bias voltages are  $22\text{mV}$  and  $118\text{mV}$ , respectively. Inset shows both quadratures of the resonant response of the tenth out-of-plane mode (not shown in main panel) and the almost indistinguishable Lorentzian fit to the data.

piezoresistor and preamplifier response.

Table 5.1 lists the frequencies of the first seventeen vibrational modes of the  $16\mu\text{m}$ -long device predicted from FEMLAB finite element simulations, and also shows their measured frequencies and quality factors determined from Lorentzian fits. Discrepancies between predicted and observed frequencies do not exceed a few percent for all modes if the intrinsic strain, which presumably arises during fabrication of multilayer structures, is taken into account. The agreement is excellent for the lower modes and deteriorates slightly only for the highest modes. We attribute this to the difficulty of realistically modeling the imperfect clamping of our beams at their ends. We observe many more resonance peaks above the resonance frequency of the twelfth out-of-plane mode, up to a resonance at  $1.094\text{GHz}$ ; however, these resonance peaks become progressively smaller and some of them overlap, which makes it difficult to identify the nature of the corresponding modes and fit the resonance peaks to Lorentzian curves.

The ability to detect multiple modes of mechanical vibration simultaneously in doubly-clamped beams is important for applications such as mass sensing, where obtaining data from multiple modes can improve the accuracy and speed of measurements [33]. Operation at a higher flexural mode offers the benefits of higher resonance frequency and increased quality factors in air and liquid [8]. The dependence of dynamic range on the mode number has not been investigated so far. I present below

Table 5.1: Predicted,  $f_{pred}$ , and experimental,  $f_{exp}$ , resonance frequencies, as well as quality factors in vacuum,  $Q_{exp}$ , for the lowest twelve out-of-plane (out) modes and lowest five in-plane (in) modes of a  $16\mu\text{m}$ -long beam. In simulations, we assume the following material properties for the SiC layer: Young’s modulus 430GPa, Poisson ratio 0.3, mass density  $3.2\text{g}/\text{cm}^3$  [58], and intrinsic tensile strain  $2.8\times 10^{-4}$ . The strain value was varied to obtain the best fit to the experimental frequencies.

mode	1out	2out	1in	3out	4out	2in	5out	6out	3in	7out	8out	9out	4in	10out	11out	5in	12out
$f_{pred}$ , MHz	9.48	20.0	20.7	32.3	46.9	54.3	64.1	83.8	103	106	131	158	166	187	219	244	252
$f_{exp}$ , MHz	9.52	20.0	20.8	32.3	46.8	54.0	63.9	83.5	103	107	132	160	167	190	223	243	258
$Q_{exp}$	12000	7750	3110	5570	4410	2630	3620	3220	2210	2950	2700	2510	1740	2190	1970	1760	1660

the experimental data on dynamic range of higher flexural modes and a simple theoretical model that attempts to explain the observed effects.

The nonlinearity data was collected from the  $16\mu\text{m}$  device described above using thermoelastic actuation and piezoresistive detection. As mentioned in Section 3.2.4, the amplitude of the downmixed piezoresistive signal is  $V \approx V_b g \langle \varepsilon_{xx} \rangle / 2$ , where  $g$  is the gauge factor. For each mode, we record a family of resonance curves for increasing drive values and a constant bias voltage,  $V_b$ . Since thermoelastic actuation tends to heat the device, frequency shifts down as the drive level is increased:  $f_0 \propto -V^2$ . Using several linear response curves for lower drives, we can calculate the proportionality factor and correct all of the data for the frequency shift. The higher drive response curves are then used to define the backbone curve as described in Section 5.1. The critical voltage,  $V_c$ , corresponding to the onset of nonlinearity is extracted from the shape of the backbone curve.  $V_c$  values for the first ten out-of-plane modes are plotted in Figure 5.9 as black points. These values are proportional to critical strain in the beam multiplied by the gauge factor,  $g$ . The bias voltage,  $V_b$ , was kept the same for all modes, barring some variation in attenuation by the filter at different frequencies. Assuming that the gauge factor is constant for all modes in a single device, the critical strain is observed to increase with the mode number until the eighth flexural mode. In other words, compared to the fundamental mode, the nonlinearity sets in later for higher modes in strain devices and, if we account for the degradation of  $Q$  in higher modes, dynamic range of a device can be increased up to 4dB simply by operating in a higher flexural mode.

We will try to use a simple theoretical model using an adapted Galerkin discretization method described in Chapter 2 to analyze the response of higher flexural modes of the beam. Instead of

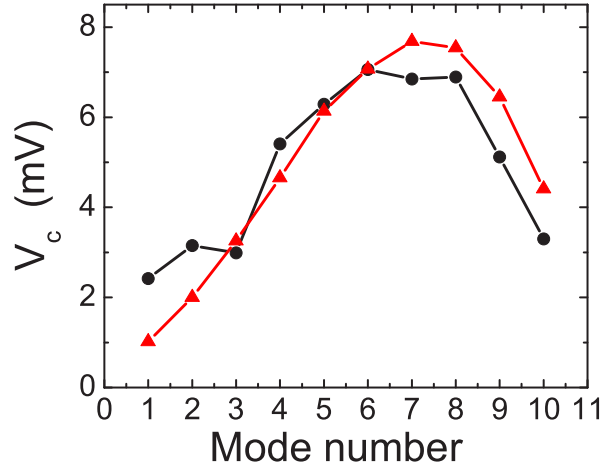


Figure 5.9: Critical strain dependence on the resonator's vibrational mode number. Experimental data (black points) qualitatively agrees with the predictions of theoretical model (red triangles).

approximate Galerkin modes, we will use mode shapes for a doubly-clamped beam under stress and negligible tension as given in equation (2.1.4), where the values of  $\kappa L$  for the first ten modes are

$$\begin{aligned} \kappa L = & (1) 4.73, (2) 7.8532, (3) 10.9956, (4) 14.1372, (5) 17.2788, \\ & (6) 20.4204, (7) 23.5619, (8) 26.7035, (9) 29.8451, (10) 32.9867. \end{aligned}$$

Resonant frequencies,  $\omega_n$ , are given by equation (2.1.15) and the cubic nonlinearity,  $\alpha_n$ , by equation (2.3.7). Using the experimental values of  $Q$  for the first ten modes (see Table 5.1), we can calculate the critical amplitude,  $(a_c)_n$ , as [85]

$$(a_c)_n^2 = \frac{8\sqrt{3}}{9\alpha_n Q_n^{exp}}. \quad (5.3.1)$$

The measured strain in a beam of thickness,  $t$ , can be converted into displacement using equation (3.2.7) for small displacements,  $\varepsilon_{xx} \approx z''(x)t/2$ . If all strain is concentrated at the clamping point, critical strain can be obtained from

$$(\varepsilon_c)_n = \frac{t}{2}(a_c)_n \frac{z_n''(0)}{z_n(L/2n)}. \quad (5.3.2)$$

However, we use loops of finite length (250nm in this experiment) for piezoresistive detection and we detect an average strain distribution over the entire length,  $l$ , of the loop:  $\varepsilon_n^{exp} \approx (\int_0^l z_n''(x)dx)t/(2L)$ . For the higher out-of-plane modes, the strain may change sign within the length of the detection loop, resulting in partial cancellation of the detected strain average. The critical strain determination has to take this into consideration:

$$(\varepsilon_c)_n = \frac{t}{2}(a_c)_n \frac{\int_0^l z_n''(x)dx}{z_n(L/2n)L}. \quad (5.3.3)$$

Moreover, the beam is not clamped rigidly at one point, but is attached to a ledge that forms during dry etching and is about 350nm in the device we used. The ledge is modeled by effectively lengthening the beam by this amount. Calculated critical strain for the first ten modes of the resonator is plotted in Figure 5.9 as red triangles. The theoretical values have been scaled by the maximum experimentally observed critical signal voltage (that of the 6th flexural mode).

While there is good qualitative agreement with the experimental data, theory predicts a much steeper initial increase in the critical strain than is observed experimentally. This discrepancy is most likely due to our choice of mode shapes for the beam. The beam mode shapes given by (2.1.4) do not take into account any residual tension,  $T_0$ , in the beam, which from the fundamental resonance response is determined to be  $T_0 = 3.58\mu\text{N}$ . Presence of residual tension lowers the overall nonlinearity (refer to equation (2.3.14)) and would account for a slower initial growth of critical strain with the mode number that is observed experimentally. This is especially pronounced in the lower modes, where the residual tension has a larger effect. The actual mode shapes are also affected by the exact geometry of clamping structure, which can be taken into account in a finite-element simulation, but not in an analytical model.

In the  $16\mu\text{m}$  long device with 250nm long detection loop, the increase in critical strain levels off at about 7th or 8th out-of-plane mode. This is due to partial cancellation of the detected strain average as the strain changes sign within the length of the detection loop for these higher modes. The cancellation can be engineered to set in for even higher modes by patterning a shorter detection loop and/or increasing the beam length. It is also helpful to minimize the clamping ledge by shortening the dry etch time. The simple theoretical model presented in this section is sufficient for such design.

The increase in dynamic range applies only to the piezoresistive strain signal: the critical amplitude tends to go down as the mode number is increased, whereas the critical strain, which depends on the second derivative of displacement, goes up with mode number. For engineering applications requiring higher dynamic range, piezoresistive strain detection has a clear advantage over magnetomotive or capacitive displacement amplitude detection for NEMS resonators operated in higher flexural modes.

## 5.4 Ideas for future experiments

This section presents some ideas for future experiments that can be done on the basis of the studies presented above. Here I discuss ideas for a self-tuning resonator, cooling of a resonator mode using nonlinear interaction with another mode, and synchronization in coupled oscillators.

### 5.4.1 Self-tuning resonators

A beautiful extension of the demonstrated frequency tuning of the resonator after fabrication would be a demonstration of a self-tuning resonator that is able to adjust its resonant frequency to the drive in a broad frequency range without sacrificing its quality factor.

Self-tuning of the nonlinear systems has been observed before in vibrating soap films, where the liquid film can adapt its mass distribution to the forcing frequency [13], and in vibrating smectic liquid crystal films, where a small metal ball free to move in the plane of the film adjusts its position as a function of excitation frequency [15]. Even more relevant to NEMS has been the experiment with a piano string loaded with a bead which was free to slide [14]. When driven magnetomotively with external frequency in a large frequency band, the bead was observed to move so that the system would be made resonant. The mass and number of beads were found to affect the range of resonant frequencies accessible to the system. These experiments have a common theme: given additional degrees of freedom, a driven nonlinear system will adapt them in such a way that it will become resonant with the drive in a large range of driving frequencies, effectively acquiring a continuous frequency spectrum instead of a discrete one.

In light of these results, a nonlinear nanomechanical resonator could also be made self-tuning by adding some large inert molecules that are free to move on the surface as the device is vibrating. Recently, micro- and nanobeads have been observed to move on cantilevers in microfluidic environment and arrange in clusters according to the shape of the excited mode [34]. It is not clear how the quality factor of such a resonator would vary with frequency, since mode shapes would also depend on a mass distribution that would vary with frequency. Self-tuning resonators would be very useful in large arrays of sensors as the frequency variation due to fabrication will no longer be an issue, and no ad hoc tuning of each element (e.g., by a gate electrode) need to be implemented.

#### 5.4.2 Cooling of a resonator mode by interaction with another mode<sup>4</sup>

Energy exchange between two nonlinearly coupled modes at resonant frequencies  $\omega_1$  and  $\omega_2$ , with high and low Q, can be used to cool or to heat up the mode at  $\omega_1$  if the device is driven at the difference or sum of two frequencies respectively. To implement this experiment, we need the setup to observe a thermal spectrum of two modes with different quality factors. For example, two different out-of-plane modes of a piezoresistively measured silicon carbide beam could be used: we can usually find a mode at  $\omega_1$  with a higher Q and at  $\omega_2$  with a lower Q, and the modes are nonlinearly coupled through the structure of the beam. While observing the thermal spectrum, the device should then be driven at the frequency  $\omega_2 - \omega_1$ . According to Mark Dykman [36], thermal peak at  $\omega_1$  will acquire the distribution of  $\omega_2$ -peak, i.e., effectively cool down since its amplitude will decrease and its quality factor will increase. Alternatively, if the device is driven at frequency  $\omega_1 + \omega_2$ , the  $\omega_1$  will become larger and narrower, i.e., will be effectively amplified. The ability to control the amplitude and Q of a mode of interest using the nonlinear coupling to another mode might prove useful for cooling and quantum measurement applications. Unfortunately, the piezoresistive downmixing detection is currently thermally limited for only the fundamental mode. Careful engineering of devices and optimization of background reduction are needed to be able to detect thermomechanical noise of two different modes in order to perform the suggested experiment.

---

<sup>4</sup>The idea for this experiment was proposed by Mark Dykman.

### 5.4.3 Synchronization of coupled oscillators

Recent progress in building a self-sustaining nanomechanical oscillator, a resonator with the energy supplied to it using a feedback loop with a DC-powered amplifier [46], has set the stage for synchronization experiments in nonlinear nanoscale systems [30]. Self-sustaining oscillators exhibit limit-cycle dynamics in phase space as opposed to simple fixed-point dynamics described in Chapter 4. Depending on the strength of coupling among oscillators, either full frequency and phase, or just phase synchronization can be observed [91]. Arrays of coupled nanomechanical oscillators would not only be useful for studying synchronization phenomena ubiquitous in the natural world [108, 42], but could also offer some ways to improve the device properties for engineering applications, such as better power handling and added immunity from the ambient noise. We can even dream of building up an artificial neural computer using synchronized NEMS elements [52].

Synchronization in the presence of noise is especially interesting to study. On one hand, theoretical models suggest that driving oscillators with the same noise can be enough to induce their synchronization [107, 87]. On the other hand, if noise is intrinsic to each oscillator, the intensity of phase noise (characterized by the square of standard deviation) of an array of  $N$  oscillators can be reduced by a factor of  $N$  over the phase noise of a single resonator by simple averaging. If noise is extrinsic to individual oscillators, i.e., affects them through their interaction with each other or the environment, the reduction can be even better: a factor of  $N^3$  in certain parameter regimes [86].

The best place to start is two NEMS oscillators with tunable (e.g., electrostatic) coupling. For fixed resonator frequencies, we can change the coupling between them and monitor the phases and frequencies of both oscillators for the onset of synchronization. Alternatively, we can leave the coupling fixed and tune the frequency of one of the resonators to look for evidence of locking. Currently the feedback circuit required to make a NEMS self-sustaining oscillator consists of bulky macroscopic instruments. For building functional arrays of NEMS oscillators, we will need to develop nanofabrication techniques for feedback loops and detection multiplexors on chips containing NEMS devices.

## Chapter 6

# Concluding Remarks

Science is what you know, philosophy is  
what you don't know.

---

BERTRAND RUSSELL

While nonlinear systems in physics are usually associated with a lot of pain and massive consumption of computational resources, in biology they are everywhere. In biological systems, nonlinearity does not seem to be an inconvenient quirk of nature that we hope is small, as it forces us to deviate from familiar and manageable linear equations. In biological systems, nonlinearity looks more like an adaptation, a necessary ingredient of making living creatures work as well as they do [28, 37, 45, 59]. All the curious phenomena associated with nonlinear behavior, such as synchronization, self-organization, pattern formation, all seem to contribute to the robust and adapting natural world. Out there, in the real world, nonlinearity is a rule and even a necessity rather than an exception.

I like to think that studying nonlinear physical systems brings us a little closer to understanding the most profound designs of nature, including those of biological systems. Maybe a profound understanding of nonlinear effects and how they modify system behaviors is the only link that is needed to be able to explain biology. The challenges in establishing this link are significant: nonlinearities in most organic systems are not small and only few of them currently allow clear classification by type of bifurcation or nonlinearity. Moreover, real-life organisms are never found in isolation and their nonlinear interactions with the environment greatly complicate their behavior.

We as physicists are trying to explain this complex world by adding small nonlinear perturbations on top of linear mathematical descriptions that have been developed over the last few centuries. But maybe here our approach and our mathematics are not quite right for describing highly nonlinear interacting systems. Maybe we need to change our frame of thinking and come up with essentially nonlinear mathematics, which would have the usual linear equations as a limiting case. Maybe essentially linear variables, such as displacement or velocity, have to be replaced by variables characterizing complex phenomena, such as entropy or deviation from robustness. . .

I am convinced that the convergence of physics, chemistry, and biology, which has become more pronounced in recent years, will bring deeper understanding of the role that nonlinearity plays in nature. And I sincerely hope that the development of nanotechnology will result in new tools to probe and analyze nonlinear effects in both physical and biological systems and will shed some light on the most fascinating mysteries of nature.

# Bibliography

- [1] ADAMS, S. G., BERTSCH, F. M., SHAW, K. A., AND MACDONALD, N. C. Independent tuning of linear and nonlinear stiffness coefficients. *Journal of Microelectromechanical Systems* 7, 2 (1998), 172–180.
- [2] ALDRIDGE, J. S., AND CLELAND, A. N. Noise-enabled precision measurements of a Duffing nanomechanical resonator. *Physical Review Letters* 94, 15 (2005), 156403.
- [3] ANDERSON, T. J., NAYFEH, A. H., AND BALACHANDRAN, B. Experimental verification of the importance of the nonlinear curvature in the response of a cantilever beam. *Journal of Vibration and Acoustics* 118 (1996), 21–27.
- [4] ARMOUR, A. D., BLENCOWE, M. P., AND SCHWAB, K. C. Entanglement and decoherence of a micromechanical resonator via coupling to a cooper-pair box. *Physical Review Letters* 88, 14 (2002), 148301.
- [5] ATLURI, S. Nonlinear vibrations of a hinged beam including nonlinear inertia effects. *Journal of Applied Mechanics* 40 (1973), 121–126.
- [6] BARBIC, M., MOCK, J. J., SMITH, D. R., AND SCHULTZ, S. Single crystal silver nanowires prepared by the metal amplification method. *Journal of Applied Physics* 91, 11 (2002), 9341–9345.
- [7] BARGATIN, I., KOZINSKY, I., AND ROUKES, M. L. Measurement of multiple modes of nanomechanical resonators using electrothermal actuation and piezoresistive detection. *Applied Physics Letters* 90 (2007), 093116.

- [8] BARGATIN, I., KOZINSKY, I., AND ROUKES, M. L. Quality factors of higher flexural modes of nanomechanical resonators. *Manuscript in preparation* (2007).
- [9] BARGATIN, I., MYERS, E. B., ARLETT, J., GUDLEWSKI, B., AND ROUKES, M. L. Sensitive detection of nanomechanical motion using piezoresistive signal downmixing. *Applied Physics Letters* 86, 13 (2005), 133109.
- [10] BLEANEY, B. I., AND BLEANEY, B. *Electricity and Magnetism*, 3rd ed. Oxford University Press, Oxford; New York, 1989.
- [11] BOGOLIUBOV, N. N., AND MITROPOLSKY, Y. A. *Asymptotic Methods in the Theory of Non-linear Oscillations*, 2 ed. Hindustan Publishing Corporation, Delhi, 1961.
- [12] BOLOTIN, V. V. *The Dynamic Stability of Elastic Systems. Holden-Day Series in Mathematical Physics*. Holden-Day, Inc., San Francisco, 1964.
- [13] BOUDAUD, A., COUDER, Y., AND BEN AMAR, M. Self-adaptation in vibrating soap films. *Physical Review Letters* 82, 19 (1999), 3847–3850.
- [14] BOUDAUD, A., COUDER, Y., AND BEN AMAR, M. A self-adaptative oscillator. *The European Physical Journal B* 9, 1 (1999), 159 – 165.
- [15] BRAZOVSKAIA, M., AND PIERANSKI, P. Self-tuning behavior of vibrating smectic films. *Physical Review Letters* 80, 25 (1998), 5595–5598.
- [16] BRUNNER, M., SCHMID, R., SCHMITT, R., STURM, M., AND GESSNER, O. Electron-beam MCM testing and probing. *IEEE Transactions on Components, Packaging, and Manufacturing Technology* 17, 1 (1994), 62–68.
- [17] BUKS, E., AND ROUKES, M. L. Metastability and the Casimir effect in micromechanical systems. *Europhysics Letters* 54, 2 (2001), 220–226.
- [18] BUKS, E., AND YURKE, B. Mass detection with a nonlinear nanomechanical resonator. *Physical Review E* 74, 4 (2006), 046619.

- [19] CALDEIRA, A. O., AND LEGGETT, A. J. Influence of dissipation on quantum tunneling in macroscopic systems. *Physical Review Letters* 46, 4 (1981), 211–214.
- [20] CALDEIRA, A. O., AND LEGGETT, A. J. Quantum tunneling in a dissipative system. *Annals of Physics* 149 (1983), 374–456.
- [21] CARR, D. W., EVOY, S., SEKARIC, L., CRAIGHEAD, H. G., AND PARPIA, J. M. Measurement of mechanical resonance and losses in nanometer scale silicon wires. *Applied Physics Letters* 75, 7 (1999), 920–922.
- [22] CHAN, H. B., AND STAMBAUGH, C. Activation barrier scaling and crossover for noise-induced switching in a micromechanical parametric oscillator. *cond-mat/0609394* (2006).
- [23] CHO, A. Researchers race to put the quantum into mechanics. *Science* 299, 5603 (2003), 36–37.
- [24] CLELAND, A. N., AND ROUKES, M. L. Fabrication of high frequency nanometer scale mechanical resonators from bulk Si crystals. *Applied Physics Letters* 69, 18 (1996), 2653–2655.
- [25] CLELAND, A. N., AND ROUKES, M. L. A nanometre-scale mechanical electrometer. *Nature* 392, 6672 (1998), 160–162.
- [26] CLELAND, A. N., AND ROUKES, M. L. External control of dissipation in a nanometer-scale radiofrequency mechanical resonator. *Sensors and Actuators A* 72, 3 (1999), 256–261.
- [27] CLELAND, A. N., AND ROUKES, M. L. Noise processes in nanomechanical resonators. *Journal of Applied Physics* 92, 5 (2002), 2758–2769.
- [28] COLLINS, J. J., IMHOFF, T. T., AND GRIGG, P. Noise-mediated enhancements and decrements in human tactile sensation. *Physical Review E* 56, 1 (1997), 923–926.
- [29] CRESPO DA SILVA, M. R. M., AND GLYNN, C. C. Nonlinear flexural-flexural-torsional dynamics of inextensional beams. *Journal of Structural Mechanics* 6 (1978), 437–461.

- [30] CROSS, M. C., ZUMDIECK, A., LIFSHITZ, R., AND ROGERS, J. L. Synchronization by nonlinear frequency pulling. *Physical Review Letters* 93, 22 (2004), 224101.
- [31] CUSUMANO, J. P., AND KIMBLE, B. W. A stochastic interrogation method for experimental measurements of global dynamics and basin evolution: application to a two-well oscillator. *Nonlinear Dynamics* 8 (1995), 213–235.
- [32] DEQUESNES, M., ROTKIN, S. V., AND ALURU, N. R. Calculation of pull-in voltages for carbon-nanotube-based nanoelectromechanical switches. *Nanotechnology* 13 (2002), 120–131.
- [33] DOHN, S., SANDBERG, R., SVENDSEN, W., AND BOISEN, A. Enhanced functionality of cantilever based mass sensors using higher modes. *Applied Physics Letters* 86, 23 (2005), 233501.
- [34] DORRESTIJN, M., BIETSCH, A., ACIKALIN, T., RAMAN, A., HEGNER, M., MEYER, E., AND GERBER, C. Chladni figures revisited based on nanomechanics. *Physical Review Letters* 98, 2 (2007), 026102.
- [35] DYKMAN, M. I., AND KRIVOGLAZ, M. A. Theory of fluctuational transitions between stable states of a nonlinear oscillator. *Soviet Physics JETP* 50, 1 (1979), 30–37.
- [36] DYKMAN, M. I., AND KRIVOGLAZ, M. A. Theory of nonlinear oscillator interacting with a medium. In *Soviet Physics Reviews*, I. M. Khalatnikov, Ed., vol. 5. Harwood Academic, New York, 1984, pp. 265–441.
- [37] EGUILUZ, V. M., OSPECK, M., CHOE, Y., HUDSPETH, A. J., AND MAGNASCO, M. O. Essential nonlinearities in hearing. *Physical Review Letters* 84, 22 (2000), 5232–5235.
- [38] EISLEY, J. G. Nonlinear vibration of beams and rectangular plates. *Journal of Applied Mathematics and Physics* 15, 9 (1964), 167–175.
- [39] EKINCI, K. L., HUANG, X. M. H., AND ROUKES, M. L. Ultrasensitive nanoelectromechanical mass detection. *Applied Physics Letters* 84, 22 (2004), 4469–4471.

- [40] EKINCI, K. L., YANG, Y. T., HUANG, X. M. H., AND ROUKES, M. L. Balanced electronic detection of displacement in nanoelectromechanical systems. *Applied Physics Letters* 81, 12 (2002), 2253–2255.
- [41] EMAM, S. A. *A Theoretical and Experimental Study of Nonlinear Dynamics of Buckled Beams*. PhD thesis, 2002.
- [42] ENRIGHT, J. T. Temporal precision in circadian systems: A reliable neuronal clock from unreliable components? *Science* 209, 4464 (1980), 1542–1545.
- [43] EVAN-IWANOWSKI, R. M. *Resonance Oscillations in Mechanical Systems*. Elsevier Scientific, New York, 1976.
- [44] EVERHART, T. E., AND THORNLEY, R. F. M. Wide-band detector for micro-microampere low-energy electron currents. *Journal of Scientific Instruments* 37, 7 (1960), 246.
- [45] FEE, M. S., SHRAIMAN, B., PESARAN, B., AND MITRA, P. P. The role of nonlinear dynamics of the syrinx in the vocalizations of a songbird. *Nature* 395 (1998), 67–71.
- [46] FENG, X. L., WHITE, C. J., HAJIMIRI, A., AND ROUKES, M. L. Ultra-high frequency low-noise self-sustaining oscillator with vibrating nanodevice. *To be submitted* (2007).
- [47] FUJIOKA, H., NAKAMAE, K., HIROTA, M., URA, K., AND TAKASHIMA, S. A real-time electron beam testing system. *Journal of Physics E* 22 (1989), 138–143.
- [48] GARG, A. Escape-field distribution for escape from a metastable potential well subject to a steadily increasing bias field. *Physical Review B* 51, 21 (1995), 15592–15595.
- [49] GREYWALL, D. S., B., Y., BUSCH, P. A., PARGELLIS, A. N., AND WILLETT, R. L. Evading amplifier noise in nonlinear oscillators. *Physical Review Letters* 72, 19 (1994), 2992–2995.
- [50] HANGGI, P., AND INGOLD, G.-L. Fundamental aspects of quantum Brownian motion. *Chaos* 15, 2 (2005), 026105.

- [51] HARDY, W. R., BEHERA, S. K., AND CAVAN, D. A voltage contrast detector for the SEM. *Journal of Physics E* 8, 9 (1975), 789.
- [52] HOPPENSTEADT, F. C., AND IZHIKEVICH, E. M. Synchronization of MEMS resonators and mechanical neurocomputing. *IEEE Transactions on Circuits and Systems - I: Fundamental Theory and Applications* 48, 2 (2001), 133–138.
- [53] HUANG, X. M. H., FENG, X. L., ZORMAN, C. A., MEHREGANY, M., AND ROUKES, M. L. VHF, UHF and microwave frequency nanomechanical resonators. *New Journal of Physics* 7 (2005), 247–261.
- [54] HUANG, X. M. H., PRAKASH, M. K., ZORMAN, C. A., MEHREGANY, M., AND ROUKES, M. L. Free-free beam silicon carbide nanomechanical resonators. In *The 12th International Conference on Solid State Sensors, Actuators, and Microsystems* (Boston, MA, 2003).
- [55] HUANG, X. M. H., ZORMAN, C. A., MEHREGANY, M., AND ROUKES, M. L. Nanoelectromechanical systems: Nanodevice motion at microwave frequencies. *Nature* 421, 6922 (2003), 496.
- [56] HUSAIN, A., HONE, J., POSTMA, H. W. C., HUANG, X. M. H., DRAKE, T., BARBIC, M., SCHERER, A., AND ROUKES, M. L. Nanowire-based very-high-frequency electromechanical resonator. *Applied Physics Letters* 83, 6 (2003), 1240–1242.
- [57] JACKSON, K. M., DUNNING, J., ZORMAN, C. A., AND SHARPE, W. N. Mechanical properties of epitaxial 3C silicon carbide thin films. *Journal of Microelectromechanical Systems* 14, 4 (2005), 664–673.
- [58] JIANG, L., CHEUNG, R., HEDLEY, J., HASSAN, M., HARRIS, A. J., BURDESS, J. S., MEHREGANY, M., AND ZORMAN, C. A. SiC cantilever resonators with electrothermal actuation. *Sensors and Actuators A* 128, 2 (2006), 376–386.

- [59] JINDRICH, D. L., ZHOU, Y., BECKER, T., AND DENNERLEIN, J. T. Non-linear viscoelastic models predict fingertip pulp force-displacement characteristics during voluntary tapping. *Journal of Biomechanics* 36 (2003), 497–503.
- [60] KAAJAKARI, V., MATTILA, T., KIIHAMAKI, J., KATTELUS, H., OJA, A., AND SEPPA, H. Nonlinearities in single-crystal silicon micromechanical resonators. In *The 12th International Conference on Solid State Sensors, Actuators, and Microsystems* (Boston, MA, 2003).
- [61] KAAJAKARI, V., MATTILA, T., OJA, A., AND SEPPA, H. Nonlinear limits for single-crystal silicon microresonators. *Journal of Microelectromechanical Systems* 13, 5 (2004), 715–724.
- [62] KATZ, I., RETZKER, A., STRAUB, R., AND LIFSHITZ, R. Classical to quantum transition of a driven nonlinear nanomechanical resonator. *To be submitted* (2007).
- [63] KNOBEL, R. G., AND CLELAND, A. N. Nanometre-scale displacement sensing using a single electron transistor. *Nature* 424, 6946 (2003), 291–293.
- [64] KOGAN, O. Controlling transitions in a Duffing oscillator by sweeping parameters in time. *nlin/0607023* (2006).
- [65] KOGAN, O., AND DYKMAN, M. I. Critical exponents away from bifurcation point in Duffing systems. *Manuscript in preparation* (2007).
- [66] KOZINSKY, I., POSTMA, H. W. C., BARGATIN, I., AND ROUKES, M. L. Tuning nonlinearity, dynamic range, and frequency of nanomechanical resonators. *Applied Physics Letters* 88, 25 (2006), 253101.
- [67] KOZINSKY, I., POSTMA, H. W. C., KOGAN, O., HUSAIN, A., AND ROUKES, M. L. Basins of attraction of a nonlinear platinum nanowire mechanical resonator. *To be submitted* (2007).
- [68] KOZLOWSKI, J., PARLITZ, U., AND LAUTERBORN, W. Bifurcation analysis of two coupled periodically driven Duffing oscillators. *Physical Review E* 51, 3 (1995), 1861–1867.
- [69] KRAMERS, H. A. Brownian motion in a field of force and the diffusion model of chemical reactions. *Physica* 7, 4 (1940), 284–304.

- [70] KROMMER, H., ERBE, A., TILKE, A., MANUS, S., AND BLICK, R. H. Nanomechanical resonators operating as charge detectors in the nonlinear regime. *Europhysics Letters* 50, 1 (2000), 101–6.
- [71] KURKIJARVI, J. Intrinsic fluctuations in a superconducting ring closed with a Josephson junction. *Physical Review B* 6, 3 (1972), 832–835.
- [72] LAHAYE, M. D., BUU, O., CAMAROTA, B., AND SCHWAB, K. C. Approaching the quantum limit of a nanomechanical resonator. *Science* 304, 5667 (2004), 74–77.
- [73] LANDAU, L. D., AND LIFSHITZ, E. M. *Mechanics*, 3rd ed., vol. 1 of *Course of Theoretical Physics*. Butterworth Heinemann, Oxford, 1981.
- [74] LANDAU, L. D., AND LIFSHITZ, E. M. *Theory of Elasticity*, 3rd ed., vol. 7 of *Course of Theoretical Physics*. Butterworth Heinemann, Oxford, Boston, 1986.
- [75] LAPIDUS, L. J., ENZER, D., AND GABRIELSE, G. Stochastic phase switching of a parametrically driven electron in a Penning trap. *Physical Review Letters* 83, 5 (1999), 899–902.
- [76] LARKIN, A. I., AND OVCHINNIKOV, Y. N. Quantum-mechanical tunneling with dissipation. The pre-exponential factor. *Soviet Physics JETP* 59, 2 (1984), 420–424.
- [77] LEAMY, M. J., AND GOTTLIEB, O. Nonlinear dynamics of a taut string with material nonlinearities. *Journal of Vibration and Acoustics* 123 (2001), 53–60.
- [78] LEE, S. I., HOWELL, S. W., RAMAN, A., AND REIFENBERGER, R. Nonlinear dynamics of microcantilevers in tapping mode atomic force microscopy: A comparison between theory and experiment. *Physical Review B* 66, 11 (2002), 115409.
- [79] LI, M., TANG, H. X., AND ROUKES, M. L. Ultra-sensitive NEMS-based cantilevers for sensing, scanned probe and very high-frequency applications. *Nature Nanotechnology* 2 (2007), 114–120.

- [80] LIFSHITZ, R., AND CROSS, M. C. Response of parametrically driven nonlinear coupled oscillators with application to micromechanical and nanomechanical resonator arrays. *Physical Review B* 67, 13 (2003), 134302.
- [81] LIFSHITZ, R., AND ROUKES, M. L. Thermoelastic damping in micro- and nanomechanical systems. *Physical Review B* 61, 8 (2000), 5600–5609.
- [82] MARTIN, C. R. Nanomaterials: A membrane-based synthetic approach. *Science* 266, 5193 (1994), 1961–1966.
- [83] MOHANTY, P., HARRINGTON, D. A., EKINCI, K. L., YANG, Y. T., MURPHY, M. J., AND ROUKES, M. L. Intrinsic dissipation in high-frequency micromechanical resonators. *Physical Review B* 66, 8 (2002), 085416.
- [84] NAYFEH, A. H. *Nonlinear Interactions: Analytical, Computational, and Experimental Methods*. *Wiley Series in Nonlinear Science*. John Wiley & Sons, Inc., New York, 2000.
- [85] NAYFEH, A. H., AND MOOK, D. T. *Nonlinear Oscillations*, 1st ed. *Physics and Applied Mathematics: A Wiley-Interscience Series of Texts, Monographs & Tracts*. John Wiley & Sons, New York, 1979.
- [86] NEEDLEMAN, D. J., TIESINGA, P., AND SEJNOWSKI, T. Collective enhancement of precision in networks of coupled oscillators. *Physica D* 155, 3-4 (2001), 324–336.
- [87] NEIMAN, A., SCHIMANSKY-GEIER, L., CORNELL-BELL, A., AND MOSS, F. Noise-enhanced phase synchronization in excitable media. *Physical Review Letters* 83, 23 (1999), 4896–4899.
- [88] NGUYEN, C.-C. Frequency-selective MEMS for miniaturized low-power communication devices. *IEEE Transactions on Microwave Theory and Techniques* 47, 8 (1999), 1486–1503.
- [89] PAI, P. F., AND NAYFEH, A. H. Non-linear non-planar oscillations of a cantilever beam under lateral base excitations. *International Journal of Non-Linear Mechanics* 25, 5 (1990), 455–474.

- [90] PAMIDIGHANTAM, S., PUERS, R., BAERT, K., AND TILMANS, H. A. C. Pull-in voltage analysis of electrostatically actuated beam structures with fixed-fixed and fixed-free end conditions. *Journal of Micromechanics and Microengineering* 12, 4 (2002), 458.
- [91] PIKOVSKY, A. S., ROSENBLUM, M. G., AND KURTHS, J. *Synchronization: A Universal Concept in Nonlinear Science*, 1st ed. Cambridge University Press, Cambridge, 2002.
- [92] POSTMA, H. W. C., KOZINSKY, I., HUSAIN, A., AND ROUKES, M. L. Dynamic range of nanotube- and nanowire-based electromechanical systems. *Applied Physics Letters* 86, 22 (2005), 223105.
- [93] REIMER, L. *Scanning Electron Microscopy*, vol. 45 of *Springer Series in Optical Sciences*. Springer-Verlag, Berlin, 1985.
- [94] ROY, R., SHORT, R., DURIN, J., AND MANDEL, L. First-passage-time distributions under the influence of quantum fluctuations in a laser. *Physical Review Letters* 45, 18 (1980), 1486–1490.
- [95] RUGAR, D., BUDAKIAN, R., MAMIN, H. J., AND CHUI, B. W. Single spin detection by magnetic resonance force microscopy. *Nature* 430 (2004), 329–332.
- [96] SANTAMORE, D. H., DOHERTY, A. C., AND CROSS, M. C. Quantum nondemolition measurement of Fock states of mesoscopic mechanical oscillators. *Physical Review B* 70, 14 (2004), 144301.
- [97] SANTAMORE, D. H., GOAN, H.-S., MILBURN, G. J., AND ROUKES, M. L. Anharmonic effects on a phonon-number measurement of a quantum-mesoscopic-mechanical oscillator. *Physical Review A* 70, 5 (2004), 052105.
- [98] SAPMAZ, S., BLANTER, Y. M., GUREVICH, L., AND ZANT, H. S. J. v. D. Carbon nanotubes as nanoelectromechanical systems. *Physical Review B* 67, 23 (2003), 235414.
- [99] SAZONOVA, V., YAISH, Y., UESTUENEL, H., ROUNDY, D., ARIAS, T. A., AND MCEUEN, P. L. A tunable carbon nanotube electromechanical oscillator. *Nature* 431 (2004), 284–287.

- [100] SCHWAB, K. Spring constant and damping constant tuning of nanomechanical resonators using a single-electron transistor. *Applied Physics Letters* 80, 7 (2002), 1276–1278.
- [101] SIDDIQI, I., VIJAY, R., PIERRE, F., WILSON, C. M., FRUNZIO, L., METCALFE, M., RIGETTI, C., SCHOELKOPF, R. J., DEVORET, M. H., VION, D., AND ESTEVE, D. Direct observation of dynamical bifurcation between two driven oscillation states of a Josephson junction. *Physical Review Letters* 94, 2 (2005), 027005.
- [102] SIDDIQI, I., VIJAY, R., PIERRE, F., WILSON, C. M., METCALFE, M., RIGETTI, C., FRUNZIO, L., AND DEVORET, M. H. RF-driven Josephson bifurcation amplifier for quantum measurement. *Physical Review Letters* 93, 20 (2004), 207002.
- [103] SIDLES, J. A., GARBINI, J. L., BRULAND, K. J., RUGAR, D., ZUEGER, O., HOEN, S., AND YANNONI, C. S. Magnetic resonance force microscopy. *Reviews of Modern Physics* 67, 1 (1995), 249–265.
- [104] SIM, K. S., AND WHITE, J. D. New technique for in-situ measurement of backscattered and secondary electron yields for the calculation of signal-to-noise ratio in a SEM. *Journal of Microscopy* 217, 3 (2005), 235–240.
- [105] STAMBAUGH, C., AND CHAN, H. B. Noise-activated switching in a driven nonlinear micromechanical oscillator. *Physical Review B* 73, 17 (2006), 172302.
- [106] STAMPFER, C., ROTTER, S., AND BURGDORFER, J. Comment on “Dynamic range of nanotube- and nanowire-based electromechanical systems” [Appl. Phys. Lett. 86, 223105 (2005)]. *Applied Physics Letters* 88, 3 (2006), 036101.
- [107] STRATONOVICH, R. *Topics in the Theory of Random Noise (Mathematics and Its Applications)*, 1st ed. Gordon and Breach Science Publishers Ltd., London, 1967.
- [108] STROGARTZ, S. H. *Sync: The Emerging Science of Spontaneous Order*, 1st ed. Hyperion, New York, 2003.

- [109] SYMS, R. R. A. Electrothermal frequency tuning of folded and coupled vibrating micromechanical resonators. *Journal of Microelectromechanical Systems* 7, 2 (1998), 164–171.
- [110] TABADDOR, M. Influence of nonlinear boundary conditions on the single-mode response of a cantilever beam. *International Journal of Solids and Structures* 37 (2000), 4915–4931.
- [111] TRUITT, P. A., HERTZBERG, J., ALTUNKAYA, E., AND SCHWAB, K. C. Coupling of transverse modes of a nanomechanical resonator. *Manuscript in preparation* (2006).
- [112] TSENG, W.-Y., AND DUGUNDJI, J. Nonlinear vibrations of a beam under harmonic excitation. *Journal of Applied Mechanics* 37 (1970), 292–297.
- [113] TURNER, K. L., MILLER, S. A., HARTWELL, P. G., MACDONALD, N. C., STROGARTZ, S. H., AND ADAMS, S. G. Five parametric resonances in a microelectromechanical system. *Nature* 396, 6707 (1998), 149–152.
- [114] VIRGIN, L. N., TODD, M. D., BEGLEY, C. J., TRICKEY, S. T., AND DOWELL, E. H. Basins of attraction in experimental nonlinear oscillators. *International Journal of Bifurcation and Chaos* 8, 3 (1998), 521–533.
- [115] WEI, K., RUIHONG, L., AND SHUANG, L. Resonance and bifurcation in a nonlinear Duffing system with cubic coupled terms. *Nonlinear Dynamics* 46 (2006), 211–221.
- [116] YANG, Y. T., CALLEGARI, C., FENG, X. L., EKINCI, K. L., AND ROUKES, M. L. Zeptogram-scale nanomechanical mass sensing. *Nano Letters* 6, 4 (2006), 583–586.
- [117] YANG, Y. T., EKINCI, K. L., HUANG, X. M. H., SCHIAVONE, L. M., ROUKES, M. L., ZORMAN, C. A., AND MEHREGANY, M. Monocrystalline silicon carbide nanoelectromechanical systems. *Applied Physics Letters* 78, 2 (2001), 162–164.
- [118] YOUNIS, M. I., AND NAYFEH, A. H. A study of the nonlinear response of a resonant microbeam to an electric actuation. *Nonlinear Dynamics* 31, 1 (2003), 91–117.

- [119] YU, M. F., WAGNER, G. J., RUOFF, R. S., AND DYER, M. J. Realization of parametric resonances in a nanowire mechanical system with nanomanipulation inside a scanning electron microscope. *Physical Review B* 66, 7 (2002), 073406(1–4).
- [120] YURKE, B., GREYWALL, D. S., PARGELLIS, A. N., AND BUSCH, P. A. Theory of amplifier-noise evasion in an oscillator employing a nonlinear resonator. *Physical Review A* 51, 5 (1995), 4211–4229.
- [121] ZALALUTDINOV, M., ILIC, B., CZAPLEWSKI, D., ZEHNDER, A., CRAIGHEAD, H. G., AND PARPIA, J. M. Frequency-tunable micromechanical oscillator. *Applied Physics Letters* 77, 20 (2000), 3287–3289.
- [122] ZHAO, J. H., BRIDGES, G. E., AND THOMSON, D. J. Direct evidence of “spring softening” nonlinearity in micromachined mechanical resonator using optical beam deflection technique. *Journal of Vacuum Science and Technology A* 24, 3 (2006), 732–736.

## Appendix A

# Duffing equation analysis using Landau and Lifshitz method

The discussion in this section follows the Landau and Lifshitz approach to the analysis of the anharmonic oscillations [73] filling in some details of the calculations. We will start by considering an anharmonic oscillator in one dimension, expanding its Lagrangian up to the third-order nonlinear term to describe its motion:

$$L = \frac{1}{2}m\dot{x}^2 - \frac{1}{2}m\omega_0^2x^2 - \frac{1}{3}m\alpha x^3 - \frac{1}{4}m\beta x^4. \quad (\text{A.0.1})$$

The equation of motion corresponding to this Lagrangian is

$$\ddot{x} + \omega_0^2x = -\alpha x^2 - \beta x^3. \quad (\text{A.0.2})$$

We will look for the solution as a series of approximations:

$$\begin{aligned} x &= x^{(1)} + x^{(2)} + x^{(3)}, \text{ where} \\ x^{(1)} &= a \cos(\omega t), \text{ with } \omega = \omega_0 + \omega^{(1)} + \omega^{(2)} + \omega^{(3)}. \end{aligned}$$

To find the differential equation satisfied by  $x^{(2)}$ , substitute  $x = x^{(1)} + x^{(2)}$  and  $\omega = \omega_0 + \omega^{(1)}$  into the equation of motion:

$$\frac{\omega_0^2}{\omega^2}\ddot{x} + \omega_0^2x = -\alpha x^2 - \beta x^3 - \left(1 - \frac{\omega_0^2}{\omega^2}\right)\ddot{x}. \quad (\text{A.0.3})$$

We get

$$\begin{aligned}
& -a\omega_0 \cos(\omega t) + \frac{\omega_0^2}{\omega^2} \ddot{x}^{(2)} + a\omega_0 \cos(\omega t) + \omega_0^2 x^{(2)} = \\
& -\alpha a^2 \cos^2(\omega t) - 2a\alpha x^{(2)} \cos(\omega t) - \alpha(x^{(2)})^2 - \beta a^3 \cos^3(\omega t) - 3\beta a^2 x^{(2)} \cos^2(\omega t) - \\
& -3\beta a(x^{(2)})^2 \cos(\omega t) - \beta(x^{(2)})^3 + \left(1 - \frac{\omega_0^2}{\omega^2}\right) a\omega^2 \cos(\omega t) - \left(1 - \frac{\omega_0^2}{\omega^2}\right) \ddot{x}^{(2)}.
\end{aligned}$$

Neglecting the small third and higher order terms, we are left with

$$\begin{aligned}
\ddot{x}^{(2)} + \omega_0^2 x^{(2)} &= -\alpha a^2 \cos^2(\omega t) + \left(1 - \frac{\omega_0^2}{\omega^2}\right) \ddot{x}^{(2)} \text{ or, expanding to the second order,} \\
\ddot{x}^{(2)} + \omega_0^2 x^{(2)} &= -\frac{1}{2}\alpha a^2 - \frac{1}{2}\alpha a^2 \cos(2\omega t) + 2\omega_0 \omega^{(1)} a \cos(\omega t).
\end{aligned}$$

We would like to account for all the resonance (i.e.,  $\cos(\omega t)$ ) terms in  $x^{(1)}$ , so that the higher-order contributions to  $x$  are small. Therefore, in the second order term,  $x^{(2)}$ , we want the resonance term to be absent, and the condition for this is to set  $\omega^{(1)} = 0$ . To find  $x^{(2)}$ , then, we just need to solve the differential equation:

$$\ddot{x}^{(2)} + \omega_0^2 x^{(2)} = -\frac{1}{2}\alpha a^2 - \frac{1}{2}\alpha a^2 \cos(2\omega t). \quad (\text{A.0.4})$$

The solution to the homogeneous equation,  $\ddot{x}^{(2)} + \omega_0^2 x^{(2)} = 0$ , is  $x_h^{(2)} = A \cos(\omega t) + B \sin(\omega t)$ . Trying the particular solution,  $x_p^{(2)} = C + D \cos(2\omega t)$ , and plugging it into the original equation, we find that  $C = -\frac{\alpha a^2}{2\omega_0^2}$  and  $D = \frac{\alpha a^2}{2(4\omega^2 - \omega_0^2)} = \frac{\alpha a^2}{6\omega_0^2}$  because  $\omega^{(1)} = 0$  as agreed above. Therefore, we get that

$$x^{(2)} = -\frac{\alpha a^2}{2\omega_0^2} + \frac{\alpha a^2}{6\omega_0^2} \cos(2\omega t). \quad (\text{A.0.5})$$

To get an approximation to a higher order, put  $x = x^{(1)} + x^{(2)} + x^{(3)}$  and  $\omega = \omega_0 + \omega^{(2)}$  in the original equation of motion. After neglecting the higher order terms, we end up with

$$\ddot{x}^{(3)} + \omega_0^2 x^{(3)} = a^3 \left( \frac{1}{4} - \frac{\alpha^2}{6\omega_0^2} \right) \cos(3\omega t) + a \left( 2\omega_0 \omega^{(2)} + \frac{5a^2 \alpha^2}{6\omega_0^2} - \frac{3}{4} a^2 \beta \right) \cos(\omega t). \quad (\text{A.0.6})$$

Again assuming we can absorb the resonance term into  $x^{(1)}$ , the equation for  $x^{(3)}$  becomes

$$\ddot{x}^{(3)} + \omega_0^2 x^{(3)} = a^3 \left( \frac{1}{4} - \frac{\alpha^2}{6\omega_0^2} \right) \cos(3\omega t). \quad (\text{A.0.7})$$

The coefficient of  $\cos(\omega t)$  here is set to 0 – this allows us to solve for  $\omega^{(2)}$ :

$$\begin{aligned} a \left( 2\omega_0 \omega^{(2)} + \frac{5a^2 \alpha^2}{6\omega_0^2} - \frac{3}{4} a^2 \beta \right) &= 0 \implies \\ \omega^{(2)} &= \frac{1}{2\omega_0} \left( \frac{3}{4} a^2 \beta - \frac{5a^2 \alpha^2}{6\omega_0^2} \right) = \frac{3a^2 \beta}{8\omega_0} - \frac{5a^2 \alpha^2}{6\omega_0^3}. \end{aligned}$$

Trying a particular solution,  $x^{(3)} = A \cos(3\omega t)$ ,

$$\begin{aligned} -9\omega^2 A \cos(3\omega t) + A\omega_0^2 \cos(3\omega t) &= a^3 \left( \frac{1}{4} - \frac{\alpha^2}{6\omega_0^2} \right) \cos(3\omega t) \implies \\ A &= \frac{a^3}{\omega_0^2 - 9\omega^2} \left( \frac{1}{4} - \frac{\alpha^2}{6\omega_0^2} \right) \approx \frac{a^3 \omega_0^4 (2\alpha^2 - 3\omega_0^2 \beta)}{3\omega_0^4 (32\omega_0^4 + 27a^2 \omega_0^2 \beta)} = \frac{a^3 \alpha^2}{48\omega_0^4} - \frac{a^3 \beta}{32\omega_0^2}. \end{aligned}$$

Then the third order correction is

$$x^{(3)} = \left( \frac{a^3 \alpha^2}{48\omega_0^4} - \frac{a^3 \beta}{32\omega_0^2} \right) \cos(3\omega t). \quad (\text{A.0.8})$$

Now, we will consider the case of the driven oscillator corresponding to the equation of motion

$$\ddot{x} + 2\lambda \dot{x} + \omega_0^2 x + \beta x^3 = D \cos(\gamma t). \quad (\text{A.0.9})$$

For the driving frequency,  $\gamma$ , to be near resonance, we write  $\gamma = \omega_0 + \epsilon$ , where  $\epsilon$  is small. We have already shown that if the nonlinear term is absent, the amplitude is

$$b = \frac{D}{2\omega_0 \sqrt{\epsilon^2 + \lambda^2}}. \quad (\text{A.0.10})$$

The addition of anharmonicity to oscillations results in the dependence of  $\omega$  on  $b^2$  as we have just seen from the calculation of the second-order correction to  $\omega$ . Thus, our new  $\omega$  for the nonlinear

case can be written as

$$\omega = \omega_0 + \omega^{(2)} = \omega_0 + \left( \frac{3\beta}{8\omega_0} - \frac{5\alpha^2}{6\omega_0^3} \right) b^2 = \omega_0 + \kappa b^2, \quad (\text{A.0.11})$$

where  $\kappa = \frac{3\beta}{8\omega_0} - \frac{5\alpha^2}{6\omega_0^3}$ . Since  $\gamma = \omega_0 + \epsilon$  stays the same as for the linear case, the equivalent procedure is to re-define  $\epsilon$  to be  $\epsilon - \kappa b^2$ . This is the  $\epsilon$  we now need to substitute into our earlier relation for the amplitude in order to account for the nonlinear term. The new equation connecting  $b$  and  $\epsilon$  is

$$b = \frac{D}{2\omega_0\sqrt{\epsilon^2 + \lambda^2}}. \quad (\text{A.0.12})$$

This gives an equation that is third order in the amplitude,  $b^2$ :

$$\kappa^2 b^6 - 2\epsilon\kappa b^4 + (\epsilon^2 + \lambda^2)b^2 = \frac{D^2}{4\omega_0^2}, \quad (\text{A.0.13})$$

that can be solved with the help of *Mathematica* in order to obtain the plot of  $b$  vs.  $\epsilon$ . The example plots determined by the solution are shown in Figure A.1. It has been shown above and in literature [11] that the second root, which is clearly visible between the other two in the bottom left graph in Figure A.1, corresponds to the unstable oscillations of the system.

The analytical expression describing the resonance curve allows us to determine the driving force for which the nonlinear effects become significant, i.e., the resonance curve leans over to the right. Let  $D_c$  be the critical value of driving force,  $D$ , that corresponds to the transition at which the tangent to the peak point is vertical. That is, at the critical point  $\frac{db}{d\epsilon} \rightarrow \infty$ . Differentiating the above equation with respect to  $\epsilon$ , we get

$$\frac{db}{d\epsilon} = \frac{\kappa b^3 - \epsilon b}{\epsilon^2 - 4\epsilon\kappa b^2 + 3\kappa^2 b^4 + \lambda^2} \rightarrow \infty. \quad (\text{A.0.14})$$

This means that

$$\epsilon^2 - 4\epsilon\kappa b^2 + 3\kappa^2 b^4 + \lambda^2 = 0. \quad (\text{A.0.15})$$

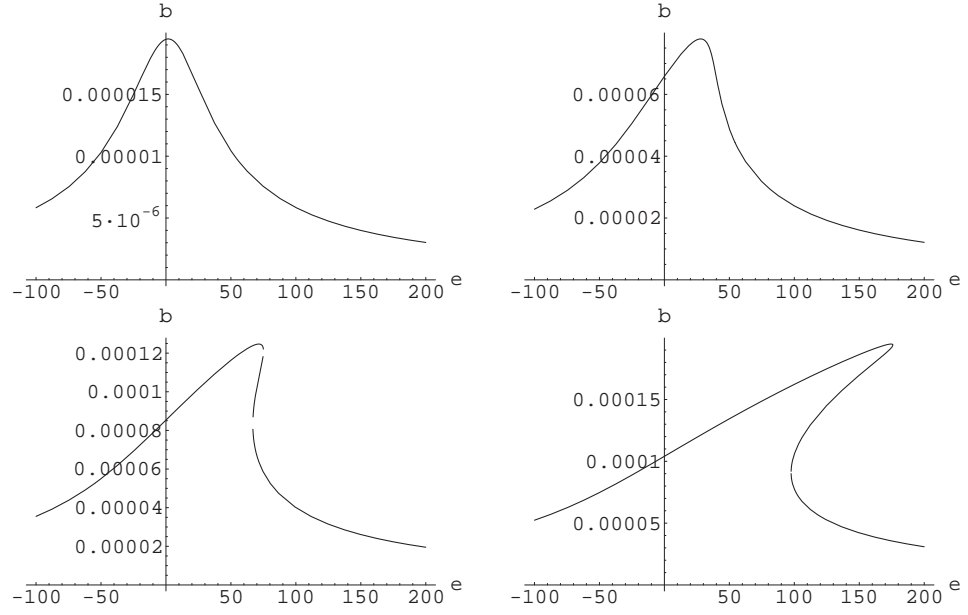


Figure A.1: Example resonance curves for the fixed  $\beta$  and increasing driving force illustrating the gradual change in shape.

This is a quadratic equation with the discriminant

$$\mathcal{D} = 4\kappa^2 b^4 \epsilon^2 - 3\kappa^2 b^4 \epsilon^2 - 3\kappa^2 b^4 \lambda^2. \quad (\text{A.0.16})$$

Setting it equal to 0 to get the inflection point, we obtain the condition on  $\epsilon$  and the corresponding condition on  $b$ :  $\epsilon^2 = 3\lambda^2$  and  $\kappa b^2 = \frac{2}{3}\epsilon$ . Substituting these values back into the original equation and solving for  $D$  allows us to obtain the critical value for the driving force:

$$D_c^2 = \frac{32\sqrt{3}}{9\kappa} \omega_0^2 \lambda^3. \quad (\text{A.0.17})$$

The results obtained by the Landau and Lifshitz method are equivalent to the results obtained by the method of multiple scales.

## Appendix B

# Mathematica script for solving the nonlinear equation with electrostatics

This is the listing of the Mathematica script to solve the frequency and nonlinearity tuning model described in Chapter 5.

### Loading experimental data

```
Clear[bb10]

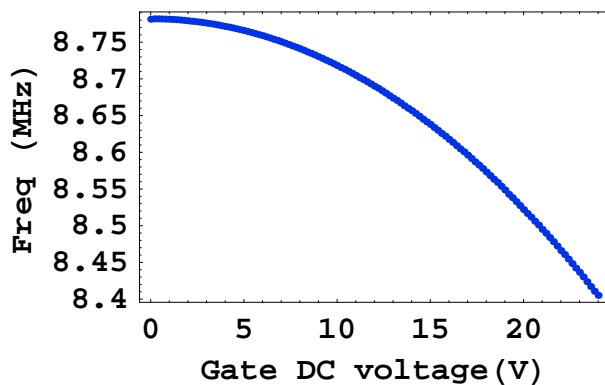
$TextStyle = {FontWeight->"Bold", Font->"Arial", FontSize -> 12};

bb10 = Transpose[Import["H:/Data/011605/A13.2_bb9_fullbg4.dat"]];

Fexp = bb10[[2]] / 106 ;

f0vsVgate = Transpose [Union [{bb10[[1]]}, {bb10[[2]] / 106 }]] ;

f0graph = ListPlot[f0vsVgate, PlotStyle -> {RGBColor[0, .2, .9], PointSize[0.015]}, Frame -> True,
Axes -> None, FrameLabel -> {"Gate DC voltage(V)", "Freq (MHz)"}, ImageSize -> Automatic]
```



```
Qexp = bb10[[3]];
```

```
Q = First[Qexp]
```

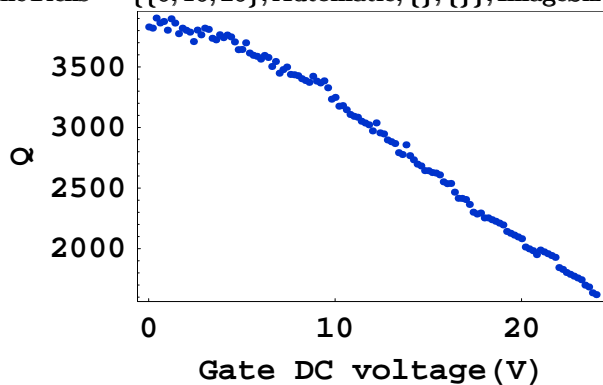
```
3829.89
```

```
QvsVgate = Transpose[Union[{bb10[[1]]}, {bb10[[3]]}]];
```

```
Qgraph = ListPlot[QvsVgate, PlotStyle → {RGBColor[0, 0.2, 0.8], PointSize[0.015]}, Frame → True,
```

```
Axes → None, FrameLabel → {"Gate DC voltage(V)", "Q"},
```

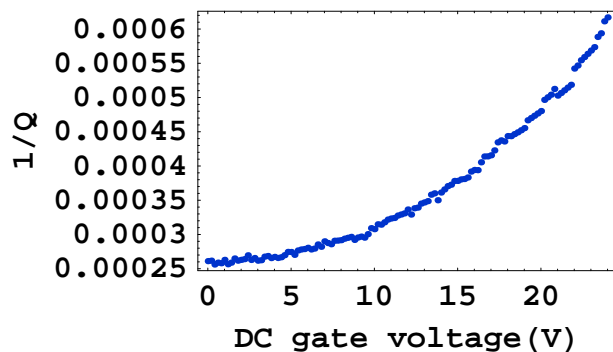
```
FrameTicks → {{0, 10, 20}, Automatic, {}, {}}, ImageSize → Automatic]
```



```
QinvvsVgate = Transpose[Union[{bb10[[1]]}, {1/(bb10[[3]])}]];
```

```
Qinvgraph = ListPlot[QinvvsVgate, PlotStyle → {RGBColor[0, 0.2, 0.8], PointSize[0.015]},
```

```
Frame → True, Axes → None, FrameLabel → {"DC gate voltage(V)", "1/Q"}, ImageSize → Automatic]
```

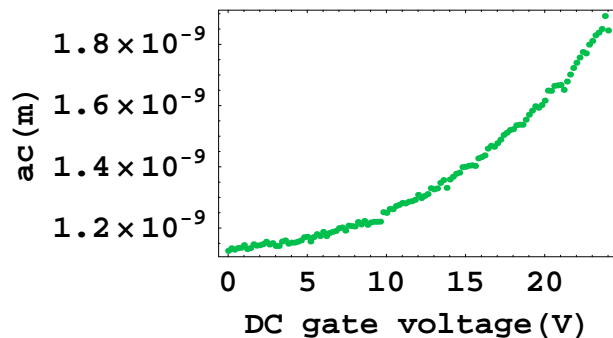


```
Npts = First[Dimensions[Qexp]];
```

```
acvsVgate = Transpose[Union[{bb10[[1]]}, {bb10[[4]]}]];
```

```
acgraph = ListPlot[acvsVgate, PlotStyle → {RGBColor[0, 0.75, .3], PointSize[0.015]},
```

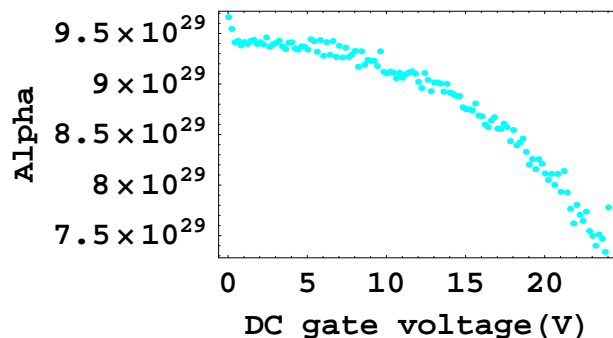
```
Frame → True, Axes → None, FrameLabel → {"DC gate voltage(V)", "ac(m)"}, ImageSize → Automatic]
```



```
alphavsVgate = Transpose[Union[{bb10[[1]]}, {bb10[[6]]}]];
```

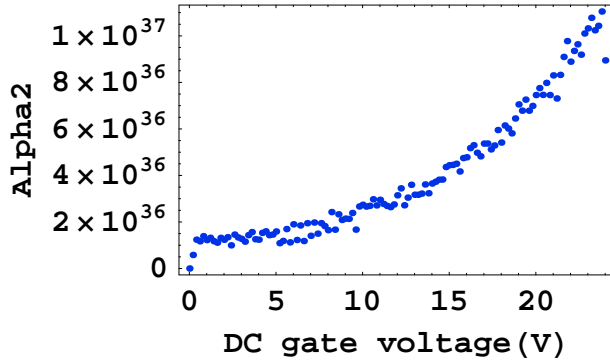
```
alphagraph = ListPlot[alphavsVgate, PlotStyle → {RGBColor[0, 1, 1], PointSize[0.015]},
```

```
Frame → True, FrameLabel → {"DC gate voltage(V)", "Alpha"}, ImageSize → Automatic]
```



```
alpha2vsVgate = Transpose[Union[{bb10[[1]]}, {bb10[[7]]}]];
```

```
alpha2graph = ListPlot[alpha2vsVgate, PlotStyle -> {RGBColor[0, 0.2, .9], PointSize[0.015]},
Frame -> True, Axes -> None, FrameLabel -> {"DC gate voltage(V)", "Alpha2"}, ImageSize -> Automatic]
```

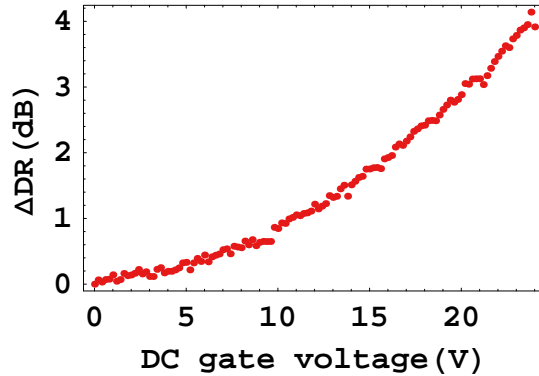


```
DR0 = First[bb10[[10]]];
```

```
DRvsVgate = Transpose[Union[{bb10[[1]]}, {bb10[[10]] - DR0}]];
```

```
DRgraph = ListPlot[DRvsVgate, PlotStyle -> {RGBColor[.9, .1, .1], PointSize[0.015]},
```

```
Frame -> True, Axes -> None, FrameLabel -> {"DC gate voltage(V)", "ΔDR(dB)"}, ImageSize -> Automatic]
```



## Tuning calculations using Galerkin discretization method

### Capacitance

```
Clear[x, y, r, R, z, a, A, As, F1, F2, K2, K3, K1, K4, K5, c, ρ, Y, Ym, T0, L, r, R, S, Sm, ε, ε0,
```

```
IM, IMm, V, gap, a, Eq, Freq, d, s, Veq, Vstab, dEq, Api];
```

```
K0 = Normal [Simplify [Series [  $\frac{2\pi\epsilon\epsilon_0}{\text{Log}[1/y*(1-a-x+y+\sqrt{(1-a-x+y)^2-y^2}]}$ , {x, 0, 0} ] ] ] ] ;
```

```
K1 = ( Normal [Simplify [Series [  $\frac{2\pi\epsilon\epsilon_0}{\text{Log}[1/y*(1-a-x+y+\sqrt{(1-a-x+y)^2-y^2}]}$ , {x, 0, 1} ] ] ] ] )
```

```
-K0)/x/R;
```

$$K2 = \left( \text{Normal} \left[ \text{Simplify} \left[ \text{Series} \left[ \frac{2\pi\epsilon_0}{\text{Log} \left[ 1/y * (1-a-x+y + \sqrt{(1-a-x+y)^2 - y^2}) \right]}, \{x, 0, 2\} \right] \right] \right] \right]$$

$$-(K1 * R) * x - K0/x^2/R^2;$$

$$K3 = \text{Simplify} \left[ \left( \text{Normal} \left[ \text{Simplify} \left[ \text{Series} \left[ \frac{2\pi\epsilon_0}{\text{Log} \left[ 1/y * (1-x-a+y + \sqrt{(1-a-x+y)^2 - y^2}) \right]}, \{x, 0, 3\} \right] \right] \right] \right] \right]$$

$$-K2 * (R * x)^2 - K1 * (R * x) - K0/(x * R)^3;$$

$$K4 = \text{Simplify} \left[ \left( \text{Normal} \left[ \text{Simplify} \left[ \text{Series} \left[ \frac{2\pi\epsilon_0}{\text{Log} \left[ 1/y * (1-a-x+y + \sqrt{(1-a-x+y)^2 - y^2}) \right]}, \{x, 0, 4\} \right] \right] \right] \right] \right]$$

$$-K3 * (R * x)^3 - K2 * (R * x)^2 - K1 * (R * x) - K0/(x * R)^4;$$

$$x = z/R;$$

$$y = r/R;$$

$$F0 = K1/2 * V^2;$$

$$F1 = K2 * V^2;$$

$$F2 = 3/2 * K3 * V^2;$$

$$F3 = 2 * K4 * V^2;$$

$$\text{Eq} = -(a * R) * \left( \frac{Y * \text{IM} + Y_m * \text{IM}_m}{3 * (\rho * S + \rho_m * \text{Sm})} * \left( \frac{2\pi}{L} \right)^4 + \frac{T_0}{3 * (\rho * S + \rho_m * \text{Sm})} \left( \frac{2\pi}{L} \right)^2 \right)$$

$$0009 - (a * R)^3 * \left( \frac{Y * S + Y_m * \text{Sm}}{18 * (\rho * S + \rho_m * \text{Sm})} * \left( \frac{2\pi}{L} \right)^4 - \frac{35F3}{18 * (\rho * S + \rho_m * \text{Sm})} \right) + \frac{\sqrt{2}F0}{\sqrt{3} * (\rho * S + \rho_m * \text{Sm})};$$

$$a = A/R;$$

$$d\text{Eq} = D[\text{Eq}, A];$$

$$\text{Veq}[A_] = V /. \text{First}[\text{Solve}[\text{Eq} == 0, V]];$$

$$\text{Vstab}[A_] = V /. \text{First}[\text{Solve}[d\text{Eq} == 0, V]];$$

SiC beam with Au layer

$$Y = 430 * 10^9;$$

$$Y_m = 78 * 10^9;$$

$$\rho = 2880;$$

$$L = 15 * 10^{(-6)};$$

$$w = 150 * 10^{-9};$$

$$t = 100 * 10^{-9};$$

$$\rho_m = 19300;$$

```

 $t_m = 35 * 10^{-9};$ 
 $t_m = 40 * 10^{-9};$ 
 $IM = w^3 * t/12;$ 
 $IMm = w^3 * t_m/12;$ 
 $S = w * t;$ 
 $Sm = w * t_m;$ 
 $T0 = 5.27 * 10^{-6};$ 
 $T0 = 6 * 10^{-6};$ 
 $r = 70 * 10^{(-9)};$ 
 $R = 300 * 10^{(-9)};$ 
 $\epsilon_0 = 8.8542 * 10^{(-12)};$ 
 $\epsilon = 1;$ 

```

Solve for freq, ac, DR and compare to experimental data

First, calculate pull-in amplitude and voltage:

```

 $A_{pi} = \text{Re}[A/.\text{FindRoot}[\text{Veq}[A] - \text{Vstab}[A] == 0, \{A, 10^{\wedge} - 11\}]]$ 

```

```

 $7.60308 \times 10^{-8}$ 

```

```

 $\text{Abs}[\text{Veq}[A_{pi}]]$ 

```

```

43.9911

```

```

 $\text{Stepper} = (\text{Npts} - 1)/\text{Abs}[\text{Veq}[A_{pi}]]$ 

```

```

2.72782

```

```

 $V = V1/\text{Stepper};$ 

```

```

 $V_{\text{max}} = \text{Abs}[\text{Veq}[A_{pi}]] * \text{Stepper};$ 

```

DC displacement amplitude:

```

 $\text{AsN} = \text{Table}[A/.\text{First}[\text{FindRoot}[\text{Eq} == 0, \{A, 10^{\wedge}(-9)\}], \{V1, 0, V_{\text{max}}\}];$ 

```

```

 $\text{VN} = \text{Table}[V, \{V1, 0, V_{\text{max}}\}];$ 

```

```

 $\text{V2N} = \text{Table}[V^{\wedge}2, \{V1, 0, V_{\text{max}}\}];$ 

```

A vs. V

$$\mathbf{APlot} = N[\text{Transpose}[\text{Union}[\{\mathbf{VN}\}, \{\mathbf{AsN}\}]]];$$

A vs.  $V^2$

$$\mathbf{A2Plot} = N[\text{Transpose}[\text{Union}[\{\mathbf{V2N}\}, \{\mathbf{AsN}\}]]];$$

$$\mathbf{A} = \mathbf{AsN};$$

Driving force terms in terms of capacitance coefficients:

$$\mathbf{F1N} = \mathbf{K2} * \mathbf{V2N};$$

$$\mathbf{F2N} = 3/2 * \mathbf{K3} * \mathbf{V2N};$$

$$\mathbf{F3N} = 2 * \mathbf{K4} * \mathbf{V2N};$$

Resonant frequency:

$$\mathbf{FreqN} = \frac{1}{2\pi} \sqrt{\left( \frac{Y * \mathbf{IM} + Y_m * \mathbf{IM}_m}{3 * (\rho * S + \rho_m * S_m)} * \left( \frac{2\pi}{L} \right)^4 + \frac{T_0}{3 * (\rho * S + \rho_m * S_m)} \left( \frac{2\pi}{L} \right)^2 + 0.0090009 + \frac{Y * S + Y_m * S_m}{(\rho * S + \rho_m * S_m)} * \frac{\mathbf{AsN}^2}{6} * \left( \frac{2\pi}{L} \right)^4 - \frac{\mathbf{F1N}}{(\rho * S + \rho_m * S_m)} \right)};$$

Quadratic nonlinear coefficient:

$$\mathbf{Alpha2} = \frac{Y * S + Y_m * S_m}{6 * (\rho * S + \rho_m * S_m)} * \mathbf{AsN} * \left( \frac{2\pi}{L} \right)^4 - \frac{5}{3} \sqrt{\frac{2}{3}} \frac{\mathbf{F2N}}{(\rho * S + \rho_m * S_m)};$$

Cubic nonlinear coefficient:

$$\mathbf{Alpha3} = \frac{Y * S + Y_m * S_m}{18 * (\rho * S + \rho_m * S_m)} * \left( \frac{2\pi}{L} \right)^4 - \frac{35 * \mathbf{F3N}}{18 * (\rho * S + \rho_m * S_m)};$$

$$\mathbf{First}[\mathbf{Alpha3}] // N$$

$$7.44158 \times 10^{28}$$

Effective nonlinearity:

$$\mathbf{Alpha} = \mathbf{Alpha3} - \frac{10 * \mathbf{Alpha2}^2}{9 * \mathbf{FreqN}^2};$$

Critical amplitude:

$$\mathbf{acrit} = \sqrt{\frac{8 * \sqrt{3} * (\mathbf{FreqN} * 2\pi)^2}{9 * \mathbf{Alpha} * Q}};$$

$$\mathbf{kB} = 1.38 * 10^{(-23)};$$

$$T = 20;$$

$$\mathbf{df} = 1;$$

Change in dynamic range using the experimental values for Q:

$$\Delta \mathbf{DR} = 20 * \text{Log} \left[ \sqrt{\frac{\mathbf{FreqN}^2 * \mathbf{First}[\mathbf{Alpha}] * \mathbf{First}[\mathbf{Qexp}]}{\mathbf{Qexp} * \mathbf{First}[\mathbf{FreqN}]^2 * \mathbf{Alpha}}} \right];$$

Resonant frequency vs. V:

```
FreqPlot = N[Transpose[Union[{VN}, {FreqN/106}]]];
```

Effective nonlinearity alpha vs. V:

```
AlphaPlot = N[Transpose[Union[{VN}, {Alpha}]]];
```

Quadratic nonlinearity alpha2 vs. V:

```
Alpha2Plot = N[Transpose[Union[{VN}, {Alpha2}]]];
```

Critical amplitude vs. V:

```
acritPlot = N[Transpose[Union[{VN}, {acrit}]]];
```

Change in dynamic range vs. V:

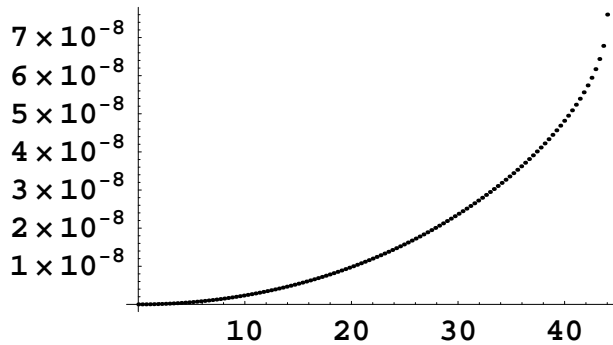
```
ΔDRPlot = N[Transpose[Union[{VN}, {ΔDR}]]];
```

```
First[FreqN]/106
```

8.78128

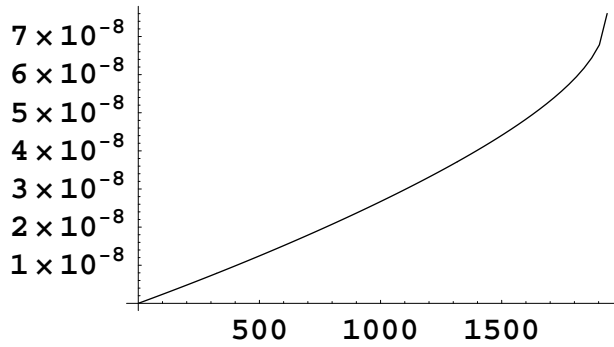
A<sub>DC</sub> vs. V:

```
a2 = ListPlot[APlot, PlotRange → All, ImageSize → Automatic]
```



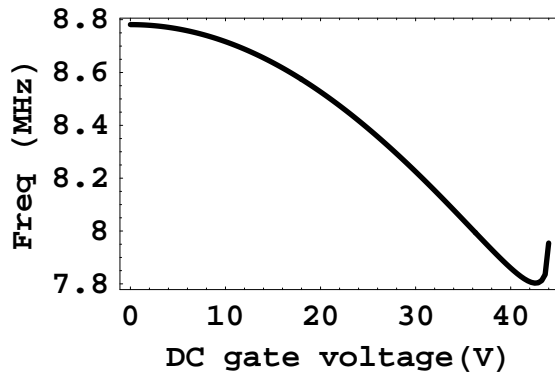
A<sub>DC</sub> vs. V<sup>2</sup>:

```
ListPlot[A2Plot, PlotJoined → True, PlotRange → All, ImageSize → Automatic]
```



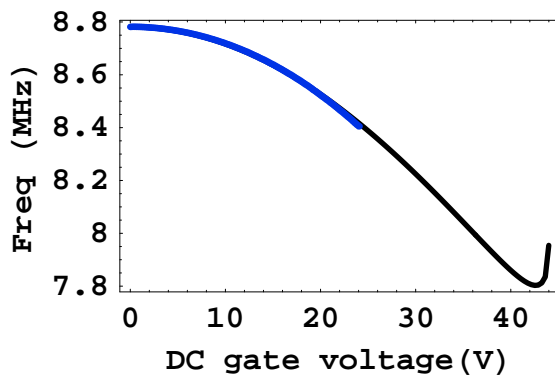
Resonant frequency vs.  $V$ :

```
f2 = ListPlot[FreqPlot, PlotStyle -> {RGBColor[0, 0, 0], AbsoluteThickness[2]},
PlotJoined -> True, PlotRange -> All, Frame -> True, Axes -> None,
FrameLabel -> {"DC gate voltage(V)", "Freq (MHz)"}, ImageSize -> Automatic]
```

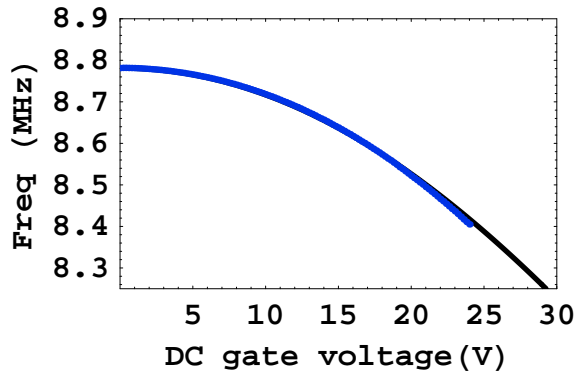


Compare theory(black) with data (blue):

```
Show[f2, f0graph, ImageSize -> Automatic]
```

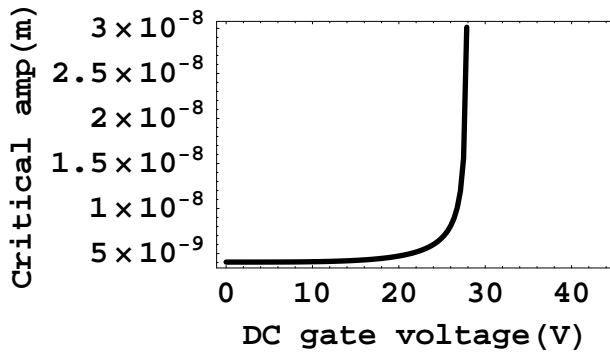


```
Show[f2, f0graph, PlotRange -> {{0, 30}, {8.25, 8.9}}, ImageSize -> Automatic]
```



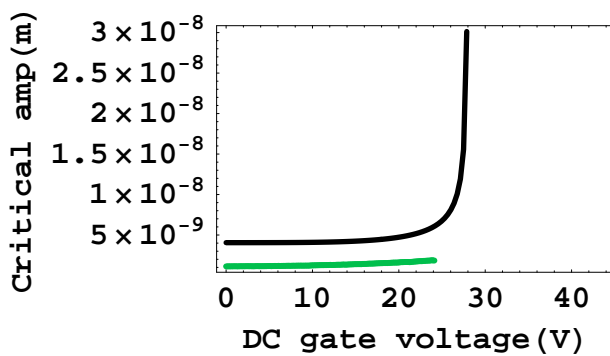
Critical amplitude vs.  $V$ :

```
acth = ListPlot[acritPlot, PlotStyle → {RGBColor[0, 0, 0], AbsoluteThickness[2]},
PlotJoined → True, PlotRange → All, Frame → True, Axes → None,
FrameLabel → {"DC gate voltage(V)", "Critical amp(m)"}, ImageSize → Automatic]
```



Compare theory(black) with data (green):

```
Show[acth, acgraph, ImageSize → Automatic]
```



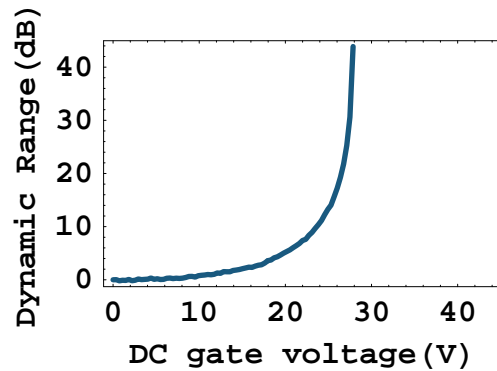
Dynamic range vs.  $V$ :

```
DRth = ListPlot[ΔDRPlot, PlotJoined → True, PlotRange → {All, All},
```

PlotStyle  $\rightarrow$  {RGBColor[.1, .35, .5], AbsoluteThickness[2], PointSize[0.015]},

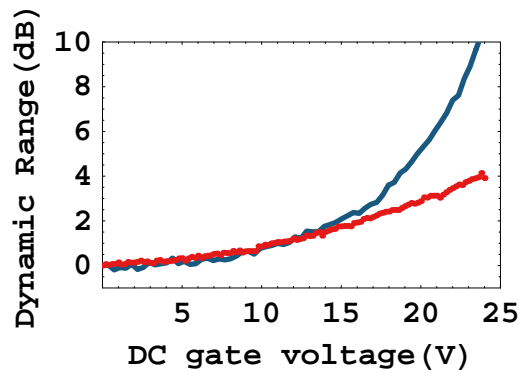
Frame  $\rightarrow$  True, Axes  $\rightarrow$  None, FrameLabel  $\rightarrow$  {"DC gate voltage(V)", "Dynamic Range(dB)"},

ImageSize  $\rightarrow$  Automatic]



Compare theory(blue) with data (red):

Show[DRth, DRgraph, PlotRange  $\rightarrow$  {{0, 25}, {-1, 10}}, ImageSize  $\rightarrow$  Automatic];



## Appendix C

# Matlab routine for fitting resonance with a background

This is the listing of the Matlab code that fits experimental resonance data to a Lorentzian using the procedure described in Chapter 3. The main program `fitdata.m` calls on `circfit.m`, `fitdtheta.m`, and `fullresfit.m` subroutines.

```
function result=fitdata(files, resultfile, FreqStart, FreqStop, flag);

% Inna Kozinsky
% 8 March 2006
% inna@caltech.edu
% x2914
%
% Arguments:
% files - full name of the data file, e.g. 'C:\Data\run1.dat')
% resultfile - full name of the file where the fit result is recorded
%             format recorded: f0 Q Amp
% Fstart - starting frequency for the fit, in MHz
% Fend - end frequency for the fit, in MHz
% flag - indicates initial f0 and Q guess options
%       0 for initial guess from dtheta fit - good for most cases
%       1 subtract line from the data before the dtheta fit - for low Qs
%       2 and 3 - manual f0 and Q guesses - when auto guesses are not good enough
%       2 use manual f0 and Q guess for dtheta fit, then use result for the
%         final fit
%       3 use manual f0 and Q guesses for the final fit, do not worry about
%         the dtheta fit
% Output:
% result = [Ax Ay Q f0 C0x C0y C1x C1y]

close all

comment=4; %number of comment lines at the beginning of data file
NoToSmooth=10; %how many points to smooth for dtheta fit
Fstart=FreqStart*1e-3; % convert to GHz
Fend=FreqStop*1e-3;

% read in the data from a file
temp=dlmread(files, '\t', comment, 0);

ifstarts=find(temp(:,1)>Fstart);
```

```

ifstart=ifstarts(1);
ifends=find(temp(:,1)<Fend);
ifend=ifends(end);

freq=temp(ifstart:ifend,1)*1e3;
xcomp=temp(ifstart:ifend,3);
ycomp=temp(ifstart:ifend,4);

% plot the loaded data
figure
title('Raw amplitude data')
hold on
plot(freq, sqrt(xcomp.^2+ycomp.^2));
xlabel freq, ylabel amp

if flag==1,
    % fit a line to the background
    xbgline_est(2)=(xcomp(end)-xcomp(1))/(freq(end)-freq(1));
    xbgline_est(1)=xcomp(1)-xbgline_est(2)*freq(1);
    ybgline_est(2)=(ycomp(end)-ycomp(1))/(freq(end)-freq(1));
    ybgline_est(1)=ycomp(1)-ybgline_est(2)*freq(1);
    hx=inline('xb(1)+xb(2)*freq', 'xb', 'freq');
    hy=inline('yb(1)+yb(2)*freq', 'yb', 'freq');
    xbgline=lsqcurvefit(hx, xbgline_est, freq, xcomp);
    ybgline=lsqcurvefit(hy, ybgline_est, freq, ycomp);
    xcomp_bg=xbgline(1)+xbgline(2).*freq;
    ycomp_bg=ybgline(1)+ybgline(2).*freq;

    % subtract background from x and y
    xcomp_sig=xcomp-xcomp_bg;
    ycomp_sig=ycomp-ycomp_bg;

    figure
    subplot(2,2,1)
    plot(freq,xcomp, '.', freq,xcomp_bg, 'm')
    subplot(2,2,2)
    plot(freq,ycomp, '.', freq,ycomp_bg, 'm')
    subplot(2,2,3)
    plot(freq,xcomp_sig, '.')
    subplot(2,2,4)
    plot(freq,ycomp_sig, '.')
else
    xcomp_sig=xcomp;
    ycomp_sig=ycomp;
end

%%% fit the data to a circle
cut=4/12; % fraction of data to cut from both ends of the data
[xc,yc,R,a]=circfit(xcomp_sig(round(end*cut):round(end*(1-cut))),
                    ycomp_sig(round(end*cut):round(end*(1-cut))));
th = 0:pi/length(freq):2*pi;
xfit1=R*cos(th)+xc;
yfit1=R*sin(th)+yc;

% fitting to a circle plot
figure
title('Data fitted to a circle')
hold on
plot(xcomp_sig(round(end*cut):round(end*(1-cut))),
     ycomp_sig(round(end*cut):round(end*(1-cut))), 'co',
     xcomp_sig, ycomp_sig, '.', xfit1, yfit1, 'r'),
xlabel x, ylabel y
axis equal

%%% find dtheta
% translate the center of the circle to (0,0)
xtrans=xcomp_sig-xc;
ytrans=ycomp_sig-yc;

```

```

domega=freq(2)-freq(1);

% figure out y(i+1)-y(i-1)
dy=[ytrans(1); diff(ytrans)];
dyminus1=dy;
dyminus1(1)=[];
dyminus1(end+1)=-ytrans(end);
dyy=dy+dyminus1;

% figure out x(i+1)-x(i-1)
dx=[xtrans(1); diff(xtrans)];
dxminus1=dx;
dxminus1(1)=[];
dxminus1(end+1)=-xtrans(end);
dxx=dx+dxminus1;

dtheta=(xtrans.*dyy-ytrans.*dxx)./(domega*2*R^2);

% plot of dtheta
figure
title('d\theta vs. freq')
hold on
plot(freq,dtheta, '.');
xlabel freq, ylabel d\theta

%%% Fit dtheta to get Q and f0
fitout=fitdtheta(freq, smooth(dtheta,NoToSmooth),flag);
Q=fitout(1);
f0=fitout(2);

%%% Find the resonance and background
%%% points on the circle
ipeak=find(freq==f0);
if (ipeak),
    x0=xtrans(ipeak);
    y0=ytrans(ipeak);
else
    ilower=find(freq<f0);
    ilow=ilower(end);
    ihigher=find(freq>f0);
    ihigh=ihigher(1);
    xlow=xtrans(ilow);
    xhigh=xtrans(ihigh);
    ylow=ytrans(ilow);
    yhigh=ytrans(ihigh);

    % Assume the f0 is in the same place between flow and fhigh
    % as (x0,y0) is between (xlow,ylow) and (xhigh,yhigh)
    x0=(f0-freq(ilow))/(freq(ihigh)-freq(ilow))*(xhigh-xlow)+xlow;
    y0=(f0-freq(ilow))/(freq(ihigh)-freq(ilow))*(yhigh-ylow)+ylow;
end

theta0=angle(x0+j*y0);
xbg=-x0;
ybg=-y0;

figure
hold on
plot(xtrans,ytrans, '.',x0,y0,'go',xbg,ybg,'gx')
axis equal

%%% Full 8-parameter fit of the experimental data to the Lorentzian
%%% with background

% x(1) = Ax = Re(amp*exp(theta0-3pi/2))
% x(2) = Ay = Im(amp*exp(theta0-3pi/2))
Amp=2*R; % amp estimate, max of sqrt((xtrans-xbg).^2+(ytrans-ybg).^2)

```

```

A=Amp*exp(j*(theta0-3*pi/2));
estimate(1)=real(A);
estimate(2)=imag(A);

% x(3) = Q
% x(4) = center frequency, f0
if flag==3,
    estimate(3) = input('Enter your guess for Q: ');
    estimate(4) = input('Enter your guess for f0 (MHz): ');
else,
    estimate(3)=Q;
    estimate(4)=f0;
end

if flag==1,
    % x(5) = C0x
    % x(6) = C0y
    estimate(5)=xbgline(1)+xbgline(2)*f0;
    estimate(6)=ybgline(1)+ybgline(2)*f0;
    % x(7) = C1x
    % x(8) = C1y
    estimate(7)=xbgline(2);
    estimate(8)=ybgline(2);
else
    % x(5) = C0x
    % x(6) = C0y
    estimate(5)=xbg+xc;
    estimate(6)=ybg+yc;
    % x(7) = C1x
    % x(8) = C1y
    estimate(7)=0;
    estimate(8)=0;
end

% Ax Ay Q f0 C0x C0y C1x C1y
result=fullresfit(freq,xcomp,ycomp,estimate);

fittedA=abs(result(1)+j*result(2));
fittedQ=result(3);
fittedf0=result(4);

% Format in the recorded file:
% f0 Q Amp
answer = input('Do you want to record the results? (y/n): ','s');
if answer=='y',
    dlmwrite(resultfile,[fittedf0 fittedQ fittedA],'delimiter','\t','-append')
end

function [xc,yc,R,a] = circfit(x,y)

% This function fits the raw experimental x and y data to a circle.
% [xc yc R] = circfit(x,y)
% x,y are column vector where (x(i),y(i)) is a measured point
% result is center point (yc,xc) and radius R
% an optional output is the vector of coefficients a describing the circle's equation
%  $x^2+y^2+a(1)*x+a(2)*y+a(3)=0$ 
%
% This routine written by Izhak Bucher, 25 Oct 1991.
% Courtesy of Matlab Central file exchange.

x=x(:); y=y(:);
a=[x y ones(size(x))]\[-(x.^2+y.^2)];
xc = -.5*a(1);
yc = -.5*a(2);
R = sqrt((a(1)^2+a(2)^2)/4-a(3));

```

```

function output=fitdtheta(xdata, ydata, flag);

% This function fits the experimental dtheta/domega values to the
% theoretical function dtheta/domega=-4*gamma/(gamma^2+4*(omega-omega0)^2

% dtheta/domega
h=inline('-4*x(1)./(x(1)^2+4*(xdata-x(2)).^2)', 'x', 'xdata');

% x(1) = gamma = omega0/Q
% x(2) = omega0 (resonance frequency)

if flag==2,
    guessQ = input('Enter your guess for Q: ');
    estimate(2) = input('Enter your guess for f0 (MHz): ')*1e6;
    estimate(1) = estimate(2)/guessQ;
else
    % estimate resonant frequency
    indexmax=find(abs(ydata)==max(abs(ydata)));
    estimate(2)=xdata(indexmax(1));

    % estimate Q as full width at half max
    halfpeak_ind=find(abs(ydata)>=(max(abs(ydata))/2));
    df=xdata(halfpeak_ind(end))-xdata(halfpeak_ind(1));
    if max(abs(ydata))==max(ydata),
        estimate(1)=-df;
    else
        estimate(1)=df;
    end
end

% actual fitting goes on here
clear LB;
clear UB;
LB=[-Inf, xdata(1)];
UB=[Inf, xdata(end)];

OPTIONS=optimset('lsqcurvefit');
OPTIONS=optimset(OPTIONS, 'TolX', 1e-20);
OPTIONS=optimset(OPTIONS, 'TolFun', 1e-20);
OPTIONS=optimset(OPTIONS, 'MaxFunEvals', 1000);
OPTIONS=optimset(OPTIONS, 'MaxIter', 1000);

xfit=lsqcurvefit(h, estimate, xdata, ydata, LB, UB, OPTIONS);

outcome=h(xfit, xdata);
initial=h(estimate, xdata);

% display results
disp(strcat('Q      = ', num2str(xfit(2)/xfit(1))));
disp(strcat('f0    = ', num2str(xfit(2))));

% plot of dtheta fit
figure
hold on
plot(xdata, outcome,'r', xdata, initial,'g',xdata, ydata, '.');
hold off

out(1)=xfit(2)/xfit(1);    % Q
out(2)=xfit(2);          % f0

% Q f0
output=out;

```

```

function output=fullresfit(f, xexp, yexp, estimate);

% This is a full 8-parameter fit of the Lorentzian with background
% For constant background or background varying linearly with frequency
% i.e. C0 + C1*freq
%
% Data and the values for estimate are real values.
% The response has the form for A=Ax+jAy; C0=C0x+jC0y; C1=C1x+jC1y:
% R(f)=A*f0^2/Q/(f0^2-f^2+j*f*f0/Q)+C0+C1(f-f0)*2*pi == data
%
% x(1) = Ax = Re(amp*exp(j*(theta0-3pi/2)))
% x(2) = Ay = Im(amp*exp(j*(theta0-3pi/2)))
% x(3) = Q
% x(4) = f0
% x(5) = C0x
% x(6) = C0y
% x(7) = C1x
% x(8) = C1y

clear LB;
clear UB;
LB=[-Inf, -Inf, -f(1)/(f(2)-f(1)), f(1), -1, -1, -1, -1];
UB=[Inf, Inf, f(1)/(f(2)-f(1)), f(end), 1, 1, 1, 1];

OPTIONS=optimset('lsqnonlin');
OPTIONS=optimset(OPTIONS, 'TolX', 1e-20);
OPTIONS=optimset(OPTIONS, 'TolFun', 1e-20);
OPTIONS=optimset(OPTIONS, 'MaxFunEvals', 3000);
OPTIONS=optimset(OPTIONS, 'MaxIter', 1000);

xfit=lsqnonlin(@x) [real((x(1)+j*x(2))*x(4)^2/x(3)./(x(4)^2-f.^2+j*f.*x(4)/x(3)))+
    +x(5)+x(7)*(f-x(4)).*2*pi-xexp; imag((x(1)+j*x(2))*x(4)^2/x(3)./(x(4)^2-f.^2+
    +j*f.*x(4)/x(3)))+x(6)+x(8)*(f-x(4)).*2*pi-yexp], estimate, LB,UB,OPTIONS);

fittedx=real((xfit(1)+j*xfit(2))*xfit(4)^2/xfit(3)./(xfit(4)^2-f.^2+
    +j*f.*xfit(4)/xfit(3))+xfit(5)+xfit(7)*(f-xfit(4)).*2*pi;
fittedy=imag((xfit(1)+j*xfit(2))*xfit(4)^2/xfit(3)./(xfit(4)^2-f.^2+
    +j*f.*xfit(4)/xfit(3))+xfit(6)+xfit(8)*(f-xfit(4)).*2*pi;

guessx=real((estimate(1)+j*estimate(2))*estimate(4)^2/estimate(3)./(estimate(4)^2-f.^2+
    +j*f.*estimate(4)/estimate(3))+estimate(5)+estimate(7)*(f-estimate(4)).*2*pi;
guessy=imag((estimate(1)+j*estimate(2))*estimate(4)^2/estimate(3)./(estimate(4)^2-f.^2+
    +j*f.*estimate(4)/estimate(3))+estimate(6)+estimate(8)*(f-estimate(4)).*2*pi;

% Display results
disp(strcat('Q from fit      = ', num2str(xfit(3))));
disp(strcat('f0 from fit   = ', num2str(xfit(4)), ' MHz'));
disp(strcat('Amp from fit  = ', num2str(abs(xfit(1)+j*xfit(2))), ' V'));

figure
subplot(2,2,1)
hold on
title('x')
xlabel('freq')
ylabel('x')
plot(f, xexp, '.', f, guessx, 'g', f, fittedx, 'r');
subplot(2,2,2)
hold on
title('y')
xlabel('freq')
ylabel('y')
plot(f, yexp, '.', f, guessy, 'g', f, fittedy, 'r');
subplot(2,2,3)
hold on
title('amp')
xlabel('freq')
ylabel('amp')
plot(f, abs(xexp+j*yexp), '.', f, abs(fittedx+j*fittedy), 'r');

```

```

subplot(2,2,4)
hold on
title('phase')
xlabel('freq')
ylabel('phase')
plot(f, angle(xexp+j*yexp), '.',f, angle(fittedx+j*fittedy),'r');

% This is the resonance with the background subtracted
nobgx=real((xfit(1)+j*xfit(2))*xfit(4)^2/xfit(3)./(xfit(4)^2-f.^2+j*f.*xfit(4)/xfit(3)));
nobgy=imag((xfit(1)+j*xfit(2))*xfit(4)^2/xfit(3)./(xfit(4)^2-f.^2+j*f.*xfit(4)/xfit(3)));

figure
subplot(2,2,1)
hold on
title('x')
xlabel('freq')
ylabel('x')
plot(f, nobgx);
subplot(2,2,2)
hold on
title('y')
xlabel('freq')
ylabel('y')
plot(f, nobgy);
subplot(2,2,3)
hold on
title('amp')
xlabel('freq')
ylabel('amp')
plot(f, abs(nobgx+j*nobgy));
subplot(2,2,4)
hold on
title('phase')
xlabel('freq')
ylabel('phase')
plot(f, unwrap(angle(nobgx+j*nobgy)));

% Ax Ay Q f0 C0x C0y Clx Clx
output=xfit;

```